

**Very Low Temperature Sensitive, Deep-Well Quantum
Cascade Lasers ($\lambda = 4.8 \mu\text{m}$) grown by MOCVD**

by

Jae Cheol Shin

**A dissertation submitted in partial fulfillment of
the requirements for the degree of**

**Doctor of Philosophy
(Electrical and Computer Engineering)**

at the

UNIVERSITY OF WISCONSIN-MADISON

2010

Very Low Temperature Sensitive, Deep-Well Quantum Cascade Lasers

($\lambda = 4.8 \mu\text{m}$) grown by MOCVD

submitted to the Graduate School of the

University of Wisconsin-Madison

in partial fulfillment of the requirements for the

degree of Doctor of Philosophy

by

Jae Cheol Shin

Date of final oral examination: June 28, 2010

Month and year degree to be awarded: August 2010

The dissertation is approved by the following members of the Final Oral Committee:

Dan Botez, Philip Dunham Reed Professor of Electrical and Computer Engineering

Leon McCaughan, Professor of Electrical and Computer Engineering

Luke J. Mawst, Professor of Electrical and Computer Engineering

Irena Knezevic, Assistant Professor of Electrical and Computer Engineering

Thomas F. Kuech, Milton J. and A. Maude Shoemaker Professor of Chemical and

Biological Engineering

Very Low Temperature Sensitive, Deep-Well Quantum Cascade Lasers
($\lambda = 4.8 \mu\text{m}$) grown by MOCVD

Jae Cheol Shin

Under the supervision of Professor Dan Botez
At the University of Wisconsin-Madison

Abstract

Varying-composition, deep-well quantum cascade laser (DW-QCL) structures are proposed to suppress carrier leakage at and above room temperature. The layer compositions of the quantum wells and barriers in the active region differ from those in the extractor/injector regions. These structures are grown by using metal organic chemical vapor deposition (MOCVD). Fabricated ridge-guide devices, lasing at $\sim 4.8 \mu\text{m}$, show ultra-low temperature sensitivity of their electro-optical characteristics by comparison to those of conventional QCLs emitting in the $4.5\text{-}5.5 \mu\text{m}$ wavelength range. T_0 values as high as 278 K and T_1 values as high as 285 K are obtained over a wide temperature range: 20-90 °C.

We introduce modified equations for J_{th} and η_d which take into account both leakage and backfilling currents. Using these equations we can obtain reasonably good agreement between calculated and experimental values for T_o and T_1 for both conventional and DW-type QCLs by using the modified J_{th} and η_d equations, in conjunction with a model for electron thermal excitation in and out of the active region.

In Ch. 6 we increase the barriers' height in the active region from the injection barrier to the exit barrier, so called tapered active-region QCL. As a result, we further increase the energy separation between the upper laser level and the upper energy states. Thus, electrons in upper laser level can hardly reach the highest energy state in the active region. This design reduces the electron-leakage current by a factor of ~ 3 compared to that in deep-well QCLs. Moreover, the lifetime in the upper laser level is kept similar to that in high-performance conventional QCLs. Then, the threshold current of the TA-QCL device at room-temperature decreases by $\sim 20\%$ compared to that for conventional, high-performance QCLs. The combination of significantly reduced electron leakage and lower room-temperature threshold leads to much higher wallplug efficiencies for TA-QCL devices than for conventional QCL devices.

Acknowledgement

My time at the University of Wisconsin-Madison has been very precious to me. My work could not have been as successful without the support, encouragement and guidance from a lot of people. I would like to express my immense appreciations.

First, I would like to thank my advisor, Philip Dunham Reed Professor Dan Botez. He gave me a very interesting and challenging project to work on as well as valuable guidance and support.

Additionally, I would like to thank Professor Luke J. Mawst for his invaluable suggestions, comments and encouragements on my research.

I also want to thank all of my Ph. D. defense committee members, Professor Leon McCaughan, Professor Irena Knezevic from the department of Electrical and Computer Engineering, and Professor Thomas Kuech from the department of Chemical and Biological Engineering for their helpful comments and suggestions.

Finally, I would like to thank all of my previous and current colleagues, Nam-Heon Kim, Dapeng. Xu, Mithun D'Souza, Joo Hyung Park, Charles Paulson, Juno Yu-Ting Huang, Jeremy Kirch, Sangho Kim, Toby Garrod, Peter Dudley, Yinggang Huang, Tae Hee Kim, Tae Wan Kim, and Richard Delgado.

I thank my parents, wife, brother, and daughter.

Jae Cheol Shin

June 28, 2010

Table of Contents

Abstract	i
Acknowledgement	iii
Table of Contents	iv
List of Figures	vii
List of Tables	xi
Chapter 1 Introduction	1
1.1 General introduction	1
1.2 Mid-IR coherent light sources	2
1.2.1 CO and CO₂ Gas lasers	3
1.2.2 Lead-salt lasers	4
1.2.3 Antimonide-based interband laser	5
1.2.4 Interband cascade laser	6
Chapter 2 Theoretical background for quantum cascade laser	12
2.1 General introduction	12
2.2 Theoretical frame work for quantum cascade laser	14
2.3 Quantum cascade laser	17
2.4 The diagonal-transition design in Active region	19
2.5 The vertical transition QCL structure	20
2.6 Double-phonon resonance design for the active-region QCLs	22
2.7 Rate equations	23

2.8 Thermal effects	27
Chapter 3 MOCVD crystal growth	32
3.1 Introduction	32
3.2 Reactor gas delivery	33
3.3 Reaction chamber	37
3.4 Growth temperature	38
3.5 Growth rate layer composition	39
3.6 V/III ratio	46
3.7 Layer strain	46
3.8 Doping concentration	49
3.9 HRXRD of the 30 stages deep-well QC structure	50
Chapter 4 4.8 μm emitting deep-well Quantum Cascade Laser	55
4.1 Introduction	55
4.2 Deep-well QCL structure design	56
4.3 Growth condition and fabrication	61
4.4 Results and discussion	62
4.5 Conclusion	66
Chapter 5 Ultra-low temperature sensitive, deep-well, Quantum Cascade Laser via tapering the injector region	69
5.1 Introduction	69

5.2	Modified equation for the threshold current and the differential quantum efficiency	70
5.3	The design of tapering-injector, deep-well QCL	74
5.4	Results and discussion	79
5.5	Estimates for temperature dependences of threshold current and differential quantum efficiency	82
5.6	Conclusion	88
Chapter 6	Tapred Active-Region Quantum Cascade Laser	92
6.1	Introduction	92
6.2	The design of tapered active-region QCL device	93
6.3	Conclusion	100
Appendix	The growth spreadsheet for the 4.8 μm emitting tapered injector DW-QCLs	103

List of Figures

- Fig. 1-1 The lattice periodicity length of IV-VI semiconductor compounds versus the bandgap energy or wavelength [21]. III-V and II-VI compounds are also shown for comparison. The lower abscissa shows the relative lattice misfit to Si.
- Fig. 1-1 The conduction and valance band diagram of the type-II ICL at an applied electric field of 100 kV/cm, as proposed by Meyer in 1996 [28]. Each period is composed of an active region (I), electron barrier (II) and injection region (III).
- Fig. 2-1 The conduction band diagram of the photon-assisted tunneling proposed by Kazarinov and Suris [2]. A photon is emitted via inter-well photon-assisted tunneling transition between the ground state (level 1) of n^{th} well and the first excited state (level 2) of $(n+1)^{\text{th}}$ well.
- Fig. 2-2 Conduction band diagram of general QCL structure. Each stage consists of an injector/Bragg-reflector region and an active region. Electrons are moving from left to right and a wavy arrow indicates the photon emission. Energy states 3 and 2 are the upper and lower laser levels, respectively and the energy state 1 is separated by one phonon energy from energy state 2 and thus it helps depopulating the lower laser level.
- Fig. 2-3 The first operated Quantum Cascade Laser structure in 1994 [1]: calculated conduction band diagram of $\text{Ga}_{0.47}\text{In}_{0.53}\text{As}$ (well) and $\text{Al}_{0.48}\text{In}_{0.52}\text{As}$ (barriers) under an applied electric field. State 3 is the upper laser level, state 2 is the lower laser level and state 1 is the ground level. The dashed lines correspond to the digitally graded injector which helps the injection of electrons into the upper laser level of the next stage.
- Fig. 2-4 Schematic of calculated conduction band diagram and relevant wavefunctions under applied electric field of 85 kV/cm. State 3 is the upper laser level, and state 2 is lower laser level. The lower miniband causes electron extraction from states 2 and 1 and injection into the upper laser level of the next stage, while the minigap prevents electrons from escaping from state 3 to the continuum. (b) The electron transmission of the superlattice vs. energy. E1, E2 and E3 indicate the electron energies for states 3, 2 and 1, respectively.
- Fig. 2-5 The schematic diagram of calculated conduction band and key wavefunctions in active region. The active region consists of 4 QWs [14]. The energy separations between states 3 and 2 and states 2 and 1 correspond to the phonon energy in the semiconductor.
- Fig. 2-6 Conduction band of the three-level system of the QCL structure. The wavy

arrow indicates photon emission and other arrows indicate tunneling and the relaxation process from state 2 to state 1. The gray region is the region below the quasi-Fermi level in the injection region. The upper laser level is state 3, lower laser level is state 2 and the ground level is state 1.

- Fig. 2-7 Conduction band diagram of the conventional QC structure: g is ground state of the injector. States 3 and 2 are the upper and lower laser level, respectively. Rising the temperature increases both carrier leakage from the upper laser level and carrier backfilling into the lower laser level from the next-stage injector.
- Fig. 3-1 Schematic diagram of A-200 MOCVD reactor delivery system.
- Fig. 3-2 Schematic diagram of the MO source lines. The MO sources are generally kept as liquid in stainless-steel bubbler except TMIn which is kept as solid. The input connection tubing locates near the bottom of the bubbler under the surface of the MO sources.
- Fig. 3-3 Schematic diagram of the hydride lines. The hydride gas cylinder is connected to the double welled stainless-steel line and output gas is controlled by MFC.
- Fig. 3-4 Schematic diagram of A-200 Horizontal reactor: (a) side view (b) top view. MO sources and hydrides flows from left side with H_2 carrier gas. The wafer rotation is controlled by H_2 flows.
- Fig. 3-5 Vapor pressure of TMIn at 50 °C of the bath temperature vs. run number [9].
- Fig. 3-6 Experimental and simulated XRD (0 0 4) reflection spectra for a 5- period superlattice composed of alternating layers of $In_xGa_{1-x}As/InP$ or $Al_xIn_{1-x}As/InP$.
- Fig. 3-7 Experimental and simulated XRD spectra for 5-period superlattices of: (a) $Al_{0.75}In_{0.25}As/In_{0.40}Ga_{0.60}As$; and (b) $In_{0.68}Ga_{0.32}As/Al_{0.56}In_{0.44}As$ layer pairs.
- Fig. 3-8 Mid-IR absorption spectra as a function of wavelength at RT: (a) 20-period of $In_{0.53}Ga_{0.47}As$ (57 Å)/ $Al_{0.52}In_{0.48}As$ (200 Å). (b) 20-period of $In_{0.60}Ga_{0.40}As$ (46 Å)/ $Al_{0.56}In_{0.44}As$ (57 Å). Both absorption spectra are exactly matched with simulation results by 8-band K*P code.
- Fig. 3-9 TEM image for a 30-stage, strain-compensated, deep-well QC structure. The layers in a period are compressive or tensile strained which consist of seven different compositions.
- Fig. 3-10 ECV measurement data for a three-period $In_{0.60}Ga_{0.40}As/Al_{0.56}In_{0.44}As$

(300/300Å) structure. (a) The $\text{In}_{0.60}\text{Ga}_{0.40}\text{As}$ layer is doped and (b) the $\text{Al}_{0.56}\text{In}_{0.44}\text{As}$ layers are doped while the other layer is left undoped. Both structures have a target Si-doping concentration of $1 \times 10^{17} \text{ cm}^{-3}$.

Fig. 3-11 Experimental and simulated HRXRD (0 0 4) reflection spectra of 30 stages deep-well QC structures.

Fig. 4-1 Conduction band diagram and key wavefunctions for Conventional QC laser emitting at $4.8 \mu\text{m}$ [5]. The upper lasing level is labeled as 4; while 5, 6 and 7 are upper energy states in the active region. The laser transition occurs between states 4 and 3. The electrons in state 4 leak out in two ways: a) thermal scattering process to the upper Γ miniband (dashed dot region); b) thermal excitation to levels 5 and 6 followed by relaxation to the lower AR states 3, 2 and 1.

Fig. 4-2 Conduction band diagram and key wavefunctions for Deep-well QC laser emitting at $4.8 \mu\text{m}$ under an electric field of 75 kV/cm ($\lambda \approx 4.8 \mu\text{m}$). The upper lasing level is labeled as 4; while 5, 6 and 7 are upper energy states in the active region. The lasing transition occurs between states 4 and 3.

Fig. 4-3 L-I curves in pulsed (100ns, 2kHz) modes at various heatsink temperatures. Also shown is the V-I curve at 20°C . The inset shows the lasing spectrum at room temperature near threshold current with an emission peak at $4.84 \mu\text{m}$.

Fig. 4-4 SEM micrographs of exposed and developed PS templates annealed for 1 hour at (a) 140°C , (b) 165°C , and (c) 180°C . Threshold-current density and slope efficiency, η_s as a function of heatsink temperature

Fig. 4-5 Light vs current curve of a 3 mm-long, uncoated device with stripe width of $27 \mu\text{m}$ in pulsed (250ns, 2kHz) mode at 20°C .

Fig. 4-11 SEM micrographs of PS-cylinder-forming diblock copolymer spin-casted from 1.5 % (w/w) PS-*b*-PMMA (MW: 20 kg mol^{-1} for PS and 50 kg mol^{-1} for PMMA) diluted in toluene at (a) 3, (b) 4, and (c) 5 krpm after annealing more than 24 hour in vacuum, provided by Chi-Chun Liu and Prof. Paul Nealey, Dept. of Chemical Engineering in Univ. of Wisconsin - Madison.

Fig. 5-1 Schematic representation of the primary leakage paths for electrons injected into the upper laser level of a $4.5\text{-}5.5 \mu\text{m}$ -emitting QCL of the DPR design. g is the injector region ground state, 1 through 6 are energy states in the active region, and the area marked as upper Γ miniband corresponds to the energy states in the upper Γ miniband of the extractor region.

Fig. 5-2 The conduction band diagram of deep-well QCL design: (a) Original deep well QCL design [1], (b) three $\text{Al}_{0.65}\text{In}_{0.35}\text{As}$ barriers placed after the exit

barrier of the original deep-well QCL design (c) tapered-injector design for the original deep-well QCL.

- Fig. 5-3 Conduction band diagram and key wavefunctions for tapering injector Deep-well QC laser emitting at $4.8 \mu\text{m}$ under an electric field of 74 kV/cm ($\lambda \approx 4.8 \mu\text{m}$). The upper lasing level is labeled as 4; while 5, 6 and 7 are upper energy states in the active region. The lasing transition occurs between states 4 and 3.
- Fig. 5-4 Conduction band diagram and key wavefunctions for tapering injector Deep-well QC laser emitting at $4.8 \mu\text{m}$ under an electric field of 74 kV/cm ($\lambda \approx 4.8 \mu\text{m}$). The upper lasing level is labeled as 4; while 5, 6 and 7 are upper energy states in the active region. The lasing transition occurs between states 4 and 3.
- Fig. 5-5 L-I curves in pulsed (100 ns, 2 kHz) modes at various heatsink temperatures. Also shown is the V-I curve at 20°C . The inset shows the lasing spectrum at room temperature near threshold current with an emission peak at $4.85 \mu\text{m}$.
- Fig. 5-6 For device A, threshold-current density and slope efficiency as a function of heatsink temperature. The inset shows the T_0 value of 315 K in the temperature range 80 to 293 K.
- Fig. 5-7 Light vs current curve of a device B (3 mm long, uncoated device with stripe width of $26 \mu\text{m}$) in pulsed (250ns, 2kHz) mode at 20°C . Inset shows that threshold-current density as a function of heatsink temperature, T_0 , has a value of 278 K.
- Fig. 6-1 Conduction-band profile and key wavefunctions for: (a) Tapered injector (TI) Deep-well (DW) QCL emitting at $\lambda = 4.8 \mu\text{m}$, (b) TI DW-QCL structure with shortened width of the third well, and (c) shortened width of the fourth well. The upper laser level is labeled 4, while 5 and 6 are higher energy states in the active region. The lower laser level is labeled 3, while 2 and 1 are lower energy states in the active region.
- Fig. 6-2 Conduction band diagram and energy levels under a certain electric field. The quantum wells are $\text{In}_{0.68}\text{Ga}_{0.32}\text{As}$ for all structures. The barriers in (a) and (b) are $\text{Al}_{0.60}\text{In}_{0.40}\text{As}$. In (c) and (d) we have both $\text{Al}_{0.60}\text{In}_{0.40}\text{As}$ and $\text{Al}_{0.75}\text{In}_{0.25}\text{As}$ barriers.
- Fig. 6-3 Conduction-band profile and key wavefunctions for: (a) Deep-well QCL (b) Tapered active-region, deep-well QCL emitting at $\lambda = 4.8 \mu\text{m}$. The upper laser level is labeled 4, while 5 and 6 are higher energy states in the active region. The band profile at the top of each figure corresponds to the X valley.

List of Tables

- Table 3-1 The group III sources and vapor pressure with storage temperature, group V sources and dopant of MOCVD A-200 system
- Table 3-2 The InP, $\text{In}_x\text{Ga}_{1-x}\text{As}$ and $\text{Al}_x\text{In}_{1-x}\text{As}$ lattice constant and strains with InP substrate. The materials in list used in deep-well QC structures. The negative value is compressive strain while the positive value is tensile strain.
- Table 5-1 Estimated parameters for conventional and deep-well QCLs of DPR design ($\lambda = 4.6\text{-}4.8\ \mu\text{m}$).

Chapter 1

Introduction

1.1 General introduction

Semiconductor lasers have been used in many applications such as laser printing, CD players, DVD players, barcode scanners, chemical-agent detection and fiber-optical communication. A wide range of laser-emission wavelengths is needed, depending on what application the devices are intended to be used for. The GaAs- and InP- based semiconductor lasers have been successfully applied for the near-infrared (NIR) range ($0.7 - 1.55 \mu\text{m}$) with very high wallplug efficiency and power [1, 2]. However, semiconductor lasers for the mid-infrared (MIR) and far-infrared (FIR) emission ranges ($3 - 5 \mu\text{m}$ and $8 - 12 \mu\text{m}$, respectively) still suffer from low output powers and wallplug efficiency. For NIR emission, semiconductor lasers use interband transitions. Light is generated when an electron and a hole recombine in a forward-biased pn-junction; so it is called a bipolar device. The emission wavelength of bipolar devices is determined mainly by the bandgap of the material and partly by the width(s) of the quantum well(s) in the active region. The bandgaps of GaAs-based and InP-based materials are well matched to the NIR region. In contrast, quantum cascade lasers (QCLs), whose emission wavelengths are much longer than those in the NIR region, are unipolar devices since they use only electrons or holes for light generation. The emission wavelength is mainly

related on an active-region design including quantum wells (QWs) and barriers of various thicknesses; thus, allowing for emitting at any wavelength subject to thickness of the QWs and the conduction-band offsets of the semiconductor materials involved. This design flexibility for QCLs enables the emitting wavelength of laser sources to span from the MIR range to the THz range (3 to 200 μm). The MIR laser sources are applied for breath analysis, free-space communication and gas sensing [3-5]. Many gas molecules such as CO_2 , CH_4 , and C_2H_6 have their fundamental rotational-vibrational absorption in the MIR range, and the absorption lines are very strong. Therefore, it is possible to detect parts-per-billion (ppb) trace of the gas molecules using this range of coherent light sources [4]. The QCLs are the most promising sources for MIR and FIR regions because these are very stable and lase at room temperature.

In this thesis, I will present a novel type of QCL, so called deep-well quantum cascade lasers (DW-QCLs) emitting at 4.8 μm . The DW-QCLs have shown very low temperature sensitivity of their electro-optical characteristics by comparison to conventional QCLs. Therefore it is expected that DW-QCLs will provide very high wallplug efficiencies at room temperature (RT) in continuous wave (CW) operation.

1.2 Mid-IR coherent light sources

Coherent light sources for the infrared range have been researched since early 50's. Gordon and Townes realized microwave amplification by stimulated emission of radiation (MASER) in 1954 [6, 7]. After the realization of the MASER concept, Schawlow and Townes proposed a technique for the generation of coherent and very

monochromatic radiation in the infrared region using potassium vapor as active medium [8]. The first demonstration of the LASER (light amplification by stimulated emission of radiation) concept was achieved by Maiman at Hughes Labs, by using a ruby crystal [9]. The first semiconductor diode lasers for the NIR region were achieved in 1962 by several groups [10-13] and the first MIR laser was achieved in 1963 using InAs material system (3.1 μm) by Melngailis [14]. Pb-salts lasers (6.5 μm) and CO₂ lasers (9.4 and 10.4 μm) were achieved in 1964 by Butler [15] and Patel [16, 17], respectively. The first quantum cascade laser (QCL) was realized in 1994 by Faist et al. in Bell Labs [18].

1.2.1 CO and CO₂ Gas Lasers

One of the earliest gas lasers is the CO₂ laser which was demonstrated at Bell Labs in 1964 [17] and it is still one of the most useful and powerful lasers in the FIR region. CO₂ lasers can generate hundreds of kilowatts (kW) of continuous power at the 9.4 μm and 10.6 μm wavelengths [19]. These extremely high-power lasers are used for industrial applications, such as cutting and welding. Also, the light from CO₂ gas lasers is strongly absorbed in water, which makes up most biological tissue; thus those lasers are very useful for medical applications such as microsurgery, skin resurfacing, and ophthalmic procedures. The CO laser is also one of the most useful sources at the wavelength range from 2.5 μm to 8 μm . It is line-tunable in the 5 - 8 μm wavelength range when operated on the fundamental rotational-vibrational transitions, and the first overtone lasing can cover in the range of 2.7 to 3.6 μm [20].

1.2.2 Lead-salt lasers

The lead salts have a direct and relatively small energy bandgap; thus are suitable as optoelectronic devices for the MIR and FIR ranges. Figure 1.1 shows that the bandgaps of PbS, PbSe and PbTe materials, located in MIR range, with lattice constant of 5.8, 6 and 6.4 Å, respectively. These materials have relatively large variation of lattice constant, but the mixtures of Cd and Sn lead to very large bandgap shifts with small lattice-constant variation, as seen in Figure 1.1.

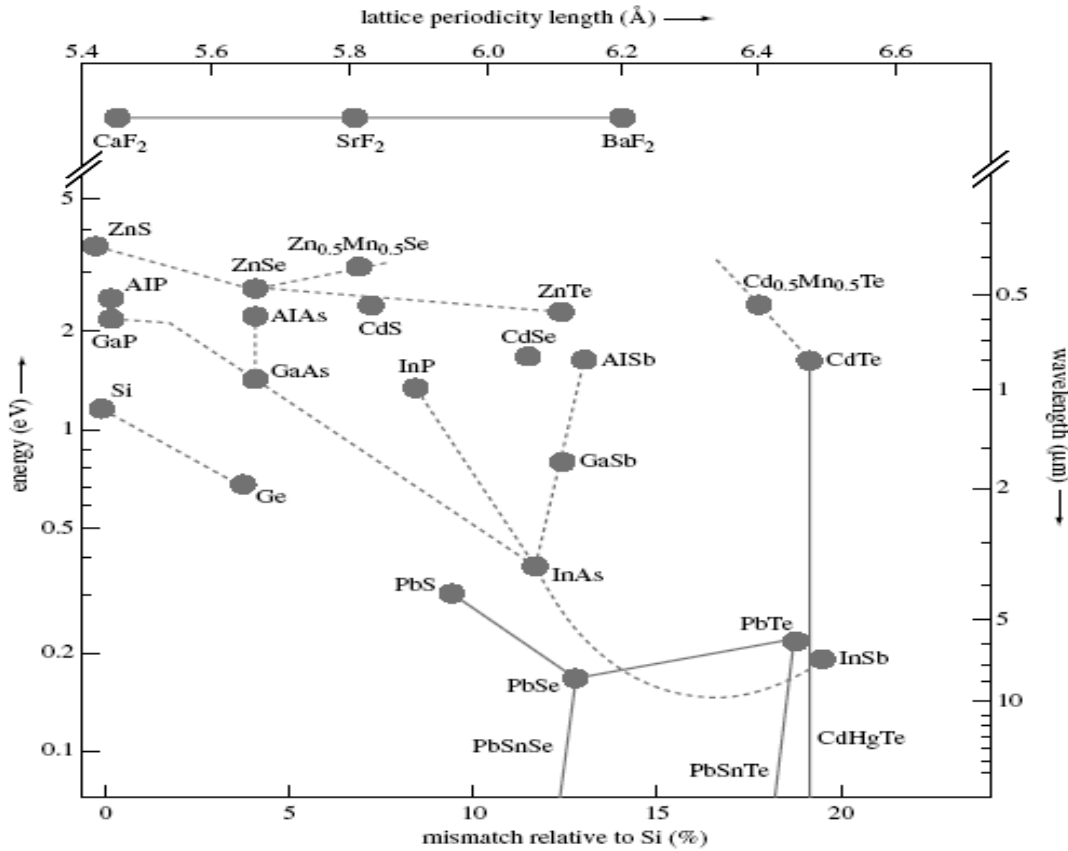


Figure 1.1: The lattice periodicity length of IV-VI semiconductor compounds versus the bandgap energy or wavelength [21]. III-V and II-VI compounds are also shown for comparison. The lower abscissa shows the relative lattice misfit to Si.

The lead-salts materials physically differ from the conventional III-V semiconductors such as GaAs and InP. For these materials the direct bandgap is not located at the Γ – point but instead there are four minima located at the L-points [21]. The electron and hole masses are quite similar at these minima. Another interesting feature of lead-salt materials compared to the conventional III-V materials is that Auger recombination is lowered by two orders of magnitude; thus having more efficiency in long-wavelength emission. However, the lead-salt materials have comparatively low thermal conductances due to heavy atoms such as Pb and Sn. Therefore CW operating at room temperature is practically impossible [22].

1.2.3 Antimonide-based interband lasers

The InGa(Al)AsSb on GaSb, quantum-well structures are mainly used for laser emission in the 1.5 - 3 μm range [23-26]. High performance of InGaAsSb/AlGaAsSb/GaSb quantum-well lasers was demonstrated by Kim et al. at the emission wavelength of 2.8 μm with room-temperature CW operation [23]. However, this structure is problematic as far as for increasing the emission wavelength. In order to increase wavelength beyond 3 μm , the In composition should increase by more than 50%, and also the As composition should increase to maintain the balance of layer strain. In turn, this causes a reduction in the valence-band offset which leads to severe degradation of hole confinement. Due to this limitation in wavelength, type-II structures, which were theoretically proposed by Grein have been researched to obtain MIR laser emission [26]. Type-II quantum-well

lasers based on GaSb demonstrated 3.2-3.6 μm coherent light emission with CW operating temperature of 230 K [24]. However, the CW operating temperature of type II lasers is still relatively low and the emission wavelength is limited to values below 5 μm .

1.2.4 Interband cascade lasers

Interband cascade lasers (ICLs) were first proposed by Yang in 1995 [27] and their design was optimized by Meyer in 1996 [28]. Figure 2 shows the band diagram of a type-II interband cascade laser (ICL), which is based on the InAs/Ga_{1-x}In_xSb system.

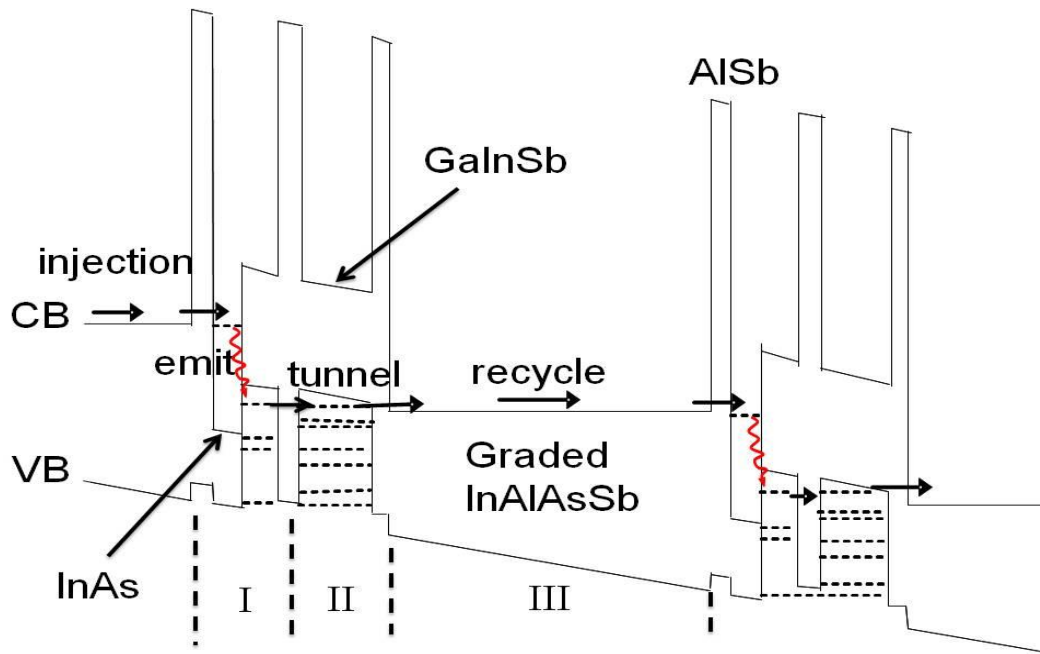


Figure 1.2: The conduction and valence band diagram of the type-II ICL at an applied electric field of 100 kV/cm, as proposed by Meyer in 1996 [28]. Each period is composed of an active region (I), electron barrier (II) and injection region (III).

The main advantage of ICLs is that one electron can emit N photons where N is the

number of periods of the ICL structure, while a conventional interband laser can emit only one photon for every injected electron. In addition, no phonon-relaxation path exists, since the device uses electron and hole recombination processes [29, 30]. In sharp contrast, for the intersubband transitions in QCLs, the nonradiative phonon-emission rate is ~ 1000 higher than the photon-emission rate between laser states. As shown in figure 1.2, electrons are injected to the ground state of an InAs well in active region by tunneling from a graded InAlAsSb injector region. The electrons in the conduction band of the active region make a transition with photon emission to the ground state of the valence band. The GaInAs and AlSb layers in the active region (i.e., the electron barriers) prevent tunneling from the ground laser state to the injector region or to the continuum band. This design was practically realized by Lin in 1997 [31]. The emission wavelength was $3.8 \mu\text{m}$ and the maximum operating temperature was 170 K in pulsed mode. Recently, ten-stage ICL devices were operated at room temperature with emission wavelengths of 4.1 and $4.3 \mu\text{m}$ [32].

References:

- [1] M. Kanskar, et al, “53% wallplug efficiency 975nm distributed feedback broad area laser”, Electronic Letters, Vol. 42, No. 25, (2006).
- [2] L. J. Mawst, et al, “High-power, Single-Mode, Al-Free InGaAs(P)/InGaP/GaAs Distributed Feedback Diode Lasers”, Journal of Crystal Growth, Vol.195, p. 609, (1998).
- [3] Jagadeeshwari Manne, et al, “Pulsed quantum cascade laser-based cavity ring-down spectroscopy for ammonia detection in breath”, Applied Optics, Vol. 45, No. 36, p. 9230, (2006).
- [4] Michael Pushkarsky, et al, “Compact mid-IR Breath Analysis System”, IEEE sensors, p.20, Oct (2007).
- [5] Rainer Martini et al, “Stability of near- and mid-infrared free-space optical links under strong scattering environment”, CLEO, Vol 1, p.2. , (2004)
- [6] Gordon, J.P., H.J. Zeiger, and C.H. Townes, “Molecular Microwave Oscillator and New Hyperfine Structure in the Microwave Spectrum of NH_3 ”, Physical Review, **95**(1): p. 282, (1954).
- [7] Gordon, J.P., H.J. Zeiger, and C.H. Townes, “The Maser-New Type of Microwave Amplifier, Frequency Standard, and Spectrometer”, Physical Review, **99**(4): p. 1264, (1955).
- [8] Schawlow, A.L. and C.H. Townes, “Infrared and Optical Masers”, Physical Review, **112**(6): p. 1940, (1958).
- [9] T. H. Maiman, “Optical and Microwave-Optical Experiments in Ruby”, Phys. Rev. Letters, 4, p. 564, (1960).
- [10] Hall, R.N., et al., “Coherent Light Emission From GaAs Junctions”, Physical

Review Letters, **9**(9): p. 366, (1962).

[11] Quist, T.M., et al., “Semiconductor MASER of GaAs”, Applied Physics Letters, **1**(4): p. 91-92, (1962).

[12] Nathan, M.I., et al., “Stimulated Emission of Radiation from GaAs p-n Junctions”, Applied Physics Letters, **1**(3): p. 62-64, (1962).

[13] Holonyak, J.N. and S.F. Bevacqua, “Coherent (Visible) Light Emission from GaAs_{1-x}P_x JUNCTIONS”, Applied Physics Letters, **1**(4): p. 82-83, (1962).

[14] Melngailis, I., “MASER action in InAs diodes”, Applied Physics Letters, **2**(9):p. 176-178, (1963).

[15] Butler, J.F., et al., “PbTe diode laser”, Applied Physics Letters, **5**(4): p. 75-77, (1964).

[16] Patel, C.K.N., “Interpretation of CO₂ Optical Maser Experiments”, Physical Review Letters, **12**(21): p. 588, (1964).

[17] Patel, C.K.N., “Continuous-Wave Laser Action on Vibrational-Rotational Transitions of CO₂”, Physical Review, **136**(5A): p. A1187, (1964).

[18] Faist, J., et al., “Quantum Cascade Laser”, Science, **264** (5158): p. 553-556, (1994).

[19] http://plasmalabs.com/production/CO2_lasers/47/

[20] A. A. Ioain, A. A. Kotkov. A. K. Kurnorov, A. P. Napartovieh, L. V. Selezoev, N. G. Torkin, “First overtone CO laser with suppressed fundamental band lasing”, Lasers and Electro-Optics Europe, p. 332, Sep (1998).

[21] Tacke, M., “Lead-Salt Lasers”, Philosophical Transactions, Mathematical, Physical and Engineering Sciences, **359**(1780): p. 547-566, (2001).

[22] Z. Shi, et al., “Midinfrared lead salt multi-quantum-well diode lasers with 282 K

operation”, Appl. Phys. Lett., Vol. 66, p. 2537, (1995).

[23] Kim, J.G., et al., “High-power room-temperature continuous wave operation of 2.7 and 2.8 μm In(Al)GaAsSb/GaSb diode lasers”, Applied Physics Letters, **83**(10): p. 1926-1928, (2003).

[24] C. L. Canedy, et al, “cw midinfrared “W” diode and interband cascade lasers”, J. Vac. Sci. Technol. B, vol.24, p. 1613, (2006).

[25] Lin, C., et al., “Low threshold room-temperature continuous-wave operation of 2.24-3.04 μm GaInAsSb/AlGaAsSb quantum-well lasers”, Applied Physics Letters, **84**(25): p. 5088-5090, (2004).

[26] Grein, C.H., P.M. Young, and H. Ehrenreich, “Theoretical performance of InAs/In_xGa_{1-x}Sb superlattice-based midwave infrared lasers”, Journal of Applied Physics, **76**(3): p. 1940-1942, (1994).

[27] Yang, R.Q., “Infrared laser based on intersubband transitions in quantum wells”, Superlattices and Microstructures, **17**(1): p. 77, (1995).

[28] Meyer, J.R., et al., “Type-II and type-I interband cascade lasers”, Electronics Letters, **32**(1): p. 45-46, (1996).

[29] E. R. Youngdale, J. R. Meyer, C. A. Hoffman, and F. J. Bartoli, P. M. Young and H. Ehrenreich, R. H. Miles and D. H. Chow, “Auger lifetime enhancement in InAsGa_xIn_{1-x}Sb superlattices”, Appl. Phys. Lett., Vol. 64, (23), pp. 3160-3162, (1994).

[30] C. H. Grein, P. M. Young and H. Ehrenreich, “Theoretical performance of InAs/In_xGa_{1-x}Sb superlattice-based midwave infrared lasers”, J. Appl. Phys., **76**, pp. 1940-1942, (1994).

[31] Chih-Hsiang, L., et al., “Type-II interband quantum cascade laser at 3.8 mm”,

Electronics Letters, Vol. **33**(7): p. 598-599, (1997).

[32] Canedy, C.L., et al., "High-temperature interband cascade lasers emitting at $\lambda = 3.6$ -
4.3 mm", Applied Physics Letters, Vol. **90**(18): p. 181120-3, (2007)

Chapter 2

Theoretical background for quantum cascade lasers

2.1 General introduction

The first quantum cascade laser (QCL) was realized by Faist et al. of Bell Labs in 1994 [1]. The concept of intersubband laser was originally proposed in 1971 by Kazarinov and Suris [2]. They proposed amplifying an electromagnetic wave generated via intersubband transitions in superlattices. Figure 2.1 shows the conduction band diagram of the photon-assisted relaxation process which was proposed by Kazarinov and Suris. The electron in ground state (level 1) of the n^{th} well can transit to the first excited state (level 2) of the $n+1^{\text{th}}$ well by photon-assisted tunneling. The population inversion condition is satisfied, where the ground state of the n^{th} well has larger electron sheet density than that in level 2 of the $n+1^{\text{th}}$ well.

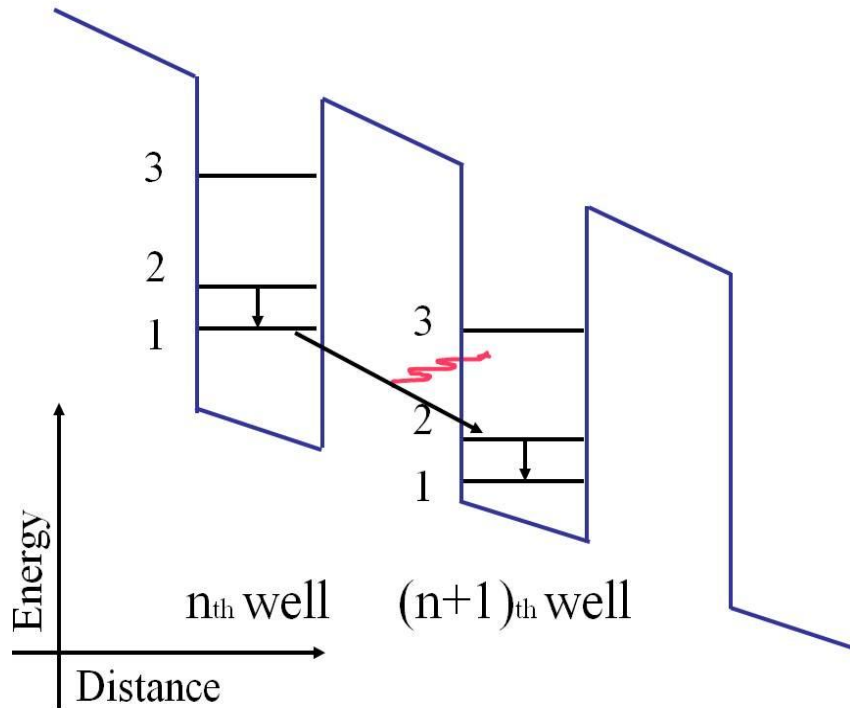


Figure 2.1: The conduction band diagram of the photon-assisted tunneling proposed by Kazarinov and Suris [2]. A photon is emitted via inter-well photon-assisted tunneling transition between the ground state (level 1) of n^{th} well and the first excited state (level 2) of $(n+1)^{\text{th}}$ well.

In this theory, each injected electron generates N photons at currents above the threshold-current density, where N is the number of stages. This fundamental aspect of QCLs has significant advantages compared to conventional interband-transition lasers. The active region of conventional semiconductor lasers is electrically pumped in parallel, so the gain is limited by the ratio of the effective transit time, which includes carrier capture and the recombination time. As a result, the number of quantum wells is limited to 5 to 10. On the contrary, the number of stages of a quantum cascade structure is limited only by the ratio between the effective width of the optical mode and the length of an

individual stage. Therefore, in general QC structures have 30 to 40 stages.

2.2 Theoretical frame work for quantum cascade lasers

The dipole matrix element, z_{ij} , between state i and j is defined [3] as:

$$z_{ij} = \langle \varphi_i | z | \varphi_j \rangle \quad (2.1)$$

where z is position operator about the growth direction of quantum well, and φ_i and φ_j are the wavefunctions at the i and j states, respectively. Sirtori calculated the dipole matrix element by using a two-band model [4].

$$z_{ij} = \frac{\hbar}{2(E_j - E_i)} \langle \varphi_i | p_z \frac{1}{m^*(E_i, z)} + \frac{1}{m^*(E_j, z)} p_z | \varphi_j \rangle, \quad (2.2)$$

where E_i and E_j are the energy of the electron at the state i and j respectively. p_z is momentum operator which can be expressed by:

$$p_z = -i\hbar(\partial / \partial z), \quad (2.3)$$

and $m^*(E_i, z)$ is the effective mass which is defined as [5]:

$$m^*(E_i, z) = m^*(E=0) \left(1 + \frac{E - V(z)}{E_G} \right), \quad (2.4)$$

where $V(z)$ is the conduction band edge at position z and E_G is energy bandgap of the material. E_G has a relation with a nonparabolicity coefficient γ , which equation is:

$$\gamma^{-1} = 2m^* E_G / \hbar^2 \quad (2.5)$$

The wavefunction φ_i and φ_j can be normalized to:

$$1 = \langle \varphi_i | 1 + \frac{E - V(z)}{E - V(z) + E_G(z)} | \varphi_i \rangle. \quad (2.6)$$

The dipole matrix element is a very important factor for the QCL design because the square of dipole matrix element between laser states is directly proportional to the gain in the active region. Another important factor in QCL design is the optical-phonon scattering time. The condition of population inversion is a significant challenge for intersubband-transition devices, since optical-phonon emission is the dominant scattering mechanism between subbands whose energy separation is more than the optical-phonon energy. The optical-phonon emission leads to lifetimes of the order of picoseconds compared to the lifetimes associated with radiative transitions, which are of the order of nanoseconds. Therefore optical-phonon emission is a dominant part of electron transitions in QCLs. The electron is assumed to be at $k_{\parallel} = 0$ because the excited-states densities are very low, so the optical phonon-scattering ratio is expressed by:

$$\frac{1}{\tau_{if}} = \frac{m^* e^2 \omega_{LO}}{2\hbar^2 \varepsilon_p q_{if}} \int dz \int dz' \varphi_i(z) \varphi_f(z) e^{-q_{if}(z-z')} \varphi_i(z') \varphi_f(z') \quad (2.7)$$

where the momentum (q_{if}) is:

$$q_{if} = \sqrt{\frac{2m^*(E_{if} - \hbar\omega_{LO})}{\hbar^2}}. \quad (2.8)$$

For optical-phonon absorption, the momentum is exchanged to:

$$q_{if} = \sqrt{\frac{2m^*(E_{if} + \hbar\omega_{LO})}{\hbar^2}}. \quad (2.9)$$

The radiative rate $(\tau_{spont})^{-1}$ for spontaneous photon emission in a single polarization mode is expressed by

$$(\tau_{spont})^{-1} = \frac{q^2 n}{6\pi c^3 \varepsilon_0 \hbar^3} E_{ij}^3 z_{ij}^2, \quad (2.10)$$

where c is light velocity, n is refractive index, ε_0 is vacuum permittivity, and q is the electronic charge. This procedure shows good agreement with the measurement of the intersubband scattering rate in InGaAs-AlInAs superlattices [6]. For the intersubband transitions in QCLs, the radiative efficiency of the upper laser level is significantly lower ($< 10^{-3}$), since most electrons relax within ~ 1 ps through non-radiative optical phonon

emission [7]. Therefore, optimum values for $(\tau_{spont})^{-1}$ and $(\tau_{if})^{-1}$ are very important in order to achieve low threshold-current density.

2.3 The quantum cascade laser

Figure 2.2 shows the conduction band diagram of a conventional, 3 QW QCL structure. It has many stages and each stage consists of an injector/Bragg reflector region and an active region. The active region where population inversion and gain occurs has three energy states (i.e., states 1, 2 and 3).

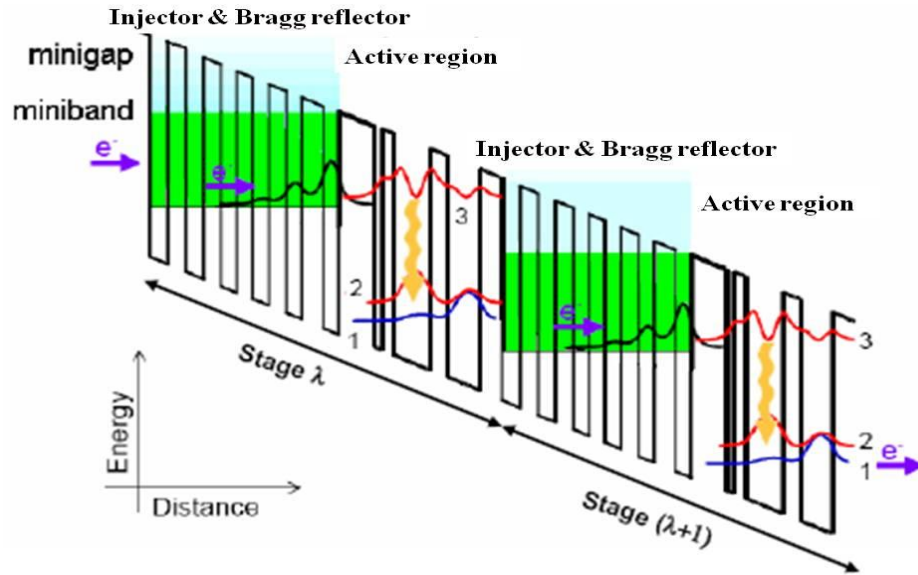


Figure 2.2: Conduction band diagram of general QCL structure. Each stage consists of an injector/Bragg-reflector region and an active region. Electrons are moving from left to right and a wavy arrow indicates the photon emission. Energy states 3 and 2 are the upper and lower laser levels, respectively and the energy state 1 is separated by one phonon energy from energy state 2 and thus it helps depopulating the lower laser level.

The population inversion condition is satisfied if $\tau_{32} > \tau_2$ where τ_{32}^{-1} is the nonradiative scattering rate from the second excited state (state 3) to the first excited state (state 2) and τ_2^{-1} is the total scattering rate out of state 2. τ_2 is computed via the scattering rate $1/\tau_{21}$ which is expressed in equation 2.7. If the population inversion condition is satisfied, the electrons are injected into state 3, relax to state 2 with photon emission and subsequent stimulated emission occurring. The electrons from state 2 transit to the ground state (state 1) via phonon-assisted relaxation, and after tunneling to the injector/Bragg-reflector region move to the next active region. The energy separation between states 2 and 1 corresponds to the phonon energy of the semiconductor material, and the wavelength of the QCL is determined by bandgap engineering of the active region. QCL structures are classified into vertical- and diagonal-transition types depending on the nature of the transition between the state 3 and state 2 (i.e., the upper and lower laser levels). A vertical-type transition has strong overlap between states 3 and 2, whereas a diagonal-type transition has reduced overlap. These transitions will be further discussed in the next chapter. The active region is normally undoped because doping introduces a tail of impurity states which results in the broadening of the laser transition [8]. The injector/Bragg-reflector region has a lower (- energy) miniband and a minigap as seen in figure 2.2. The lower miniband enables electron transfer from states 1 and 2 through the injector region, and injection into the upper laser level of the next stage; while the minigap prevents electrons from escaping from state 3 to the continuum. The injector region has to be doped to weaken the space charge buildup which will happen when the electrons are injected directly from the contact. The doping is restricted to only the

central part of each injector to separate the electrons in the injector ground state from parent donors and thus enhance injection efficiency.

2.4 The diagonal-transition design for the active region

Figure 2.3 shows the conduction band diagram of the first operated QCL, which had a diagonal-transition design [1]. The 3-coupled quantum wells are located in the active region. The wavefunctions of the upper laser level (state 3), lower laser level (state 2) and ground level (state 1) peak in the first, second and third quantum well of the active region, respectively. This means that the laser transition occurs from the first well to the second well though a photon-assisted tunneling process.

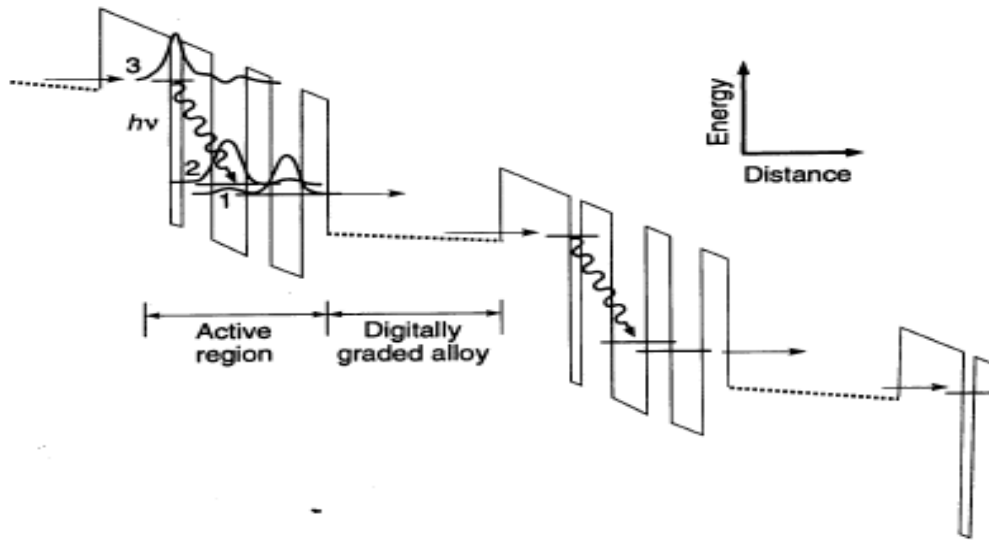


Figure 2.3: The first operated Quantum Cascade Laser structure in 1994 [1]: calculated conduction band diagram of $\text{Ga}_{0.47}\text{In}_{0.53}\text{As}$ (well) and $\text{Al}_{0.48}\text{In}_{0.52}\text{As}$ (barriers) under an applied electric field. State 3 is the upper laser level, state 2 is the lower laser level and state 1 is the ground level. The dashed lines correspond to the digitally graded injector

which helps the injection of electrons into the upper laser level of the next stage.

The diagonal design has a relatively long lifetime for the state 3 due to the reduced wavefunction overlap with state 2 [9]. In addition, the escape rate from the state 3 to the continuum state can be significantly reduced because the peak of the upper-energy-level wavefunction is located in the first well of the active region; that is, relatively far from the continuum in the next stage. However, there are several disadvantages associated with the diagonal-transition design. First, the overlap between the two laser levels is low, so the dipole matrix element, which is an important factor for the threshold-current density, is reduced. Second, the injected electron has to tunnel through a barrier to emit a photon. Even though the epitaxial growth systems are well optimized and developed, the heterostructure interfaces are not free from the roughness and impurities, which in turn lead to broadening of the gain spectrum [9-11].

2.5 The vertical-transition QCL structure

The vertical-transition design of the active region has a narrower gain spectrum compared to the diagonal-transition design, since the upper and lower laser levels are located in the same wells. A narrower gain spectrum can thus provide lower threshold-current density.

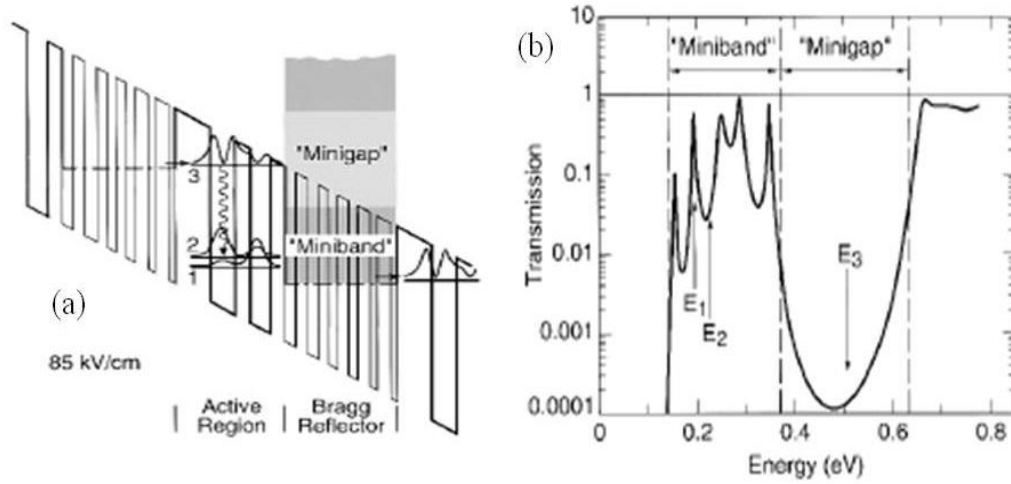


Figure 2.4: (a) Schematic of calculated conduction band diagram and relevant wavefunctions under applied electric field of 85 kV/cm. State 3 is the upper laser level, and state 2 is lower laser level. The lower miniband causes electron extraction from states 2 and 1 and injection into the upper laser level of the next stage, while the minigap prevents electrons from escaping from state 3 to the continuum. (b) The electron transmission of the superlattice vs. energy. E1, E2 and E3 indicate the electron energies for states 3, 2 and 1, respectively.

Figure 2.4 shows the first operated vertical-transition QC laser which included a superlattice for Bragg reflection in the injector region [12]. The Bragg reflector in the vertical-transition design prevents the escape of electrons from the upper laser level (state 3), thus enhancing population inversion between laser levels. However, the initial QCLs with vertical-transition design suffered from carrier “backfilling” effects into the lower laser level from the next injector region, because of the relatively large doping in the injector and a small energy separation, ΔE (i.e., ~ 30 meV), between the lower laser level

(state 2) and the next-injector ground state [12, 13]. Further designs of increased ΔE (i.e. ~ 100 meV) significantly reduced the threshold-current density of QCLs [13].

2.6 Double-phonon resonance design for the active regions of QCLs

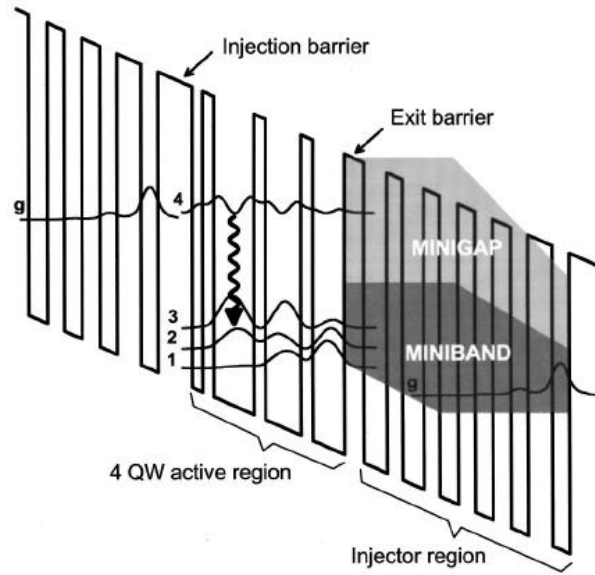


Figure 2.5: The schematic diagram of calculated conduction band and key wavefunctions in active region. The active region consists of 4 QWs [14]. The energy separations between states 3 and 2 and states 2 and 1 correspond to the phonon energy in the semiconductor.

Figure 2.5 shows the first QC design with double-phonon resonance design for the active region [14]. Electron extraction from the lower laser level (state 3) to the next injector is significantly improved by using two energy states, each separated from each other by a phonon energy. As a result a very short lifetime is obtained for the lower laser level. Moreover, the insertion of a first thin barrier layer in the active region reduces the

wavefunction overlap between the ground state of the injector and states 3, 2 and 1, thus providing good injection efficiency to the upper laser level (state 4). This design is a strain compensated structure which consists of $\text{In}_{0.40}\text{Ga}_{0.60}\text{As}$ compressive strained quantum wells and $\text{Al}_{0.56}\text{In}_{0.44}\text{As}$ tensile strained barriers, which in turn increases the conduction band offset from 560 meV (i.e., the band offset of the structure lattice-matched to the InP substrate) to 620 meV [14].

2.7. The rate equations

In this section we present the formulas for the key parameters which enable predicting the device performance. Figure 2.6 shows the schematic diagram of the conduction band for a three-level system QCL, which includes the injector with doping sheet density n_g . The lasing transition occurs between states 3 and 2 with carrier sheet densities of n_3 and n_2 , respectively. The carrier sheet density of the ground state (n_1) is neglected for simplicity.

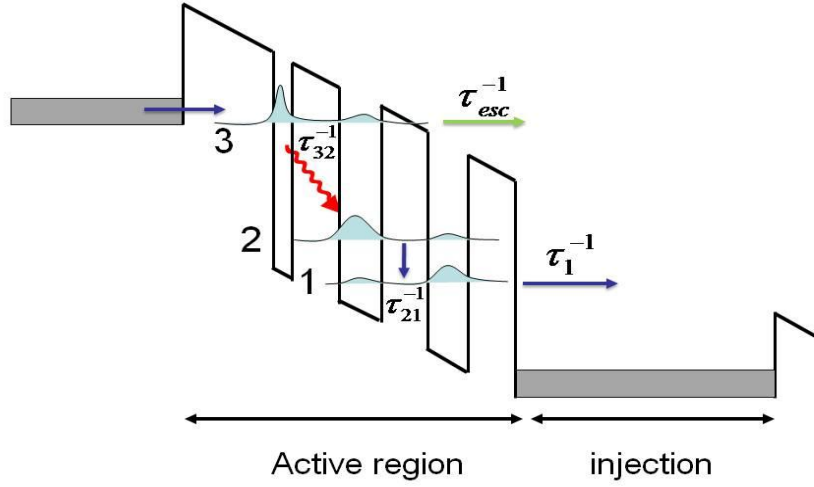


Figure 2.6: Conduction band of the three-level system of the QCL structure. The wavy arrow indicates photon emission and other arrows indicate tunneling and the relaxation process from state 2 to state 1. The gray region is the region below the quasi-Fermi level in the injection region. The upper laser level is state 3, lower laser level is state 2 and the ground level is state 1.

The total electronic scattering rate out of the state 3 can be written as such:

$$\tau_3^{-1} = \tau_{32}^{-1} + \tau_{31}^{-1} + \tau_{esc}^{-1}. \quad (2.11)$$

where τ_{esc}^{-1} is the electron escape rate into the continuum via tunneling, and τ_{32}^{-1} and τ_{31}^{-1} are optical-phonon emission rates to state 2 and state 1, respectively. These values can be deduced from equation 2.7. Similarly, the electron scattering rate from state 2 to state 1 and to the injection region is

$$\tau_2^{-1} = \tau_{21}^{-1} + \tau_{2g}^{-1} \quad (2.12)$$

where τ_{2g}^{-1} and τ_{21}^{-1} are the optical-phonon emission rates from state 2 to the injection region and from state 2 to the state 1, respectively. The rate equations which are related to the photon density, and the sheet densities n_3 and n_2 can be expressed [3] by:

$$\frac{dn_3}{dt} = \frac{J}{e} - \frac{n_3}{\tau_3} - Sg_c(n_3 - n_2), \quad (2.13)$$

$$\frac{dn_2}{dt} = \frac{n_3}{\tau_3} + Sg_c(n_3 - n_2) - \frac{n_2}{\tau_2}, \quad (2.14)$$

$$\frac{dS}{dt} = \frac{c}{n} [Sg_c(n_3 - n_2) - \alpha S]. \quad (2.15)$$

where g_c is the gain cross-section, c is the light velocity in vacuum, S is the photon flux density, and J is the current density. The gain cross-section, assuming a Lorentzian lineshape, can be written [3] as:

$$g_c = \frac{4\pi e^2 z_{32}^2}{\lambda_0 \epsilon_0 n L_p (2\gamma_{32})}, \quad (2.16)$$

where λ_0 is the wavelength, ϵ_0 is the electric permittivity in vacuum, e is electron charge, z_{32} is the dipole matrix element between states 3 and 2, L_p is the a period length of the QC structure, and γ_{32} is the full-width at half maximum of the laser transition between states

3 and 2. The peak material gain for the laser transition (i.e., state 3 to state 2) in steady state can be expressed by:

$$G_p = g_c(n_3 - n_2) = \frac{4\pi e^2 z_{32}^2}{\lambda_0 \epsilon_0 n L_p (2\gamma_{32})} J \tau_3 \left(1 - \frac{\tau_2}{\tau_{32}}\right), \quad (2.17)$$

and then the modal gain is defined by: $G_M = G_p \Gamma$, where Γ is the transverse-waveguide optical-mode confinement factor, and the modal gain coefficient g_M is defined as $g_M = G_M/J$, which can be written as

$$g_M = \frac{4\pi e^2 z_{32}^2 \Gamma}{\lambda_0 \epsilon_0 n L_p (2\gamma_{32})} \tau_3 \left(1 - \frac{\tau_2}{\tau_{32}}\right). \quad (2.18)$$

As seen in equation 2.17, the gain of QCL is directly proportional to the upper laser level lifetime and the square of the optical matrix element between the laser states. The laser threshold condition is satisfied when the modal gain equals the sum of all cavity losses and reads as such:

$$g_M J_{th} = \frac{\alpha_m + \alpha_w}{\Gamma} \quad (2.19)$$

where α_m is the mirror loss coefficient and α_w is the waveguide loss coefficient. Therefore, the laser threshold-current density can be derived from equations 2.18 and 2.19:

$$J_{th} = \frac{1}{\tau_3 \left(1 - \frac{\tau_2}{\tau_{32}}\right)} \frac{\lambda_0 \epsilon_0 n L_p (2\gamma_{32})}{4\pi e^2 z_{32}^2} \frac{\alpha_w + \alpha_m}{\Gamma} \quad (2.20)$$

2.8 Thermal effects

Conventional QCLs suffer from thermal problems, and as a result the wallplug efficiency is quite low (< 12 %) at room temperature (RT) [15]. Moreover their CW electro-optical characteristics are extremely temperature sensitive due to the carrier backfilling into the lower laser state, and due to carrier leakage out of the upper laser level as seen in figure 2.7.

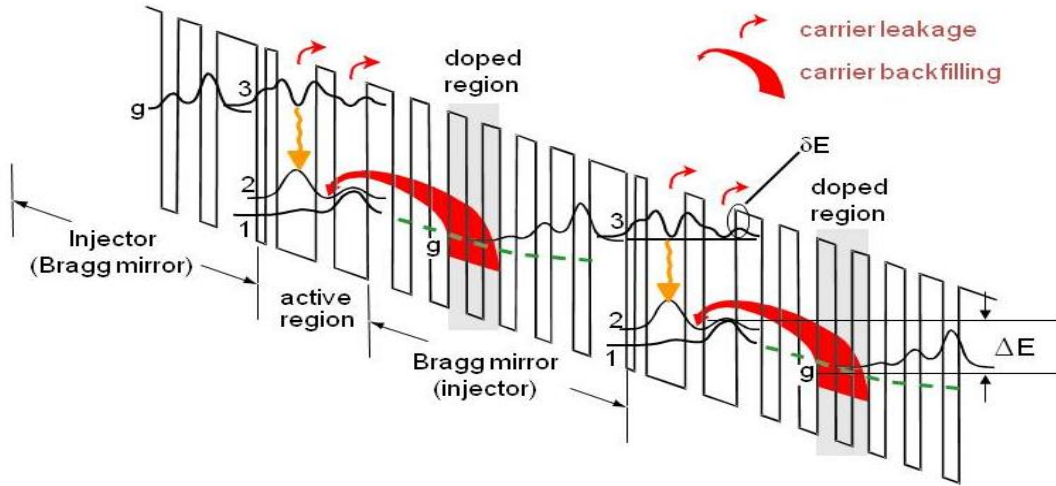


Figure 2.7: Conduction band diagram of the conventional QC structure: g is ground state of the injector. States 3 and 2 are the upper and lower laser level, respectively. Rising the temperature increases both carrier leakage from the upper laser level and carrier backfilling into the lower laser level from the next-stage injector.

The effective energy barrier for electrons in the upper laser level, δE , is the energy separation between the upper laser level and the top of the exit barrier. Its value indirectly determines the rate of escape of electrons from the upper laser level to the continuum. Another important issue as far as QCL operation above RT is carrier backfilling. The energy separation between the lower laser level and the quasi-Fermi level of the next injector region, ΔE , determines the degree of thermal backfilling of the lower laser level (Fig. 2.7). This carrier backfilling can be expressed by [11]:

$$n_2^{thermal} \cong n_{inj} e^{-\frac{\Delta E}{kT}}, \quad (2.21)$$

where $n_2^{thermal}$ is the thermal population of lower laser state and n_{inj} is the sheet density of injector. The ΔE value is generally designed to be ~ 150 meV, because a smaller value would lead to increased backfilling (See equation 2.21) and a larger value leads to high operating voltage which in turn decreases the wallplug efficiency of the device. The carrier-leakage and backfilling processes increase the threshold-current density, thus increasing the temperature of the active region of QCL in CW operation which in turn will further increase the threshold-current density. This is well known as a thermal runaway process. Moreover, the scattering rate of optical-phonon emission (i.e., inelastic scattering) between the upper and lower laser states is also affected by the temperature, and can be expressed by:

$$\tau^{-1}(T) = \tau^{-1}(0) \left[\frac{1}{\exp(\hbar\omega_{lo} / kT) - 1} + 1 \right], \quad (2.22)$$

where $\hbar\omega_{lo}$ is the LO phonon energy and $\tau^{-1}(0)$ is the scattering rate at a temperature of 0 K. To experimentally characterize the lasers, the device characteristics can be fitted to:

$$J(T_{ref} + \Delta T) = J_{th}(T_{ref}) \exp(\Delta T / T_0) \quad (2.23)$$

and

$$\frac{dP}{dI}(T_{ref} + \Delta T) = \frac{dP}{dI}(T_{ref}) \exp(-\Delta T / T_1). \quad (2.24)$$

where $T_{ref} + \Delta T$ is the heatsink temperature, T_{ref} is the reference temperature, and T_0 and T_1 are the characteristic temperatures of the device. dP/dI is the slope efficiency of the laser. T_0 , which characterizes the threshold-current density, is affected by carrier backfilling and carrier leakage, T_1 , which characterizes the slope efficiency, is also affected by carrier backfilling and carrier leakage in the laser, as we shall see in chapter 5 from the derivation of modified equations for QCLs.

References:

- [1] Faist, J., et al., Quantum Cascade Laser. *Science*, **264** (5158): p. 553-556, (1994).
- [2] R. Kazarinov and R. A. Suris, “Amplification of electromagnetic waves in a semiconductor superlattice”, *Sov. Phys. Semicon.*, Vol. 5, pp. 707-709, (1971).
- [3] Liu, H.C. and F. Capasso, Intersubband transitions in quantum wells : Physics and Device Applications II. Semiconductors and Semimetals, ed. R.K. Willardson and E.R. Weber. Vol. 60. (2000), San Diego: Academic Press.
- [4] C. Sirtori, F. Capasso, J. Faist, and S. Scandolo, *Phys. Rev. B*, Vol. 50, 8663, (1994).
- [5] D. F. Nelson, R. C. Miller, and D. A. Kleinmann, *Phys. Rev. B* 35, 7770, (1987).
- [6] J. Faist, F. Capasso, C. Sirtori, D. L. Sivco, A. L. Hutchinson, S. N. G. Chu, and A. Y. Cho. *Appl. Phys. Lett.*, 63, 1354, (1993).
- [7] Chia-Fu Hsu, Jeong-Seok O, Peter Zory and Dan Botez, “Intersubband Quantum-Box Semiconductor Lasers” *IEEE IN QUANTUM ELECTRONICS*, Vol. 6, NO. 3, (2000).
- [8] J. Faist, F. Capasso, C. Sirtori, D. L. Sivco, A. L. Hutchinson, and A. Y. Cho. *Appl. Phys. Lett.* 65, 94, (1994).
- [9] Q. Yang, R. Lösch, W. Bronner, S. Hugger, F. Fuchs, R. Aidam, and J. Wagner, “High-peak-power strain-compensated GaInAs/AlInAs quantum cascade lasers ($\lambda \sim 4.6 \mu\text{m}$) based on a slightly diagonal active region design”, *Appl. Phys. Lett.*, Vol 93, 251110, (2008).
- [10] Gerald B. Stringfello, “Organometallic Vapor-Phase Epitaxy-Theory and Practice” Academic Press, (1999).
- [11] Liu, H.C. and F. Capasso, Intersubband transitions in quantum wells : Physics and Device Applications II. Semiconductors and Semimetals, ed. R.K. Willardson and E.R.

Weber. Vol. 60. (2000), San Diego: Academic Press.

[12] Faist, J., et al., “Vertical transition quantum cascade laser with Bragg confined excited state” Appl. Phys. Lett. Vol.66, 538, (1995).

[13] [Jérôme Faist](#), [Federico Capasso](#), [Carlo Sirtori](#), [Deborah L. Sivco](#), [Albert L. Hutchinson](#), and [Alfred Y. Cho](#), “[Continuous wave operation of a vertical transition quantum cascade laser above T=80 K](#)” Appl. Phys. Lett., Vol. 67, 3057, (1995).

[14] Daniel Hofstetter, Mattias Beck, Thierry Aellen, and [Jérôme Faist](#), “High-temperature operation of distributed feedback quantum-cascade lasers at 5.3 mm”, Appl. Phys. Lett. Vol 78, 22, (2001).

[15] A. Evans, J.Nguyen, S. Slivken, J.S.Yu, S. R. Darvish and M. Razeghi, Appl. Phys. Lett. 88, (2006) 051105.

Chapter 3

MOCVD crystal growth

3.1 Introduction

Metal Organic Chemical Vapor Deposition (MOCVD) has been used for semiconductor growth since 1968 [1] and now one of the most popular epitaxial crystal growth technology for commercial devices such as laser diodes, light emitting diodes, photodetectors, solar cells and bipolar transistors. The compound semiconductor laser diodes grown by MOCVD can cover Blue and ultraviolet region using GaN material, telecommunications wavelengths (1.3 – 1.55 μm) using InGaAsP, in the range 700 – 1100 nm using AlGaAs-GaAs-InGaAs and long wavelengths using antimonides (from 2 to 4 μm). However, the intersubband semiconductor lasers for the MIR and FIR region such as QCLs were initially grown by MBE [2, 3] because those structures need very abrupt interfaces and accurate layer thicknesses and composition. The MOCVD growth has many advantageous such as robust process, large scale, high growth rate and selective growth.

In this chapter, we have shown very accurate thickness and composition controls with very high material quality by MOCVD growth. As a result, the device performances grown by MOCVD are the same or better than the best results grown by MBE. We also introduce the Aixtron A-200 MOCVD system and characterization of the $\text{In}_x\text{Ga}_{1-x}$.

$x\text{As}/\text{Al}_x\text{In}_{1-x}\text{As}/\text{InP}$ material system which includes growth mechanisms, such as boundary-layer issues, doping, layer composition, growth rate and V/III ratio.

3.2 Reactor Gas Delivery,

The MOCVD system can be divided into a reactor gas delivery system and a reaction chamber. The reactor gas delivery system should be leak-free, very clean and stainless-steel tubing with electronic mass flow controller (MFC).

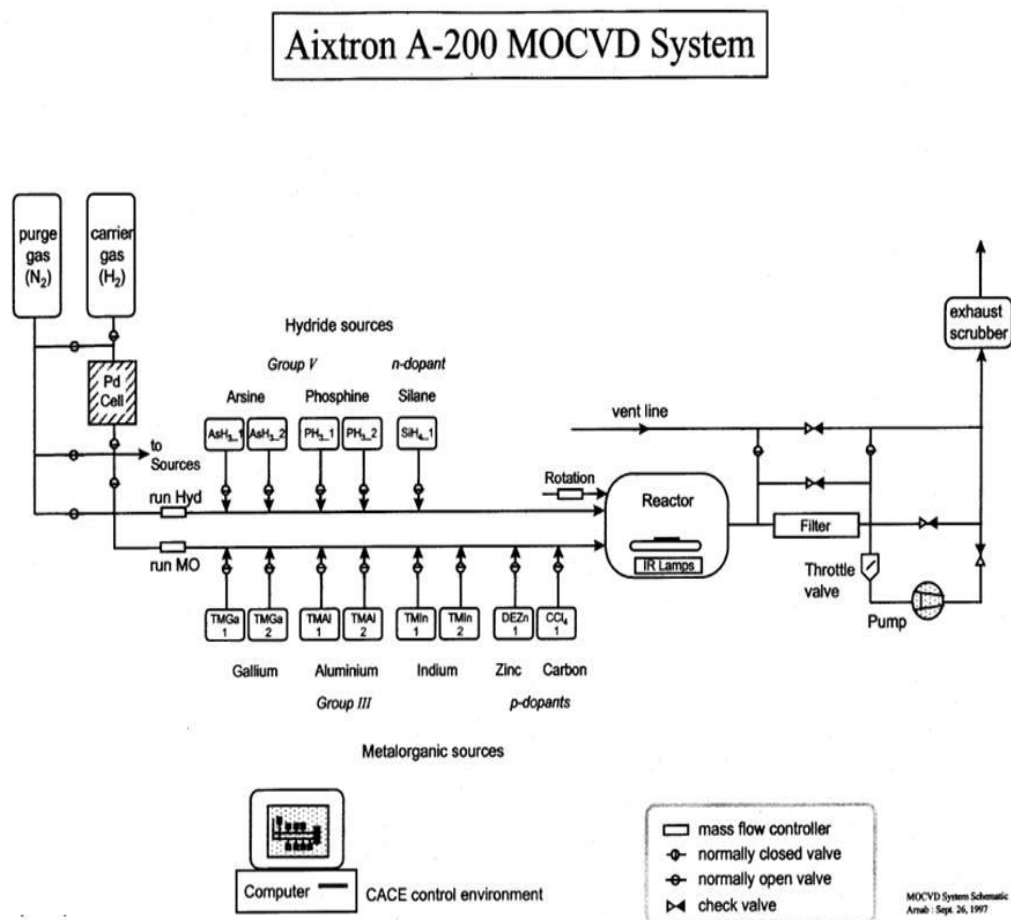


Figure 3.1: Schematic diagram of A-200 MOCVD reactor delivery system

Figure 3.1 shows that the schematic diagram of the gas delivery system of Aixtron A-200 MOCVD. The “run hyd” line is for supplying the Hydride gases such as Arsine (AsH_3), Phosphine (PH_3) or Silane (SiH_4) into the reactor, which are mixed with purified Hydrogen (H_2) which is controlled by the MFC and system manifold. The “run MO” line is for supplying the metal organics (MO) such as TriMethyl Gallium (TMGa), TriMethyl Indium (TMI), TriMethyl Aluminium (TMAI) into the reactor via MFC and the system manifold. The valves for controlling H_2 are normally closed, and the valves for controlling Nitrogen (N_2) are normally open due to the safety issue. The system is purged by Hydrogen during a resting state, but Electro-mechanical interlocking provides purging the reactor with only nitrogen if an electric power failure occurs. The MO Source materials are held in Stainless Steel Bubblers mounted in temperature controlled baths which temperature determines the source vapour pressure.

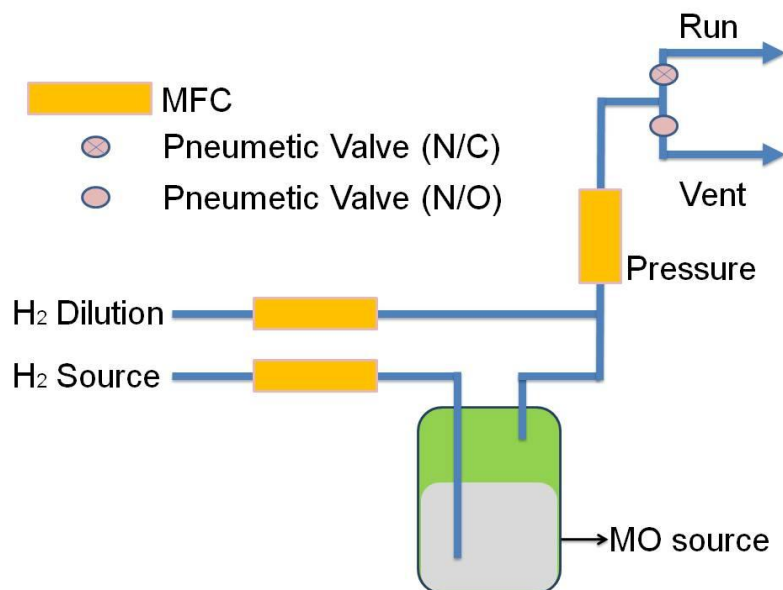


Figure 3.2: Schematic diagram of the MO source lines. The MO sources are generally kept as liquid in stainless-steel bubbler except TMIn which is kept as solid. The input connection tubing locates near the bottom of the bubbler under the surface of the MO sources.

The MO source lines near bubbler are shown in figure 3.2. The source input, dilution and output are controlled by the MFC with a carrier gas of H_2 . The material transport from the bubbler into the reactor is determined by the mass flow of the source, dilution and pressure and the vapor pressure of the MO source. Similarly, the hydride gas enters the system manifold from a gas cylinder in storage cabinet. The input pipes are double walled, leak-free and stainless-steel tubing. The hydrides flows are determined by the mass controls of the source, push and pressure as seen in figure 3.3. Table 3.1 shows hydrides and MO sources which are equipped in A-200 MOCVD and the vapor pressure of the MO sources with a storage temperature. The vapor pressure of the MO source is an important value to calculate growth rate which is expressed in equation 3.4.

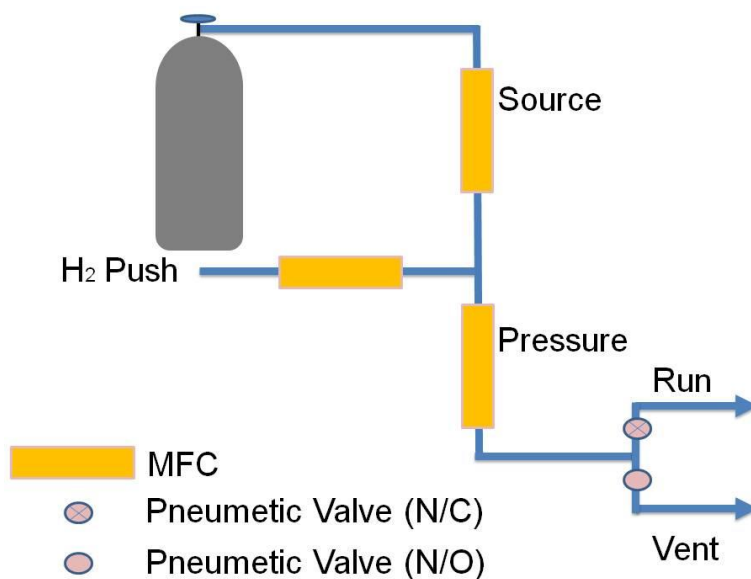


Figure 3.3: Schematic diagram of the hydride lines. The hydride gas cylinder is connected to the double wellled stainless-steel line and output gas is controlled by MFC.

Table 3.1: The group III sources and vapor pressure with storage temperature, group V sources and dopant of MOCVD A-200 system

Sources	vapor pressure (storage temperature)	
Trimethylgallium (TMGa)	39.7 mm Hg	(-10 °C)
Triethylgallium(TEGa)	4 mm Hg	(17 °C)
Trimethylaluminum (TMAI)	7.5 mm Hg	(17 °C)
Trimethylindium (TMIn)	0.9 mm Hg	(17 °C)
Trimethylantimony (TMSb)	31.2 mm Hg	(0 °C)
Arsine (AsH ₃)		
Phosphine (Ph ₃)		
Silane (SiH ₄)		

3.3 Reaction chamber

A-200 MOCVD system has a horizontal reactor in which the source gases are mixed and reacted. The reactor of A-200 system shown in Figure 3.4 is made with quartz and heated by infrared radiant.

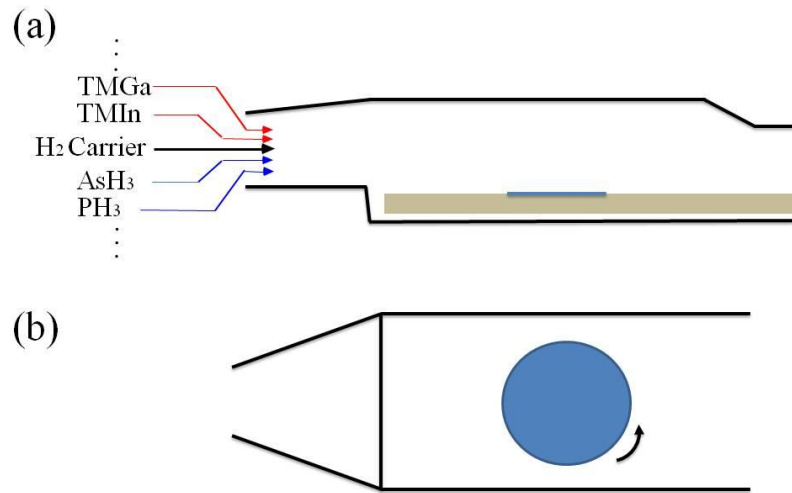
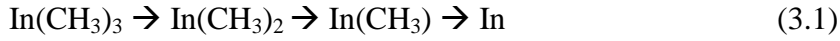


Figure 3.4: Schematic diagram of A-200 Horizontal reactor: (a) side view (b) top view. MO sources and hydrides flows from left side with H₂ carrier gas. The wafer rotation is controlled by H₂ flows.

The growth mechanism including mixed gas reaction in the chamber is important for understanding of growth rate, composition and superlattice interface. We list group III and group V materials in Table 3.1. The group III molecule such as TMIn, TMGa and

TMAI has relatively weak bonding, so pyrolysis occurs at fairly low temperatures [4-6].

The pyrolysis of TMIn ((CH₃)₃In) can be occurred follow order [5]

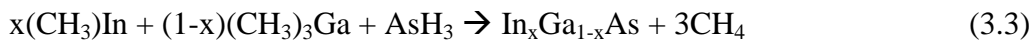


Then a simple case of pyrolysis reaction in the reaction chamber between

TMIn((CH₃)₃In) and Ph₃ can be expressed [5] by



The InP is combined with the surface of the wafer in the reactor and 3CH₄ will be vent to the exhaust line. The ternary alloy such as In_xGa_{1-x}As has a similar bonding equation which can be expressed [5] by



The ratio of TMIn and TMGa source determine the composition.

3.4 Growth temperature

The optimum MOCVD growth temperature of the III-V semiconductor is in the range of 600 – 800 °C except GaN which might be grown at much higher temperature [4]. The temperature inside the reactor determine not only the growth rate but also material

qualities such as interface roughness since the growth temperature affects the carrier gas velocity and source molecule reaction. If the growth temperature is too low, the pyrolysis efficiency of the group III and V is low and reaction rate is limited. On the contrary, if the growth temperature is too high, the solid particulate can be form without deposition on the wafer and it leads to reduced growth rate [3, 7]. In our system (A-200) growth temperature was set at 638 °C for the all $\text{In}_x\text{Ga}_{1-x}\text{As}$ and $\text{Al}_x\text{Ga}_{1-x}\text{As}$ layers on InP, since it shows not only the abrupt interface which is confirmed by x-ray diffraction but also high mobility which is inspected by Hall effect measurement.

3.5 Growth rate and layer composition

The each stage of the deep-well QC structure is composed of seven different composition layers, thus needing very accurate thickness and composition controls. The growth rates are determined by growth temperature, flow rate of the carrier gas, and vapor pressure of the MO sources. Assuming enough group V is supplied and all of the MO sources which flows into the reactor form a solid material in surface area, then the growth rate of the binary material can be expressed by [4]

$$R_g = \frac{W_m V_{mo} F_c}{k T D A_p} \quad (3.4)$$

where W_m is the molecular weight compound, V_{mo} is vapor pressure of MO source, F_c is flow rate of carrier gas (i.e., H_2), k is Boltzmann's constant, T is the growth temperature,

D is the solid density and A_e is effective area. The growth rate of the ternary can be simply given by the sum of the binary growth rate

$$R_g (C) = R_g (A) + R_g (B). \quad (3.5)$$

However, the growth rate equations are not well-matched with the experimental results since the all MO source supplied to the system will not interact only the wafer surface area. In addition, the TMIn is a solid source and it is well known that the vapour pressure of TMIn changes as the surface area changes with consumption [8]. The figure 3.5 shows that TMIn vapor pressure changes as the number of growths increases [9].

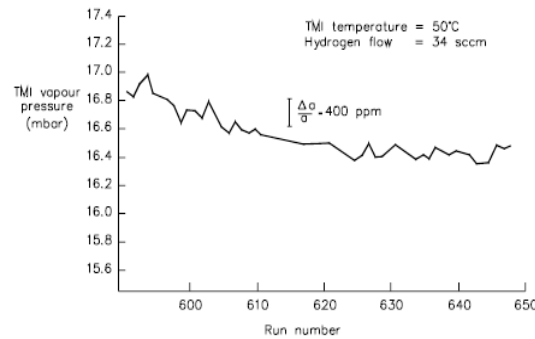


Figure 3.5: Vapor pressure of TMIn at 50 °C of the bath temperature vs. run number [9].

To find very accurate growth rate, the X-ray diffraction (XRD) which is very strong tool for characterization of materials including superlattice (SL) is experimentally performed. Inspection of XRD spectra gives a lot of information such as the thickness, strain, composition, material quality and interface abruptness [10, 11]. For each layer calibration of the deep-well QC structure, 5-period superlattices of InP/ $\text{In}_x\text{Ga}_{1-x}\text{As}$ or InP/ $\text{Al}_x\text{In}_{1-x}$.

x As were grown. To avoid strain relaxation, $\text{In}_x\text{Ga}(\text{Al})_{1-x}\text{As}$ or $\text{In}_x\text{Al}_{1-x}\text{As}$ layer thicknesses were maintained to less than 200 Å and the InP thickness was fixed to 500 Å. The grown structures were measured by High resolution x-ray diffraction (HRXRD) and compared with simulated spectra.

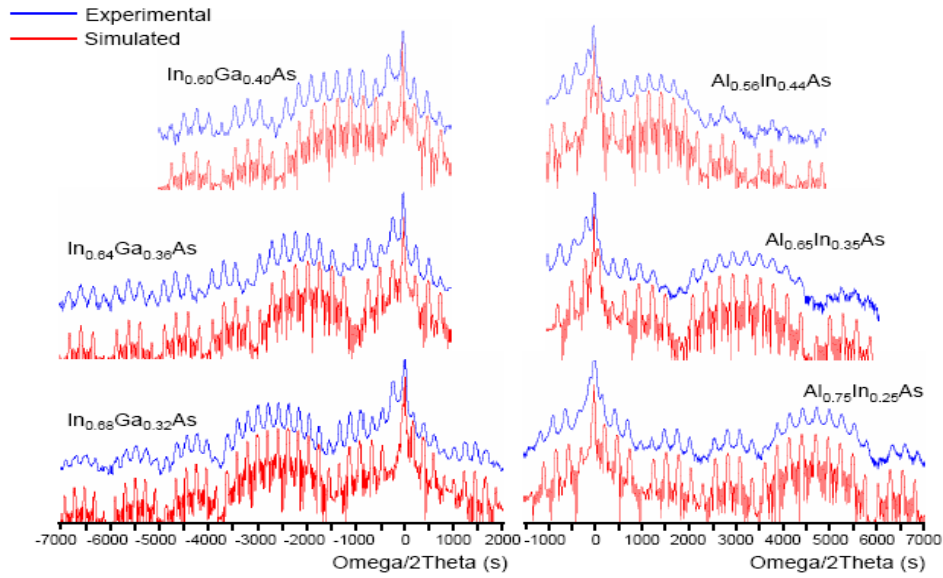


Figure 3.6: Experimental and simulated XRD (0 0 4) reflection spectra for a 5- period superlattice composed of alternating layers of $\text{In}_x\text{Ga}_{1-x}\text{As}/\text{InP}$ or $\text{Al}_x\text{In}_{1-x}\text{As}/\text{InP}$.

Figure 3.6 shows the experimental and simulated x-ray diffraction spectra of 5-period of $\text{In}_x\text{Ga}(\text{Al})_{1-x}\text{As}/\text{InP}$ or $\text{In}_x\text{Al}_{1-x}\text{As}/\text{InP}$ superlattice. The blue lines and red lines are experimental and simulation spectra, respectively. The simulation spectra were obtained from the X'Pert Epitaxy software of Panalytical. We deduced the thickness of a period of the superlattice (SL) from the satellite x-ray peaks. Also, the composition of ternary was informed by comparing the satellite peak envelopes in experimental and simulation spectra [12]. However for the highly strained layers (i.e., $\text{In}_{0.68}\text{Ga}_{0.32}\text{As}$ and $\text{Al}_{0.75}\text{In}_{0.25}\text{As}$) it is

difficult to accurately determine their thickness by using such structures, since their total thickness (in 5-period SLs) is limited by the critical thickness. That is, in such SL structures, the total thickness of the highly strained layers in each period has to be maintained to 40-50 Å (the thickness of InP layers is ~ 500 Å) to prevent strain relaxation. Thus, we found it difficult to accurately determine those layers' thickness from XRD spectra. Therefore we grew 5-period, strain-compensated SLs of: (a) $\text{Al}_{0.75}\text{In}_{0.25}\text{As}$ (96 Å)/ $\text{In}_{0.60}\text{Ga}_{0.40}\text{As}$ (391 Å) and (b) $\text{In}_{0.68}\text{Ga}_{0.32}\text{As}$ (92 Å)/ $\text{Al}_{0.56}\text{In}_{0.44}\text{As}$ (182 Å). The measured XRD spectra are shown in Fig. 3.7.

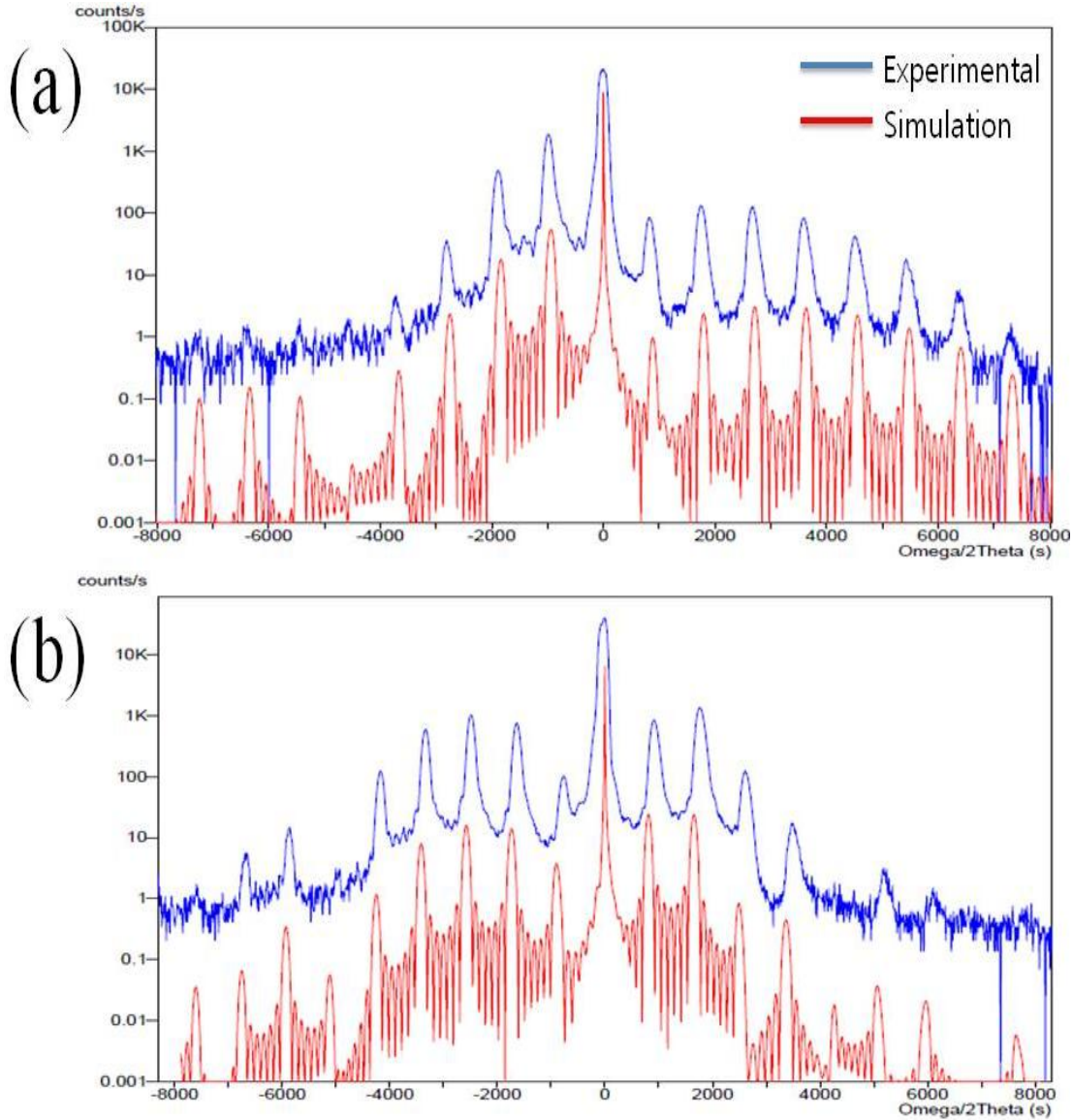


Figure 3.7 : Experimental and simulated XRD spectra for 5-period superlattices of: (a) $\text{Al}_{0.75}\text{In}_{0.25}\text{As}/\text{In}_{0.40}\text{Ga}_{0.60}\text{As}$; and (b) $\text{In}_{0.68}\text{Ga}_{0.32}\text{As}/\text{Al}_{0.56}\text{In}_{0.44}\text{As}$ layer pairs.

The blue and red curves correspond to experimental and simulation spectra, respectively. The structures were strain-compensated in each period so that we could grow relatively thick (100-150 Å) highly-strained layers without relaxation, and thus be able to obtain highly accurate thickness information. The excellent correspondence between the

experimental and simulated spectra indicates that good control of the layer thicknesses and compositions was achieved.

After x-ray calibration, the mid-IR absorption measurement was carried out at room temperature (RT) using a 20-period $\text{In}_x\text{Ga}_{1-x}\text{As}/\text{Al}_x\text{In}_{1-x}\text{As}$ superlattice structures. The FT-IR absorption measurement reconfirms not only the growth rate and composition but also crystal quality of the materials. Figure 3.8 shows the absorption results of 20-period of (a) $\text{In}_{0.53}\text{Ga}_{0.47}\text{As}$ (57 Å)/ $\text{Al}_{0.52}\text{In}_{0.48}\text{As}$ (200 Å) and (b) $\text{In}_{0.60}\text{Ga}_{0.40}\text{As}$ (46 Å)/ $\text{Al}_{0.56}\text{In}_{0.44}\text{As}$ (57 Å) superlattice structure. The $\text{In}_{0.53}\text{Ga}_{0.47}\text{As}$ (57 Å) and $\text{In}_{0.60}\text{Ga}_{0.40}\text{As}$ (46 Å) layer were highly doped to fill electrons in the ground state.

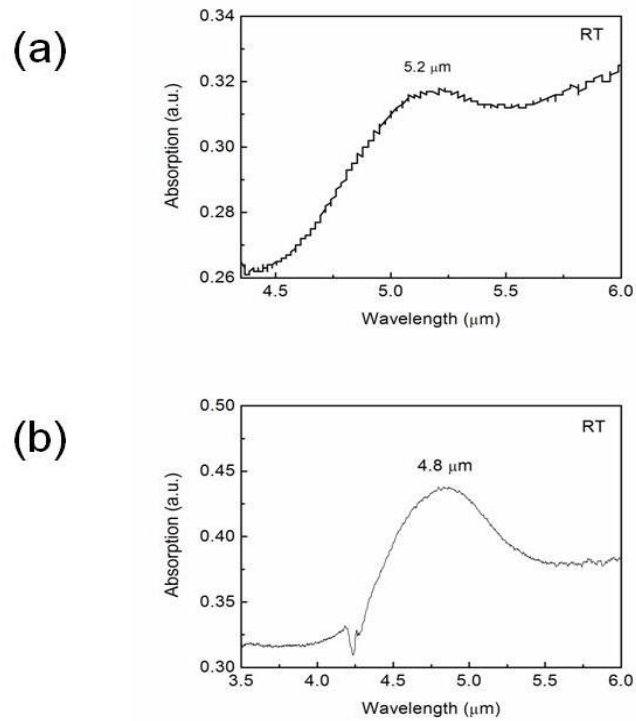


Figure 3.8: Mid-IR absorption spectra as a function of wavelength at RT: (a) 20-period of $\text{In}_{0.53}\text{Ga}_{0.47}\text{As}$ (57 Å)/ $\text{Al}_{0.52}\text{In}_{0.48}\text{As}$ (200 Å). (b) 20-period of $\text{In}_{0.60}\text{Ga}_{0.40}\text{As}$ (46 Å)/ $\text{Al}_{0.56}\text{In}_{0.44}\text{As}$ (57 Å). Both absorption spectra are exactly matched with simulation

results by 8-band K*P code.

The wavelength of both structures were calculated by 8-band k*p code. The calculated wavelengths of both structures were 5.2 μm (a) and 4.8 μm (b), respectively and the absorption peaks are exactly matched with the calculated result. The full-width at half-maximum (FWHM) of the structures (a) and (b) were 20 and 30 meV, respectively. These are comparable to the best results obtained by MBE [21]. After XRD and absorption calibration, we grew the 30 stages of deep-well QC structure then the transmission electron microscopy (TEM) was carried out to confirm interface abruptness and the layer thicknesses. The TEM image shows the layer thickness calibrated by the HRXRD and FT-IR absorption measurement is very close to the target thickness within very small error (i.e., < 5 %) as seen in figure 3.9. Also, the sharp interface was confirmed by TEM image.

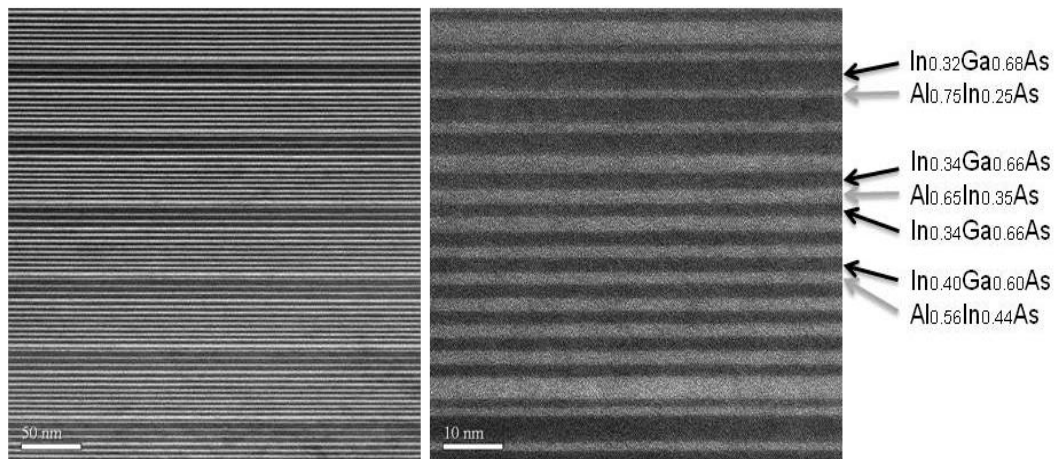


Figure 3.9: TEM image for a 30-stage, strain-compensated, deep-well QC structure. The layers in a period are compressive or tensile strained which consist of seven different

compositions.

3.6 V/III ratio

V/III ratio is very important factor to achieve good material quality such as high mobility and less impurity [13]. V/III ratio is typically higher than 100 [13] because the group V is volatile at normal growth temperature. In our system (A-200), the V/III ratio were maintained in the range of 200 – 350 for $\text{In}_x\text{Ga}_{1-x}\text{As}$ and $\text{Al}_x\text{In}_{1-x}\text{As}$ layers with the growth rate range of 1.8 – 3 Å/s. The mobility of lattice matched InGaAs and AlInAs layers which are doped to $1 \times 10^{-17}\text{cm}^3$ was more than 10,000 cm^2/Vs from Hall measurement. Several reports have shown that higher V/III ratio obtained higher mobility [13-15]. However, we didn't increase the V/III ratio more than 350 to enhance migration of the molecule on the grown surface since we believe that it gives abrupt interface between layers.

3.7 Layer strain

The InP based QCL designs below 5 μm emission are mostly strain-compensated (SC) structure [16, 17] since the conduction band offset of lattice-matched structure is small (i.e. ~520 meV) which causes significant carrier leakage from upper energy level. The deep-well QC structure is also a SC structure, but the highly strained layers (i.e., $\text{In}_{0.68}\text{Ga}_{0.32}\text{As}$ and $\text{Al}_{0.75}\text{In}_{0.25}\text{As}$) are located only in a portion of each period thus reducing the overall strain within each stage. However, precise strain calculation is

needed because the thickness of the all stages (i.e., 30 stages) reaches 1.5 μm , which means a rather small residue strain in each period will lead to relaxation.

The layer strain, ε is defined by [18]

$$\varepsilon = \frac{a_s - a_L}{a_s} \quad (3.6)$$

where a_s is lattice constant of the substrate material, a_L is the lattice constant of the overlayer. Table 3.2 shows strains of the ternary materials which are used in deep-well QC structure on InP substrate. Each strained layer has a limitation of their maximum thickness (i.e., critical thickness, d_c) because the strain energy increases as the thickness increases. The critical thicknesses can be expressed by [18]

$$d_c \cong \frac{a_s}{2|\varepsilon|} \quad (3.7)$$

In reality, the critical thickness is also affected by growth conditions such as surface conditions, temperature and dislocation kinetics. Therefore, careful inspection using XRD and FT-IR absorption measurement is needed to check the relaxation of the strained material.

Table 3.2: The InP, $\text{In}_x\text{Ga}_{1-x}\text{As}$ and $\text{Al}_x\text{In}_{1-x}\text{As}$ lattice constant and strains with InP substrate. The materials in list used in deep-well QC structures. The negative value is

compressive strain while the positive value is tensile strain.

Material	Lattice constant	Strain (%)
InP	5.869 Å	0
In _{0.40} Ga _{0.60} As	5.896 Å	-0.5
Al _{0.56} In _{0.44} As	5.836 Å	0.6
In _{0.36} Ga _{0.64} As	5.912 Å	-0.7
Al _{0.65} In _{0.35} As	5.800 Å	1.2
In _{0.34} Ga _{0.66} As	5.921 Å	-0.9
Al _{0.75} In _{0.25} As	5.760 Å	1.8
In _{0.32} Ga _{0.68} As	5.929 Å	-1.0

The well and barrier of active region of deep-well QC structure is highly compressive stain and highly tensile strain, respectively. Therefore, the total strain calculation is needed for balancing net strain. The net stain ε_{net} can be expressed by [19]

$$\varepsilon_{net} = \frac{\varepsilon_w L_w + \varepsilon_b L_b}{L_w + L_b} \quad (3.8)$$

where, ε_w is well strain, ε_b is barrier strain, L_w is well thickness and L_b is barrier thickness. All the net strains of deep-well QC structures were maintained less than ± 0.1 % to prevent generating of dislocations which cause carrier trap and gain broadening.

3.8 Doping concentration

The doping concentration of the QCL is very important since high background and injector doping leads to large free carrier absorption and waveguide loss in the device, and these losses increase the threshold current density. The doping of the InP for the cladding, contact layers, and lattice matched InGaAs and AlInAs layer were calibrated by Hall effect measurements. However, the injector region of the deep-well QC structure has $\text{In}_{0.60}\text{Ga}_{0.40}\text{As}$ and $\text{Al}_{0.56}\text{In}_{0.44}\text{As}$ layers which have to be doped to $0.7 - 1.4 \times 10^{17} \text{ cm}^{-3}$ [20]. Since these layers are highly strained (i.e., $\text{In}_{0.60}\text{Ga}_{0.40}\text{As}$ on InP is 0.5% compressively strained and $\text{Al}_{0.56}\text{In}_{0.44}\text{As}$ on InP is 0.6% tensile strained), it is not possible to grow a thick layer on InP without generating defects in the lattice. So in order to check the doping of the layers, a strain-compensated structure of $\text{In}_{0.60}\text{Ga}_{0.40}\text{As}/\text{Al}_{0.56}\text{In}_{0.44}\text{As}$ superlattice was grown. One of the layers was doped and the other was left undoped for comparison. An electrochemical capacitance-voltage (ECV) measurement was then carried out to determine the carrier concentration in the grown structure. During the ECV measurement, the sample is etched in small steps using a wet chemical etchant and the etch rate is controlled by shining light on the sample. At the end of each etch step the C-V characteristics of the sample is measured. This measurement shows doping level according to the etching depth. Shown in figure 3.10 is the ECV result of a 3-period $\text{In}_{0.60}\text{Ga}_{0.40}\text{As}/\text{Al}_{0.56}\text{In}_{0.44}\text{As}$ (300Å /300Å) structure. For figure 3.10 (a), the $\text{In}_{0.60}\text{Ga}_{0.40}\text{As}$ has a target of Si-doping of $1 \times 10^{17} \text{ cm}^{-3}$ and the $\text{Al}_{0.56}\text{In}_{0.44}\text{As}$ layer is left undoped.

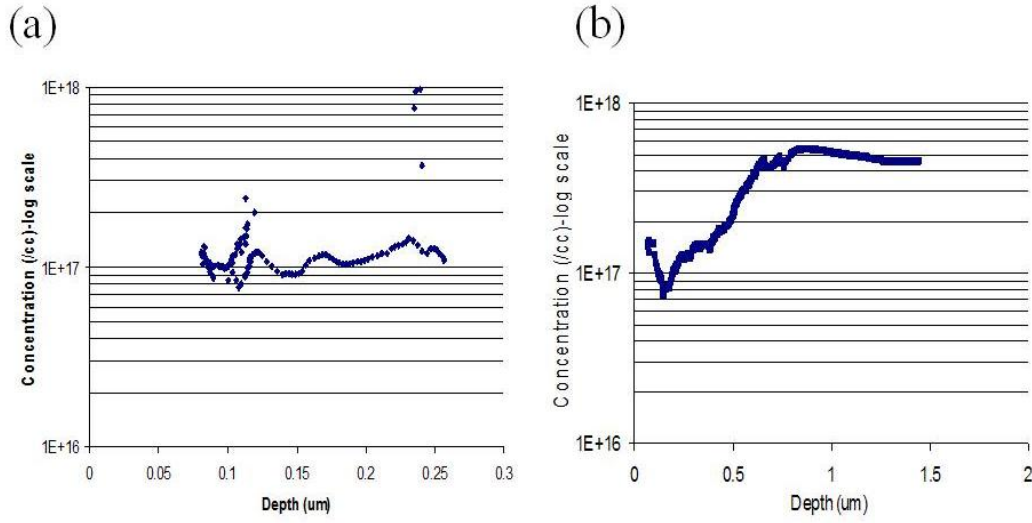


Figure 3.10: ECV measurement data for a three-period $\text{In}_{0.60}\text{Ga}_{0.40}\text{As}/\text{Al}_{0.56}\text{In}_{0.44}\text{As}$ ($300/300\text{\AA}$) structure. (a) The $\text{In}_{0.60}\text{Ga}_{0.40}\text{As}$ layer is doped and (b) the $\text{Al}_{0.56}\text{In}_{0.44}\text{As}$ layers are doped while the other layer is left undoped. Both structures have a target Si-doping concentration of $1 \times 10^{17} \text{ cm}^{-3}$.

Similarly another structure in figure 3.10 (b) was grown with the same composition and thicknesses but the $\text{Al}_{0.56}\text{In}_{0.44}\text{As}$ layer has a target of Si-doping of $1 \times 10^{17} \text{ cm}^{-3}$ and $\text{In}_{0.60}\text{Ga}_{0.40}\text{As}$ layer is left undoped. The carrier concentration of the doped layer is $\sim 1 \times 10^{17} \text{ cm}^{-3}$ from both structures. In figure 3.10 (b), the doping level (i.e., $3\text{--}5 \times 10^{17} \text{ cm}^{-3}$) after $\sim 0.5 \mu\text{m}$ indicates the doping level of the n-doped substrate.

3.9 HRXRD of the 30 stages deep-well QC structure

We have grown 30 stages of deep-well QC structure and measure high resolution x-ray diffraction (HRXRD) spectra shown in figure 3.11. The very sharp line width of the

satellite peak in overall region confirms that the good quality of superlattice periodicity, interface abruptness and low material defect. In addition, the simulation spectra are well matched with experimental HRXRD results which prove that the very accurate thickness and composition control were achieved. The total strain of both structures was slightly tensile (0.01 %).

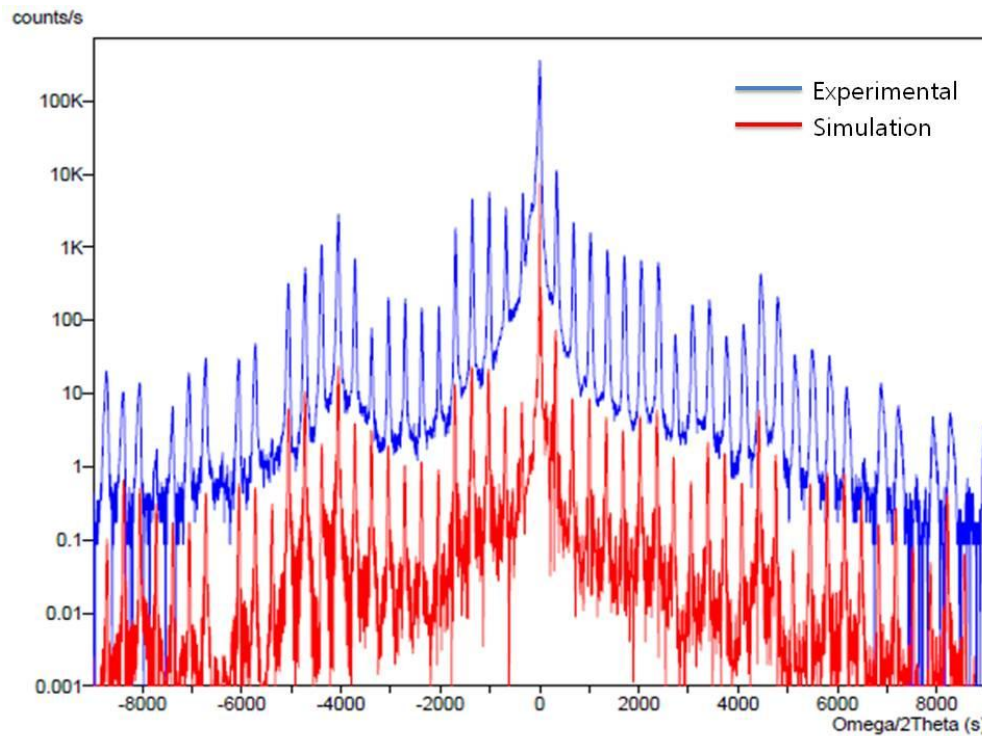


Figure 3.11: Experimental and simulated HRXRD (0 0 4) reflection spectra of 30 stages deep-well QC structures

References:

- [1] H. M Manasevit, "Single-crystal gallium arsenide on insulating substrates," Appl. Phys. Lett., vol.12, no.4, pp.156-159, (1968).
- [2] Faist, J., et al., Quantum Cascade Laser. Science, Vol. **264**(5158): p. 553-556, (1994).
- [3] Faist, J., et al., Vertical transition quantum cascade laser with Bragg confined excited state. Applied Physics Letters, Vol. **66**(5): p. 538-540, (1995).
- [4] Gerald B. Stringfellow, "Organometallic Vapor-Phase Epitaxy" Academic press, second edition (1999).
- [5] James J. Coleman, "Metalorganic Chemical Vapor Deposition for Optoelectronic Devices", Proceedings of the IEEE, Vol. 85, No. 11, (1997).
- [6] M. G. Jacko and S. J. W. Price, "Thermodynamic properties of group-III nitrides and related species", Can. J. Chem. 41 1560 (1963)
- [7] D. W. Shaw, "Kinetic aspects in the vapor phase epitaxy of III-V compounds", J. Cryst. Growth, Vol. 31, pp. 130-141, (1975).
- [8] J. Knauf, D. Schmitz, G. Strauch, H. Jurgensen, M Heyen and A Melas, "Comparison of ethyldimethylindium (EDMIn) and trimethylindium (TMIn) for GaInAs and InP growth by LP-MOVPE", Journal of Crystal Growth Vol 93, pp. 34, (1988).
- [9] System manual of the Thomas Swan CCS (3 X 2) vertical reactor.
- [10] S. G. Podorovl, G. HoElzer, E. FoErster, and N. N. Fallv, "Fourier analysis of X-ray rocking curves from superlattices", Phys. Stat. Sol (b), vol. 213, pp. 317-324, (1999).
- [11] A Sanz-Hervas, A. Sacedon, E. J. Abril, J. L. Sanchez-Rojas, C. Villar, G. D. Benito, M. Aguilar, M. Lopez, E. Calleja, and E. Munoz, "High resolution X-ray diffraction characterization of [111]B oriented InGaAs/GaAs MQW structures", Advances in X-Ray

Analysis, vol. 39, pp. 439-448, (1997).

[12] Liwei Cheng, Ruth Choa, Jacob Khurgin, Fow-Sen Choa, Xing Chen, Xiaojun wang, Jenyu Fan, Jianxin Chen, Claire Gmachl, "X-RAY DIFFRACTION ANALYSIS OF QUANTUM CASCADE LASERS", Indium Phosphide & Related Materials, (IPRM), IEEE International Conference on, May (2009).

[13] D. Kasemet, K. L. Hess, K. Mohammed, and J. L. Merz, "The effects of V/III ratio and growth temperature on the electrical and optical properties of InP grown by low-pressure metalorganic chemical vapor deposition" J. Electron. Mater. 13 655 (1984)

[14] M. Razeghi, M. A. Poisson, J. P. Larivain, and J. P. Duchemin, "Low pressure metalorganic chemical vapor deposition of InP and related compounds" J. Electron. Mater. 12 371 (1983)

[15] C. C. Hsu, J. S. Yuan, R. M. Cohen, and G. B. Stringfellow, "[Doping studies for InP grown by organometallic vapor phase epitaxy](#)" J. Crys. Growth 74 535 (1986)

[16] A. Lyakh, C. Pflugl, L. Diehl, Q. J. Wang, F. Cappasso, X. J. Wang, J. Y. Fan, T. Tanbuk-Ek, R. Maulini, A. Tsekoun, R. Go and C. K. N. Patel, "1.6W high wallplug efficiency, continuous-wave, room temperature quantum cascade laser emitting at 4.6 μm " Appl. Phys. Lett. **92**, 111110 (2008).

[17] Y. Bai S. R. Darvish, S. Slivken, W. Zhang, A. Evans, J. Nguyen and M. Razeghi, "Room temperature continuous wave operation of quantum cascade lasers with watt-level optical power", Appl. Phys. Lett. **92**, 101105 (2008).

[18] Jasprit Singh, "Electronic and Optoelectronic properties of semiconductor structures" Cambridge university press, (2003).

[19] Matsuyuki Ogasawara, Hideo Sugiura, Manabu Mitsuhara, Mitsuo Yamamoto, and

Masashi Nakao, "Influence of net strain, strain type, and temperature on the critical thickness of In(Ga)AsP-strained multi quantum wells", J. Appl. Phys., VOL. 84, pp. 4775, No. 9, (1998).

[20] J. C. Shin, M. D'Souza, Z. Liu, J. Kirch, L. J. Mawst, D. Botez, I. Vurgaftman, and J. R. Meyer, "Highly temperature insensitive, deep-well 4.8 μm emitting quantum cascade semiconductor lasers", Appl. Phys. Lett. Vol **94**, pp. 201103, (2009).

[21] D.S. Katzer, W.S. Rabinovich, G. Beadie, J. Vac. Sci. Technol. B 18 (2000) 1614.

Chapter 4

4.8 μm emitting deep-well Quantum cascade lasers

4.1 Introduction

The active regions and the relaxation/injection (R/I) regions of conventional quantum cascade lasers (QCLs) are composed of quantum wells and barriers of same composition, respectively [1-5]. As it will be shown below, this results in severe carrier leakage from the upper laser state to the continuum for state-of-the-art devices optimized for high CW power and emitting in the 4.5 -5.0 μm range [2, 3]. The carrier leakage is evidenced by the fact that the threshold-current density, J_{th} , characteristic temperature, T_0 , has relatively low value of ~ 140 K above 300 K [2, 3] and the slope efficiency characteristic temperature, T_1 , has a low value of ~ 140 K [2]. Conventional QCLs have relatively low energy differential (δE_{ul}) between the upper laser state and the top of the exit barrier (i.e., $\delta E_{\text{ul}} \sim 260$ meV), which indirectly causes the low values of both T_0 and T_1 . This strong temperature sensitivity of their electro-optical characteristics has limited the wallplug efficiency near room temperature to low values ($\sim 12\%$). There are several groups who have tried to suppress carrier leakage. Yang et al. introduced a 0.7 nm AlAs barrier as a part of a composite three-layer exit barrier for $\approx 5\mu\text{m}$ -emitting devices [6]. The device

showed relatively high peak pulsed power, but the T_0 value did not increase. For another approach, Gresch et al. used several 0.2 nm AlAs barriers same as a part of composite three-layer barriers throughout the active region of ≈ 4.8 μm -emitting devices [7]. However, that also did not increase the T_0 value above room temperature because the effective barrier thicknesses may be too thin to block carrier leakage from the upper laser state.

In this chapter, we propose varying-composition, InP-based 4.8 μm emitting QC structures which employ very deep wells and tall barriers in the active region, so a called deep-well QC structure, originally proposed for GaAs-based devices [8, 9]. The resulting active region provides very high δE_{ul} values and thus causes suppression of carrier leakage from the upper laser state. The relaxation/injection (R/I) regions, which are also composed of layers of various compositions, raise the upper Γ miniband further thus suppressing carrier leakage, while keeping the proper ΔE value for suppressing carrier backfilling. In addition, the highly strained layers are located only in a relatively small portion of each stage, thereby reducing the overall strain within each stage.

4.2 Deep-well QCL structure design

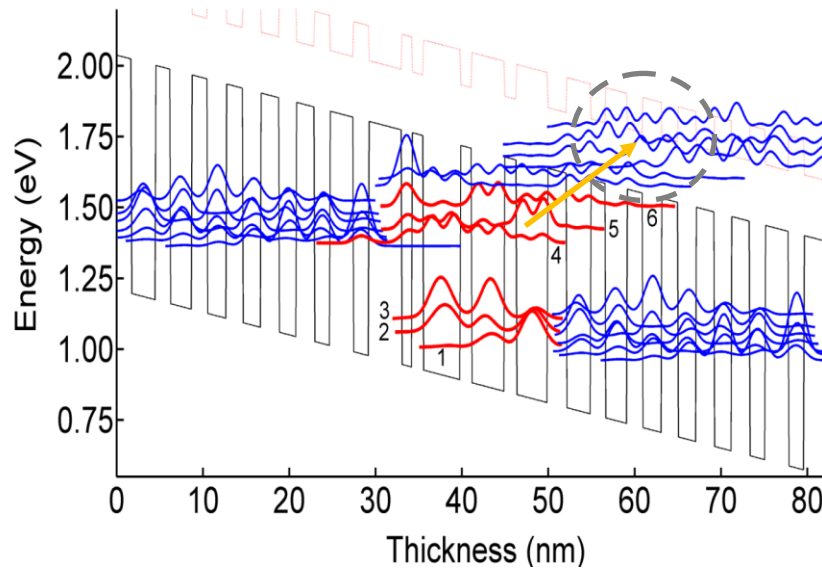


Figure 4.1: Conduction band diagram and key wavefunctions for Conventional QC laser emitting at $4.8\ \mu\text{m}$ [5]. The upper lasing level is labeled as 4; while 5, 6 and 7 are upper energy states in the active region. The laser transition occurs between states 4 and 3. The electrons in state 4 leak out in two ways: a) thermal scattering process to the upper Γ miniband (dashed dot region); b) thermal excitation to levels 5 and 6 followed by relaxation to the lower AR states 3, 2 and 1.

Figure 4.1 shows the conduction-band diagram and square modulus of the conventional $4.8\ \mu\text{m}$ -emitting QCL structure [5] which is composed of an $\text{In}_{0.669}\text{Ga}_{0.331}\text{As}/\text{Al}_{0.638}\text{In}_{0.362}\text{As}$ superlattice. The active region is of the double phonon-resonance type [10]. The lasing transition occurs between states 4 and 3. We calculated the energy levels and the corresponding wavefunctions in the active region and for the upper and lower Γ minibands in the relaxation/injection (R/I) regions using 8-band $\mathbf{k} \cdot \mathbf{p}$ code. Part of the carriers injected into the upper lasing level (state 4) get thermally excited to higher active-region energy states (i.e., states 5 and 6) at and above room

temperature [11] due to relatively small energy separations (i.e., $E_{54} = 46$ meV, $\Delta E_{65} = 80$ meV). In addition, the wavefunction of level 6 strongly overlaps with the wavefunction of the lowest state of the upper Γ miniband (See the region within the dashed-curve circle in figure 4.1). As a result, many electrons in higher energy states (i.e., 5 and 6) can escape easily to the continuum via scattering to the upper Γ miniband, similarly to what was shown by Jin et al [12] for GaAs-based QC lasers. Moreover, as shall be shown in next chapter, part of the electrons thermally excited from state 4 to states 5 and 6 are lost due to their relaxation to the lower AR states 3, 2 and 1.

We hereby present the deep-well QC structure for suppressing carrier leakage from the upper AR energy states [13]. The deep-well QC, which we designed for emitting at $4.8 \mu\text{m}$, has primarily the injector region of $5.4 \mu\text{m}$ -emitting QC lasers [14] (i.e., $\text{Al}_{0.56}\text{In}_{0.44}\text{As}/\text{In}_{0.60}\text{Ga}_{0.40}\text{As}$ superlattices). However, the quantum wells (QWs) in active region are $\text{In}_{0.68}\text{Ga}_{0.32}\text{As}$ which are much deeper in the energy than the QWs in the injector. In addition, the $\text{Al}_{0.75}\text{In}_{0.25}\text{As}$ barriers which are used in active region for the strain compensation are much taller than the barriers in conventional $4.8 \mu\text{m}$ QC structures. Specifically, for one stage of the deep-QC structure shown in Figure 4.2, starting with the exit barrier, the layer thicknesses in \AA are: **22**, [27], [19], [24], [19], [23], 20, 21, 20, 20, 22, 18, 23, 17, 23, 17, 24, **12**, 14, ***11***, **46**, ***11***, **42**, **12**, **38**. The bold normal script are $\text{In}_{0.68}\text{Ga}_{0.32}\text{As}$ wells, bold italic script are $\text{Al}_{0.75}\text{In}_{0.25}\text{As}$ barriers, normal script are $\text{In}_{0.60}\text{Ga}_{0.40}\text{As}$ wells, italic script are $\text{Al}_{0.56}\text{In}_{0.44}\text{As}$ barriers, underlining indicates doping at $1.4 \times 10^{17} \text{ cm}^{-3}$ in QWs and 10^{17} cm^{-3} in barrier. The bracketed layers are in the graded part of R/I region: one $\text{In}_{0.66}\text{Ga}_{0.34}\text{As}$ well, two $\text{In}_{0.64}\text{Ga}_{0.36}\text{As}$ wells, and two $\text{Al}_{0.65}\text{In}_{0.35}\text{As}$ barriers. The structure is strain-compensated with a net strain of 0.01%

tensile which is calculated from equation 3.6 and 3.8. At an applied field of 75 kV/cm where the energy separation between ground state of injector and upper lasing level is 7 meV, the design parameters for this 4-level state system are: the dipole matrix element is 14.5 \AA , and an upper lasing state lifetime (τ_4) is 1.35 ps, which is calculated by using the equation:

$$\tau_4 = \frac{1}{\frac{1}{\tau_{43}} + \frac{1}{\tau_{42}} + \frac{1}{\tau_{41}}} . \quad (4.1)$$

The lower lasing state lifetime (τ_3) is 0.27 ps and is calculated using the equation:

$$\tau_3 = \frac{1}{\frac{1}{\tau_{32}} + \frac{1}{\tau_{31}}} , \quad (4.2)$$

and the tunneling injection efficiency is 95% and is calculated by using the equation:

$$inj\% = \frac{z_{g4}^2}{z_{g5}^2 + z_{g4}^2 + z_{g3}^2 + z_{g2}^2 + z_{g1}^2} \times 100 . \quad (4.3)$$

Finally, the energy separation between the lower lasing level and the next injector ground state (ΔE) is 147 meV, which is expected to suppress backfilling.

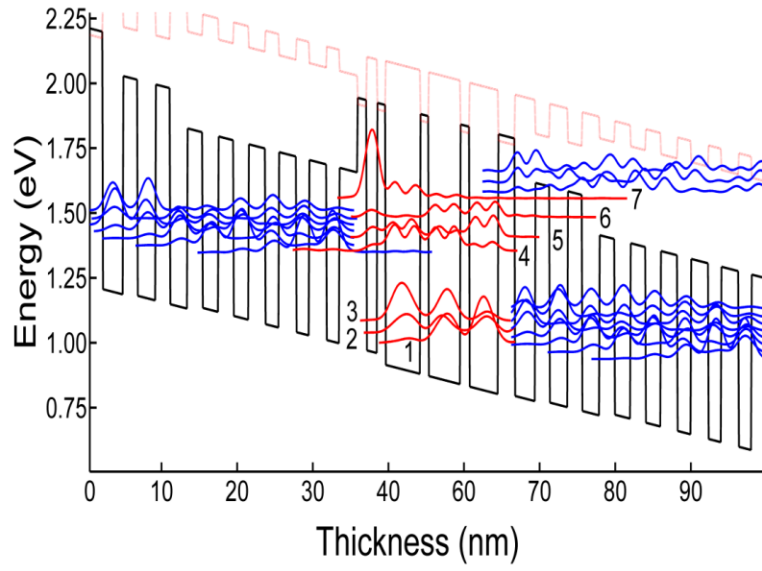


Figure 4.2: Conduction band diagram and key wavefunctions for Deep-well QC laser emitting at $4.8 \mu\text{m}$ under an electric field of 75 kV/cm ($\lambda \approx 4.8 \mu\text{m}$). The upper lasing level is labeled as 4; while 5, 6 and 7 are upper energy states in the active region. The lasing transition occurs between states 4 and 3.

As seen for figure 4.2, the δE_{ul} value increases to 450 meV , thus tightly confining the upper-lasing-level and upper-energy states (i.e., 4, 5, 6 and 7) wavefunctions to the active region. The δE_{ul} quantity is part of the electron tunneling escape rate from level i of a quantum well to the continuum [6]

$$\tau_i^{-1} \propto \exp\left(-2L_{exit} \sqrt{2m_{eb}\delta E_i} / \hbar\right) \quad (4.4)$$

, where L_{exit} is the exit barrier thickness and m_{eb} is the effective mass of electrons in the barrier, δE_i is the effective barrier height for electrons in level i , and \hbar is the Planck

constant. At a fixed barrier thickness L_{exit} , the tunneling rate at level i is a strong function of δE_i . That is, the value of the effective barrier height for the electrons in the upper lasing level, δE_{ul} is a measure of the degree of preventing electrons from escaping the active region via scattering to/relaxation to the levels in the upper/lower miniband of the R/I region. In addition, the part of the R/I region following the active region, so called extractor region, has a tapered conduction band edge which prevents wavefunctions from the upper miniband to penetrate the active region, thus further suppressing carrier leakage.

4.3 Growth conditions and fabrication

The deep-well QC structure shown in figure 4.2 was grown by metal organic chemical vapor deposition (MOCVD) with a horizontal reactor operating at a low pressure of 50 mbar. Trimethylgallium ($(\text{CH}_3)_3\text{Ga}$, TMGa), Triethylindium($(\text{CH}_3)_3\text{In}$, TMIIn) and Trimethylaluminum($(\text{CH}_3)_3\text{Al}$, TMAI) were used for Ga, In, and Al precursors respectively. AsH_3 and PH_3 were used as group V sources, and SiH_4 was used as the n-type doping source. After loading into the reactor, substrates were thermally cleaned in PH_3 ambient for 5 min at 638 °C and an InP buffer layer was grown. In order to ensure good material quality and to optimize growth conditions, HRXRD and intersubband mid-IR absorption measurements are performed on $\text{In}_x\text{Ga}_{1-x}\text{As}/\text{Al}_x\text{In}_{1-x}\text{As}$ superlattice structures, as mentioned in Chapter 3. For the mid-IR absorption measurement, the sample was prepared with two 45° polished edges. Using an FT-IR spectrometer, light was shined on one 45° wedge and, after multiple internal reflections in the sample, it was collected and focused on a deuterated triglycine sulfate (DTGS) detector. Atop a low-

doped ($1-3 \times 10^{17} \text{ cm}^{-3}$) InP substrate the following layers were grown : $0.33 \mu\text{m}$ InGaAs ($5 \times 10^{16} \text{ cm}^{-3}$ doping); a 30-stage core with the structure of a single stage given above; $0.33 \mu\text{m}$ InGaAs ($5 \times 10^{16} \text{ cm}^{-3}$ doping); $3 \mu\text{m}$ InP ($1 \times 10^{17} \text{ cm}^{-3}$ doping); $0.5 \mu\text{m}$ InP upper cladding layer ($5 \times 10^{18} \text{ cm}^{-3}$ doping); and a $0.01 \mu\text{m}$ InP cap layer ($4 \times 10^{19} \text{ cm}^{-3}$ doping). After growth, high-resolution x-ray diffraction (HRXRD) was performed to analyze the crystal line quality and layer thicknesses of the deep-well QC structure. The devices were processed by deep wet chemical etching in a $\text{HBr}:\text{HNO}_3:\text{H}_2\text{O}$ (1:1:10) solution to obtain ridges of $27 \mu\text{m}$ width at the core region, 3000 \AA of Si_3N_4 was deposited, $8 \mu\text{m}$ -wide contact stripes were opened and Ti/Au and Au/Ge/Ni/Au on the epise and on the substrate side were deposited, respectively . The laser chips were mounted epise up on gold-plated copper mounts using indium paste. The devices were measured with pulsed current (100 ns, 2kHz) at various heatsink temperature, and the laser output was focused in a mercury cadmium telluride (MCT) detector.

4.4 Results and discussion

By using deep wells and tall barriers in active regions as well as extractor region of tapered conduction band edge, carrier leakage out of the active region has been strongly suppressed. In turn that resulted in relatively high T_0 and T_1 values: 238 K, over the 20-60 °C temperature range [13], while the room-temperature J_{th} value is comparable to the best values obtained from conventional QC $4.6\text{-}4.8 \mu\text{m}$ devices of same mirror loss, same number of stages and of similar injector-region doping.

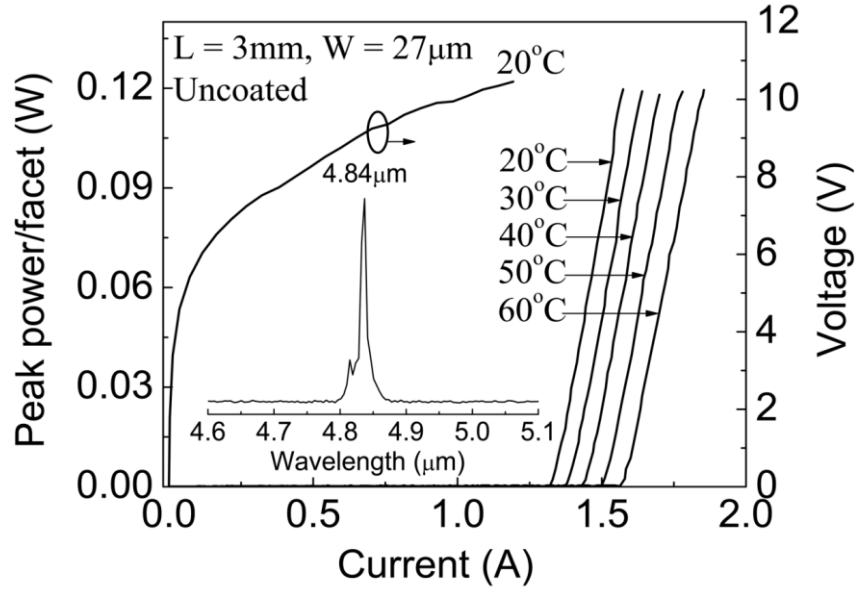


Figure 4.3: L-I curves in pulsed (100ns, 2kHz) modes at various heatsink temperatures. Also shown is the V-I curve at 20 °C. The inset shows the lasing spectrum at room temperature near threshold current with an emission peak at 4.84 μm.

The figure 4.3 shows the typical L-I-V characteristics as well as a spectrum from 3mm-long, uncoated chips. Lasing wavelength was 4.84 μm. The J_{th} value at RT (i.e., 25 °C) is 1.65 kA/cm² which for an injector doping sheet density, n_s , of 10^{11} cm⁻², is lower than the value deduced from 30-stage, 4.6 μm-emitting devices (i.e., 1.90 kA/cm²) of similar n_s value [3] and considering uncoated, 3mm-long chips. The difference may well be due to larger leakage current in conventional QCLs than in DW-QCLs.

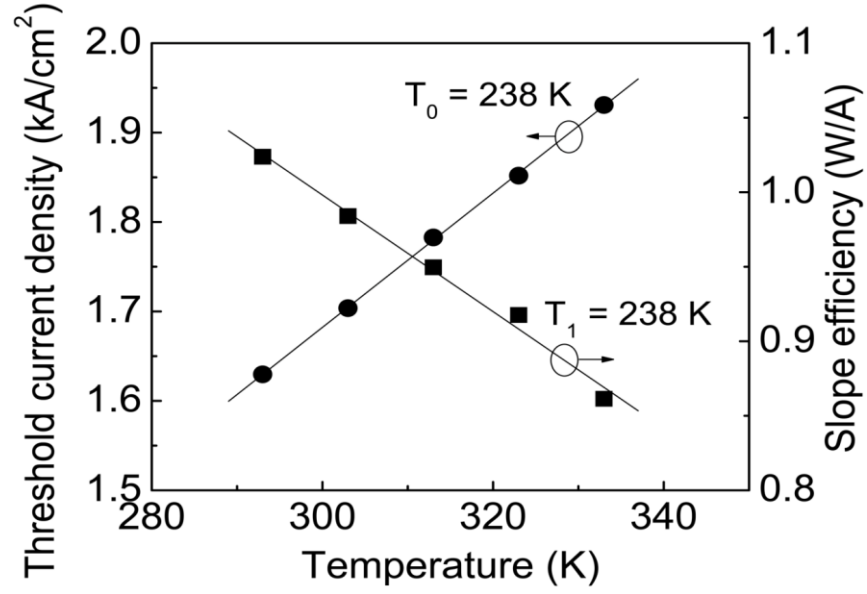


Figure 4.4: Threshold-current density and slope efficiency, η_s as a function of heatsink temperature

The light-current curves shown in Fig.4.3 are at heatsink temperatures of 20 to 60 °C, in steps of 10 °C. The temperature characteristic for J_{th} is defined as:

$$J_{th}(T_{ref} + \Delta T) = J_{th}(T_{ref}) \exp(\Delta T/T_0), \quad (4.7)$$

where $T_{ref} + \Delta T$ is the heatsink temperature and T_{ref} is the reference temperature (e.g., 300K). Similarly, the temperature characteristic for the slope efficiency, η_s , T_1 , is defined from:

$$\eta_s(T_{ref} + \Delta T) = \eta_s(T_{ref}) \exp(-\Delta T/T_1), \quad (4.8)$$

The T_0 value of the deep-well QCL is 238 K over the 20-60 °C temperature range

(Figure 4.4) whereas T_0 value of the conventional 4.6 μm QC lasers over the same temperature range has values of only 138 K to 143 K [2, 3]. In addition, the T_1 value of the deep well QCL is also 238 K over the 20-60 °C temperature range (Figure 4.4) whereas the T_1 value of the conventional 4.6 μm QC lasers over the same temperature range has values of only 140 K [2]. We attribute the increases of the T_0 and T_1 values to significant suppression of the carrier leakage out of the active regions.

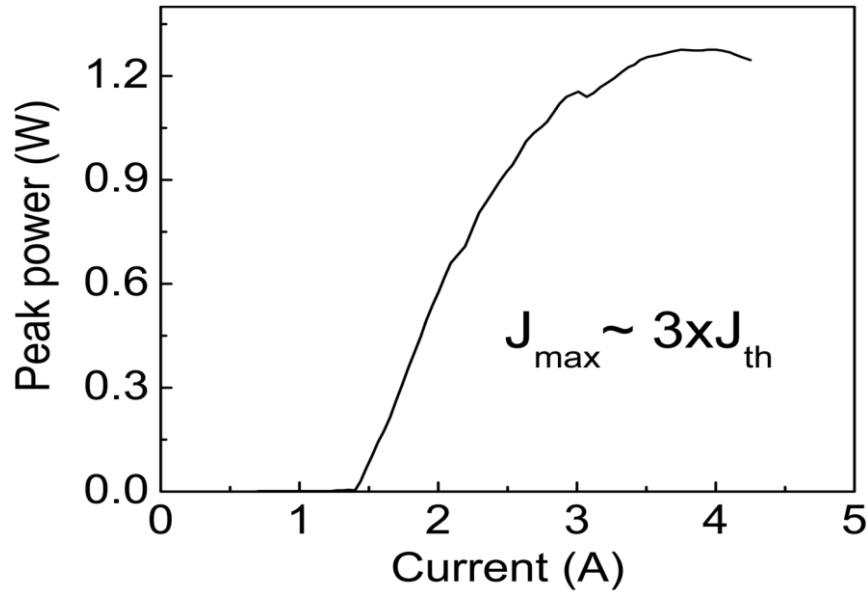


Figure 4.5: Light vs current curve of a 3 mm-long, uncoated device with stripe width of 27 μm in pulsed (250ns, 2kHz) mode at 20 °C.

The two-facet slope efficiency measured using f/1 optics is 1.05 W/A at room temperature. This slope efficiency is not corrected for the collection efficiency, which has not yet been measured. The collection efficiency is likely to be somewhat low, in part owing to the relatively wide ridge (i.e., 27 μm), which leads to multi-lateral-mode operation. Fig. 4 shows the L-I curve to high drives at 20 °C. The maximum peak pulsed

power, uncorrected for the collection efficiency, is 1.3 W. The maximum threshold current density, J_{\max} , is $\sim 5 \text{ kA/cm}^2$, typical of state-of-the-art devices.

4.5 Conclusion

A quantum cascade laser of novel design for suppressing carrier leakage out of the active region has been successfully realized via MOCVD crystal growth. For both the threshold-current density and the slope efficiency the characteristic temperature, T_0 and T_1 , reach values as high as 238 K over the 20-60 °C temperature range. Since the device temperature rise in CW operation is a function of both T_0 and T_1 , high values for those parameters will provide significantly increased RT, CW wallplug efficiencies as well as insure long-term reliability at watt-range CW powers.

References:

- [1] J. Faist, F. Capasso, C. Sirtori, D. Sivco, and A. Cho, in *Intersubband Transitions in Quantum Wells: Physics and Device Applications II*, edited by H. Liu and F. Capasso Academic, New York, Vol. 66, Chap. 1, pp. 1–83, (2000).
- [2] A. Lyakh, C. Pflugl, L. Diehl, Q.J. Wang, F. Capasso, X.J. Wang, J.Y. Fan, T. Tanbuk-Ek, R. Maulini, A. Tsekoun, R. Go and C.K.N. Patel, Appl. Phys. Lett. 92, 111110, (2008).
- [3] Y. Bai, S. R. Darvish, S. Slivken, W. Zhang, A. Evans, J. Nguyen and M. Razeghi,, Appl. Phys. Lett. **92**, 101105, (2008).
- [4] Y. Bai, S. Slivken, S. R. Darvish, and M. Razeghi, Appl. Phys. Lett., **93**, 021103, (2008).
- [5] A. Evans, S. R. Darvish, S. Slivken, J. Nguyen, Y. Bai, and M. Razeghi, “Buried heterostructure quantum cascade lasers with high continuous-wave wall plug efficiency”, Appl. Phys. Lett., Vol 91, pp. 071101, (2007).
- [6] Q. K. Yang, C. Mann, F. Fuchs, R. Kiefer, K. Köhler, N. Rollbühler, H. Schneider, and J. Wagner, Appl. Phys. Lett., Vol., 2048, (2002).
- [7] Gresch, T., Faist, J., and Giovannini, M., “Gain measurements in strain-compensated quantum cascade laser”, Appl. Phys. Lett., **94**, p.161114, (2009).
- [8] D.P. Xu, A. Mirabedini, M. D’Souza, S. Li, D. Botez, A. Lyakh, Y.-J. Shen, P. Zory, and C. Gmachl, *Appl. Phys. Lett.* **85**, 4573, (2004).
- [9] D.P. Xu, M. D’ Souza, J. C. Shin, L. J. Mawst and D. Botez, J. Crystal Growth, **310**, 2370, (2008).
- [10] D. Hofstetter, M. Beck, T. Aellen, and J. Faist, Appl. Phys. Lett. **78**, 396(2001) .
- [11] S.S. Howard, Z. Liu, and C.F. Gmachl, IEEE Photon. Tech. Lett., **44**, 319 (2008).

- [12] S.R. Jin, C. N. Ahmad, S.J. Sweeney, A.R. Adams, B.N. Murdin, H. Page, X. Marcadet, C. Sirtori and S. Tomic. Appl. Phys. Lett., **89**, Page (2006).
- [13] Shin, J. C. , D'Souza, M., Liu, Z., Kirch, J., Mawst, L. J., Botez, D. , Vurgaftman, I., and Meyer, J.R., "Highly Temperature Insensitive, Deep-Well 4.8 μm Emitting Quantum Cascade Semiconductor Lasers", Appl. Phys. Lett., 94, (20), (2009).
- [14] L. Diehl, D. Bour, S. Corzine, J. Zhu, G. Höfler, M. Loncar, M. Troccoli and F. Capasso, Appl. Phys. Lett. **89**, 081101(2006).

Chapter 5

Ultra-low temperature sensitive, deep-well, Quantum Cascade Laser via tapering the injector region

5.1 Introduction

In the chapter 4, we demonstrated [1] suppression of carrier leakage by using deep (in energy) quantum wells (QWs) and tall barriers in the active regions of 4.8 μm -emitting devices. The tapered extractor helped decouple the wavefunctions between state 6 and the upper- Γ -miniband states. That device showed T_0 and T_1 values of 238 K over the 20-60 $^{\circ}\text{C}$ temperature range.

In this chapter, we introduce equations for J_{th} and η_d which take into account both leakage and backfilling currents, then we show that by employing injector regions of uptapered conduction-band-edge, carrier leakage is further suppressed. T_0 values as high as 278 K and T_1 values as high as 285 K are obtained over a wider temperature range: 20-90 $^{\circ}\text{C}$. In addition, we can obtain reasonably good agreement between calculated and experimental values for T_o and T_1 in both conventional and DW-type QCLs by using the modified J_{th} and η_d equations, in conjunction with a model for electron thermal excitation in and out of the active region.

5. 2 Modified equations for the threshold current and the differential quantum efficiency

Figure 5.1 schematically shows the primary leakage paths from an active region of a QCL of the double-phonon-resonance (DPR) design [2]. Following the injection of electrons into the upper laser level (*i.e.*, state 4), some are thermally excited to active region's (AR's) next-higher energy level (state 5) wherefrom they either relax to the lower-energy AR states (*i.e.*, states 3, 2 and 1) or are further excited to the next-higher level (*i.e.*, state 6). For state 6 electron leakage consists of both relaxation to the states 3, 2 and 1 and excitation to the upper- Γ -miniband states and subsequently to the continuum. While other parallel leakage paths exist, their currents should be negligible. On the one hand, the tunneling-injection efficiencies are close to unity, and the QW/barrier structures (*e.g.*, $\text{In}_{0.67}\text{Ga}_{0.33}\text{As}/\text{Al}_{0.64}\text{In}_{0.36}\text{As}$) of conventional, high-performance 4.5-5.0 μm -emitting devices substantially prevent electron injection into the upper AR levels [3]. The other hand, thermal excitation from state 4 to state 6 and from state 5 to the upper- Γ -miniband states as well as relaxation from state 6 to the lower- Γ -miniband states are negligible because of relatively high energy differences and poor wavefunction overlap, respectively.

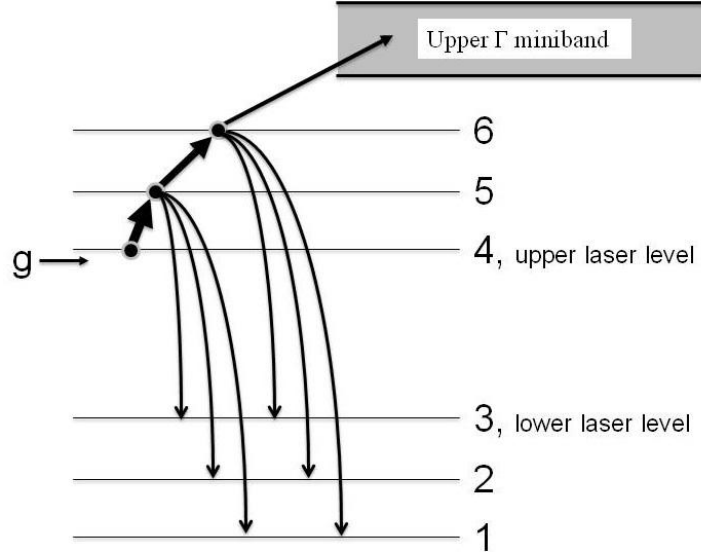


Figure 5.1: Schematic representation of the primary leakage paths for electrons injected into the upper laser level of a 4.5-5.5 μm -emitting QCL of the DPR design. g is the injector region ground state, 1 through 6 are energy states in the active region, and the area marked as upper Γ miniband corresponds to the energy states in the upper Γ miniband of the extractor region.

The conventional equations [4] for threshold and the differential quantum efficiency should be modified to include the effects of electron leakage and, in the case of η_d , of the backfilling as well [5]. We assume that the efficiency of tunneling injection from the injector to the upper laser level (η_{inj}) is unity. The threshold-current density is then the sum of J_{th} in the absence of backfilling and electron leakage, $J_{0,th}$, the current density due to backfilling, J_{bf} , and the current density due to electron leakage, J_{leak} , each of which are defined below :

$$J_{0,th} = \frac{q}{\tau_{up}} \frac{\alpha_{tot}}{g_c N_p} I \quad (5.1)$$

$$J_{bf} = \frac{q}{\tau_{up}} n_s \exp(-\Delta_{inj}/kT) \quad (5.2)$$

$$J_{leak} = \frac{q}{\tau_{5,leak}} n_5 + \frac{q}{\tau_{6,leak}} n_6 \quad (5.3)$$

where τ_{up} is the “effective” upper-state lifetime [6] due to both inelastic and elastic scattering, α_{tot} is the sum of the mirrors loss, α_m and non-resonant waveguide losses [7], α_w , g_c is the modal gain cross section per period [6], N_p is the number of periods, n_s is the electron sheet density in the injector, Δ_{inj} is the energy difference between the lower laser level and the next injector's ground state [7], and n_5/n_6 and $\tau_{5,leak}/\tau_{6,leak}$ are the electron sheet densities and carrier leakage lifetimes, respectively, corresponding to the AR's upper states 5 and 6. More specifically $\tau_{5,leak} = (1/\tau_{53} + 1/\tau_{52} + 1/\tau_{51})^{-1}$ and $\tau_{6,leak} = (1/\tau_{6,um} + 1/\tau_{63} + 1/\tau_{62} + 1/\tau_{61})^{-1}$, where $\tau_{6,um}$ is the lifetime corresponding to electron scattering from state 6 to states in the upper Γ miniband and the other lifetimes correspond to electron relaxation from states 5 and 6 to states 3, 2, and 1. Below, n_5 and n_6 are defined in the section 5.4 dedicated to estimating T_0 and T_1 values. By definition: $J_{0,th} + J_{bf} = qn_4/\tau_4$; where n_4 is the sheet density in the upper laser level (state 4) and $\tau_4 = (1/\tau_{43} + 1/\tau_{42} + 1/\tau_{41})^{-1}$ is the lifetime in that level, reflecting electron relaxation to states 3, 2, and 1. From this definition and equations (5.1)-(5.3) one can write for the net threshold-current density:

$$J_{th} = \frac{J_{0,th} + J_{bf}}{\eta_c} = \frac{q}{\eta_c \tau_4} n_4 \quad (5.4a)$$

$$\eta_c = \frac{J_{0,th} + J_{bf}}{J_{0,th} + J_{bf} + J_{leak}} \quad (5.4b)$$

where η_c is defined as the current-injection efficiency η_c is defined as the current-injection efficiency, not to be confused with the tunneling-injection efficiency which is assumed to be unity. For η_d , it can be shown from its derivation in Ref. 5 (*i.e.*, imposing the condition that the population inversion is clamped at threshold) that one obtains:

$$\eta_d = \frac{J_{0,th}}{J_{0,th} + J_{bf}} \eta_{tr} \frac{\alpha_m}{\alpha_{tot}} N_p \quad (5.5)$$

where η_{tr} is the differential efficiency of the lasing transition [6]. In order to take into account electron leakage we further insert η_c as a multiplying factor and, after defining a laser pumping efficiency term, :

$$\eta_p = \eta_c \frac{J_{0,th}}{J_{0,th} + J_{bf}} = \frac{J_{0,th}}{J_{0,th} + J_{bf} + J_{leak}} \quad (5.6a)$$

we obtain:

$$\eta_d = \eta_p \eta_{tr} \frac{\alpha_m}{\alpha_{tot}} N_p = \eta_i \frac{\alpha_m}{\alpha_{tot}} N_p \quad (5.6b)$$

where η_i , the product of η_p and η_{tr} , is in effect the laser internal efficiency. Since η_{tr} is virtually independent of temperature, and the non-resonant waveguide losses, α_w vary negligibly with T for wavelengths in the 4.5-5.5 μm range [8], it follows that the temperature dependence of η_d , and hence that of the slope efficiency, are dictated by the variations with temperature of backfilling and electron leakage. To a large extent, this

explains the experimentally-observed drop in η_d with increasing temperature, especially above 300 K (*i.e.*, the T_1 parameter). We also note that for a given heatsink temperature, changing the mirrors loss, α_m by varying the cavity length (L) or front-facet reflectivity (R_f) will alter the internal efficiency value, since $J_{0,th}$ includes α_m . The fact that η_i depends on L and R_f implies, in turn, that a conventional cavity-length [9] or reflectivity [10] study to derive η_i and α_w from $1/\eta_d$ vs. L or $1/\eta_d$ vs. $1/\alpha_m$ plots, with L or R_f varied over relatively wide ranges, may provide incorrect results.

5.3 The design of the tapered-injector, deep-well QCL

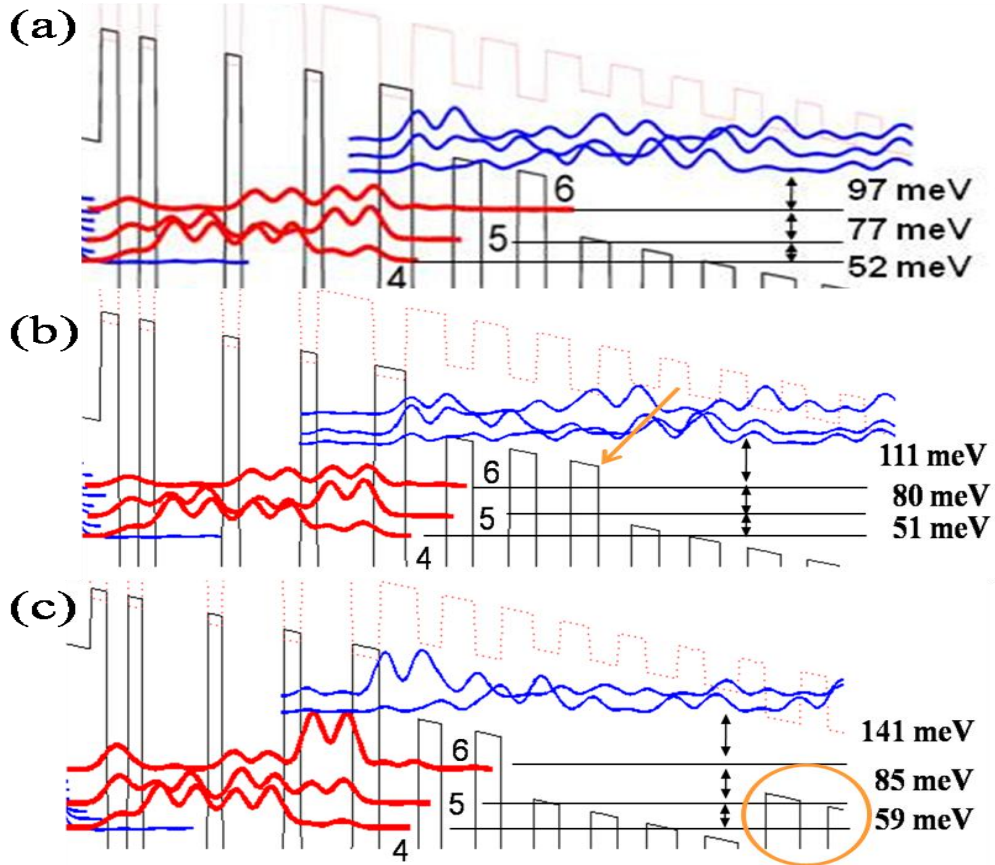


Figure 5.2: The conduction band diagram of deep-well QCL design: (a) Original deep

well QCL design [1], (b) three $\text{Al}_{0.65}\text{In}_{0.35}\text{As}$ barriers placed after the exit barrier of the original deep-well QCL design (c) tapered-injector design for the original deep-well QCL.

In chapter 4, we found that reducing the overlap of wavefunctions corresponding to the active-region upper energy levels and levels in the upper Γ miniband resulted in significant suppression of carrier leakage. However, scattering of electrons from one energy level to another depends not only on the wavefunctions overlap, but also on the energy difference between levels. Therefore, we tried several designs to increase the energy difference between upper- Γ -miniband bottom state and state 6, compared to those used in the original deep-well QCL design [See in Figure 5.2 (a)]. First, we inserted an additional barrier (i.e., $\text{Al}_{0.65}\text{In}_{0.35}\text{As}$) after the exit barrier, as seen in Figure 5.2 (b). That increased the energy separation between state 6 and upper- Γ -miniband bottom, $E_{\text{um},6}$ from 97 meV to 111 meV. However, that is a modest increase and the energy separations of E_{54} and E_{65} did not change much from the original design. Next, we created an injector region of tapered conduction-band-edge (CBE) which consists of $\text{In}_{0.36}\text{Ga}_{0.64}\text{As}$, $\text{Al}_{0.65}\text{In}_{0.35}\text{As}$, $\text{In}_{0.34}\text{Ga}_{0.66}\text{As}$ and $\text{Al}_{0.65}\text{In}_{0.35}\text{As}$ layers as seen in figure 5.2 (c). This CBE tapering for the injector, which is similar to that in the extractor region, resulted in an energy separation between state 6 and the upper Γ miniband of 141 meV; that is much larger than for the original DW-QCL. This occurred because the introduction of taller barriers near the injection barrier “pulled” the wavefunction of lowest state of the upper Γ miniband away from the active region, and thus in the extractor region the lowest miniband state becomes the 2nd state of the upper Γ miniband. In addition, the energy separations between states 4 and 5 increased from 52 to 60 meV and between states 5 and

6 increased from 77 to 85 meV. Therefore we combined the two designs shown in figure 5.1(b) and (c), and obtained an optimized tapered-injector QCL design (i.e., $E_{54} = 60$ meV and $E_{um,6} = 150$ meV) [11].

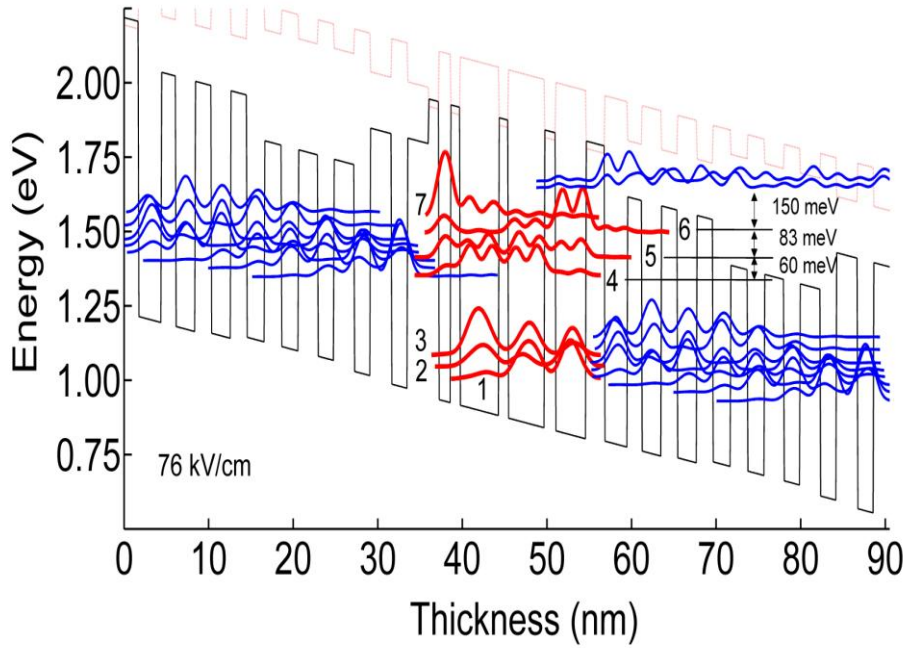


Figure 5.3: Conduction band diagram and key wavefunctions for tapering injector Deep-well QC laser emitting at $4.8 \mu\text{m}$ under an electric field of 74 kV/cm ($\lambda \approx 4.8 \mu\text{m}$). The upper lasing level is labeled as 4; while 5, 6 and 7 are upper energy states in the active region. The lasing transition occurs between states 4 and 3.

Figure 5.3 shows the conduction-band profile, energy levels and square modulus of the relevant wavefunctions in the active region and in the upper and lower Γ minibands of the relaxation/injection(R/I) regions as calculated by an 8-band $k \cdot p$ code. The layer thicknesses (in \AA) for one period, starting with the exit barrier, are: **22**, [27], [17], [23], [19], [23], [19], 21, 20, 20, 23, 19, 24, (19), (25), (19), (25), **12**, **14**, **11**, **46**, **11**, **43**, **13**, **36**.

The bold normal script are $\text{In}_{0.68}\text{Ga}_{0.32}\text{As}$ wells, bold italic script are $\text{Al}_{0.75}\text{In}_{0.25}\text{As}$ barriers, normal script are $\text{In}_{0.60}\text{Ga}_{0.40}\text{As}$ wells, italic script are $\text{Al}_{0.56}\text{In}_{0.44}\text{As}$ barriers, underlining indicates doping at $1.4 \times 10^{17} \text{ cm}^{-3}$ in the QWs and barriers. The bracketed layers are in the tapered-CBE part of the extractor region: two $\text{In}_{0.66}\text{Ga}_{0.34}\text{As}$ wells, one $\text{In}_{0.64}\text{Ga}_{0.36}\text{As}$ well and three $\text{Al}_{0.65}\text{In}_{0.35}\text{As}$ barriers. The layers in parentheses are in the uptapered-CBE part of the injector region: $\text{In}_{0.64}\text{Ga}_{0.36}\text{As}$ and $\text{In}_{0.66}\text{Ga}_{0.34}\text{As}$ wells, and two $\text{Al}_{0.65}\text{In}_{0.35}\text{As}$ barriers. The structure is strain-compensated with a nominal net (tensile) strain of 0.04 %, and the device core has 30 periods. The design parameters for this 4-level-state system at an applied field of 74 kV/cm are: 14.7 Å for the dipole matrix element, 1.32 ps for the upper-state lifetime (τ_4) from equation 4.1, 0.28 ps for the lower-state lifetime (τ_3) from equation 4.2, 147 meV for ΔE which is energy separation between lower laser state and the ground state of rear injector, and 97% for the tunneling injection efficiency from equation 4.3. The structure is similar to the structure in chapter 4 with the most notable difference being that the two $\text{Al}_x\text{In}_{1-x}\text{As}$ layers closest to the injection-barrier's $\text{Al}_{0.75}\text{In}_{0.25}\text{As}$ layer had their Al content increased from 0.56 to 0.65 and the two $\text{Ga}_x\text{In}_{1-x}\text{As}$ layers closest to the injection-barrier's $\text{Al}_{0.75}\text{In}_{0.25}\text{As}$ layer had their Ga content increased from 0.40 to 0.36 and 0.34, respectively. These taller barriers and deeper wells bring about two changes that benefit suppression of carrier leakage: a) the energy difference between states 4 and 5 increases from 52 meV to 60 meV; b) the energy difference between states 6 and the upper Γ miniband in the extractor region increases from 97 meV to 150 meV. The former suppresses thermal carrier excitation from the upper laser level (i.e., state 4) to the active-region state 5, while the latter severely suppresses thermal carrier excitation from active-region state 6 to the upper Γ miniband;

that is, carrier leakage to the continuum. The structure was grown on a low-doped ($1-3 \times 10^{17} \text{ cm}^{-3}$) InP substrate and as follows: $0.33 \mu\text{m}$ InGaAs ($5 \times 10^{16} \text{ cm}^{-3}$ doping); a 30-stage core with the structure of the single stage given above; $0.33 \mu\text{m}$ InGaAs ($5 \times 10^{16} \text{ cm}^{-3}$ doping); $3 \mu\text{m}$ InP ($1 \times 10^{17} \text{ cm}^{-3}$ doping); $0.5 \mu\text{m}$ InP upper cladding layer ($5 \times 10^{18} \text{ cm}^{-3}$ doping); and a $0.01 \mu\text{m}$ InP cap layer ($4 \times 10^{19} \text{ cm}^{-3}$ doping). After growth, high-resolution x-ray diffraction (HRXRD) was performed to analyze the crystal line quality and the layer thicknesses of the deep-well QC structure.

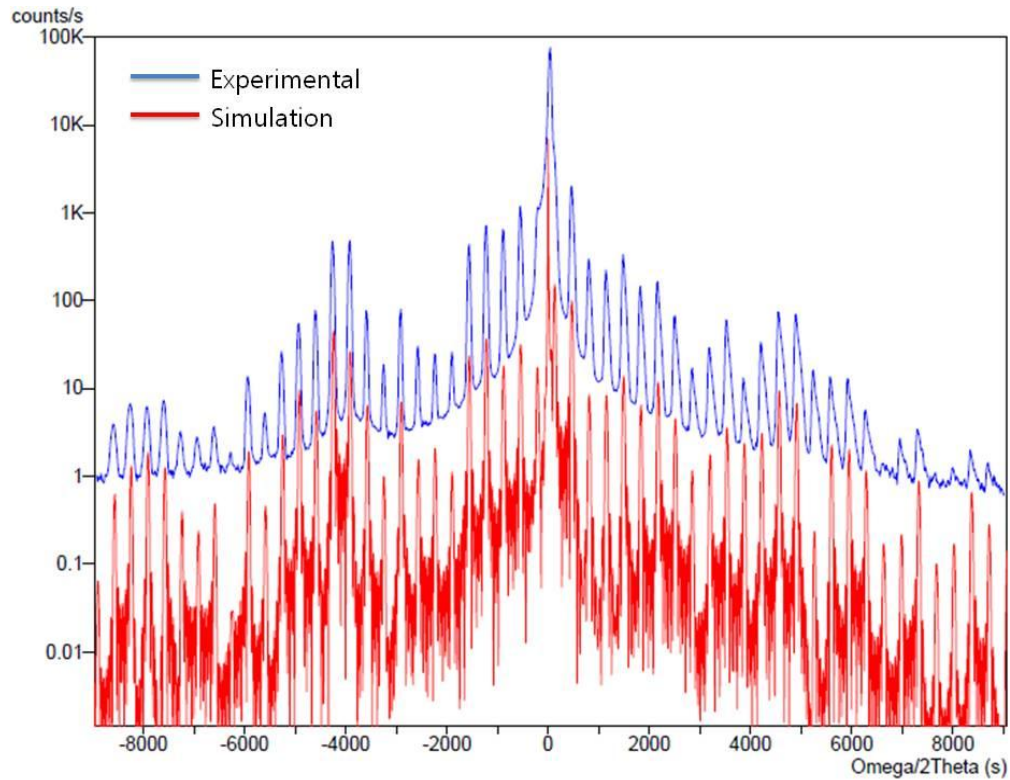


Figure 5.4: Experimental and simulated HRXRD (0 0 4) reflection spectra of 30 stages tapered injector deep-well QC structures

In figure 5.4, the HRXRD spectra which are well matched with simulation data show that

the thickness and composition are controlled very accurately as designed in Figure 5.3 through the entire core region. In addition, the extremely sharp satellite peaks through the very large range show that the core region is grown with excellent periodicity and very sharp layer interfaces [12]. The grown wafer were processed by deep wet chemical etching in a $\text{HBr}:\text{HNO}_3:\text{H}_2\text{O}$ (1:1:10) solution to obtain ridges 21-26 μm wide at the core region, depositing 3000 \AA of Si_3N_4 , opening 8 μm -wide contact stripes and using Ti/Au as metallization on the epise and Au/Ge/Ni/Au as metallization on the substrate side. 3-mm long bars were cleaved and then separated into chips. The laser chips were mounted epise up on gold-plated copper mounts using indium paste. The devices were measured pulsed (100 ns, 2 kHz) at various heatsink temperatures using a mercury cadmium telluride (MCT) detector.

5.3 Results and discussion

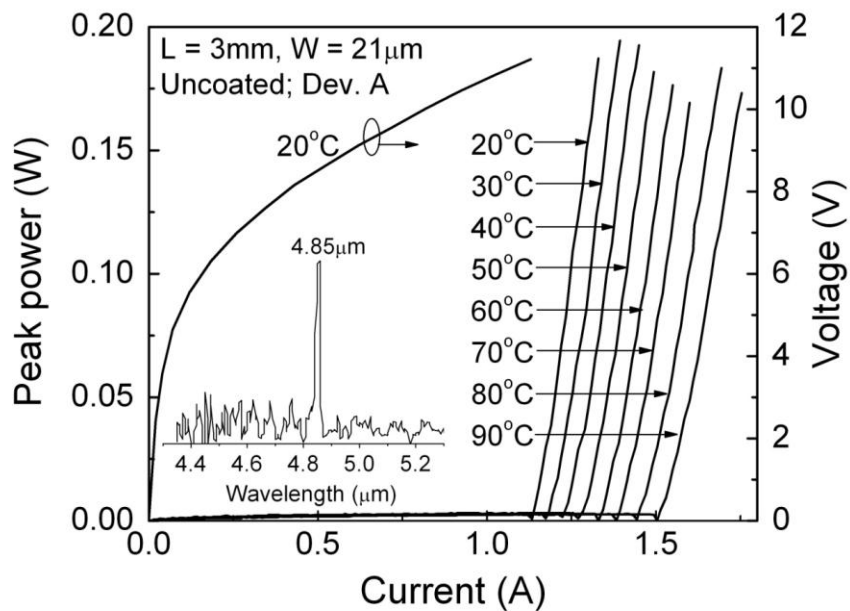


Figure 5.5: L-I curves in pulsed (100 ns, 2 kHz) modes at various heatsink temperatures. Also shown is the V-I curve at 20 °C. The inset shows the lasing spectrum at room temperature near threshold current with an emission peak at 4.85 μm .

We fabricated two different ridge widths (device A with 21 μm -wide ridge and device B with 26 μm -wide ridge). Figure 5.5 shows the results of device A. The J_{th} of the device A at 20 °C is 1.78 kA/cm^2 , a value comparable to those derived by considering uncoated, 3-mm long, conventional QC devices [13] of similar injector-doping sheet density (i.e., 10^{11} cm^{-2}) and same number of periods. The threshold voltage at 20 °C: 11.2 V, is also comparable to those from conventional, 30-period 4.8 μm QC devices. The characteristic temperature for J_{th} , T_0 , is 260 K from 20 to 60°C, and 243K from 60 to 90°C (Figure 5.6).

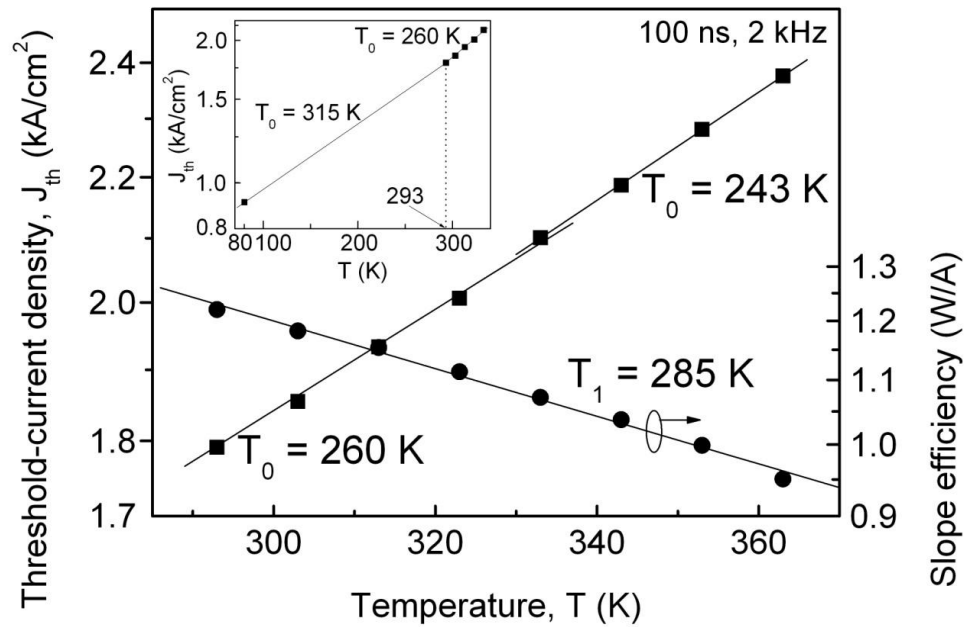


Figure 5.6: For device A, threshold-current density and slope efficiency as a function of

heatsink temperature. The inset shows the T_0 value of 315 K in the temperature range 80 to 293 K.

As shown in the inset of Figure 5.6, from 80 K to 293 K the T_0 value is 315 K. For device B, which has a somewhat higher J_{th} value at 20 °C: 1.86 kA/cm² (Figure 5.6), the T_0 value is 278 K over the 20-90 °C temperature range (inset). By comparison, for high-performance 4.6 μm QC lasers [13], over the same temperature range, T_0 is only 143 K. Similarly, the characteristic temperature for the slope efficiency, T_1 , is found to have a value of 285 K over the 20-90 °C temperature range for both devices A and B (Fig. 5.6 for device A) as compared to only ~ 140 K for 4.6-4.8 μm QC lasers over the 20-60 °C [14] and 0-50 °C [6] temperature ranges.

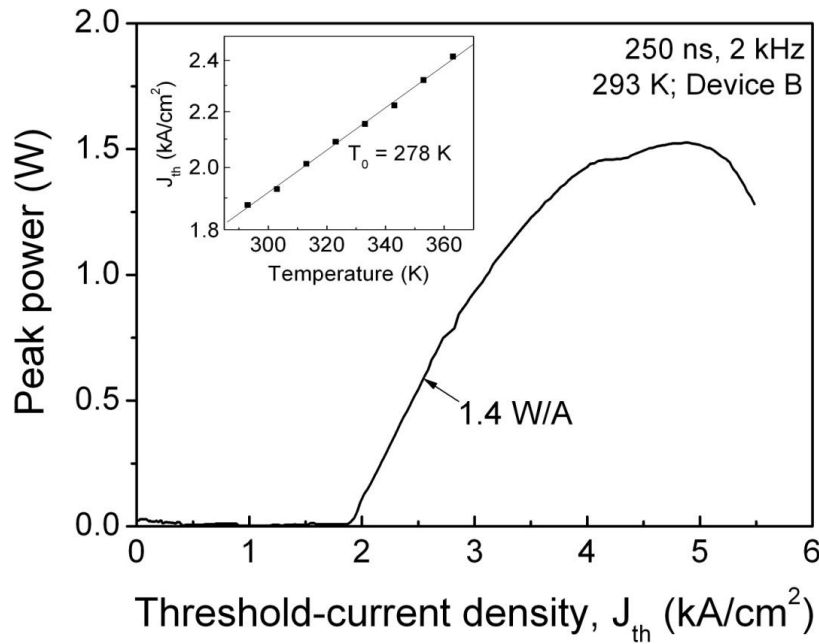


Figure 5.7: Light vs current curve of a device B (3 mm long, uncoated device with stripe

width of 26 μm) in pulsed (250ns, 2kHz) mode at 20 $^{\circ}\text{C}$. Inset shows that threshold-current density as a function of heatsink temperature, T_0 , has a value of 278 K.

Fig. 5.7 illustrates the L-I curve for device B. The slope efficiency and maximum peak power, from both facets are 1.4 W/A and 1.55 W, respectively, uncorrected for the optical collection efficiency. The high T_0 value shown in the inset, together with a high T_1 value of 285 K (not shown, but the same as for device A) indicate not only suppression of the carrier leakage, but are also indirect proof that when using heavily compressively strained (i.e., 1%) $\text{In}_{0.68}\text{Ga}_{0.32}\text{As}$ QWs carrier leakage to indirect valleys (i.e., to the X or L valleys) is not an issue. Furthermore, high T_0 and T_1 values should significantly improve the devices CW operation. On the one hand T_0 is directly related to the maximum temperature for CW lasing, T_{max} and the maximum CW power at a given heatsink temperature, P_{max} [15]. On the other hand, since both P_{max} and the maximum wallplug efficiency, $\eta_{\text{wp,max}}$ [6] are proportional with the slope efficiency, both quantities are strongly dependent on T_1 . Thus high T_0 should result in significant increases in T_{max} , while high T_0 and T_1 values should result in significant increases in both P_{max} and $\eta_{\text{wp,max}}$.

5.4 Estimates for temperature dependences of threshold current and differential quantum efficiency

We are using Eqs. (5.1)-(5.4) and (5.6b) to estimate the temperature variations of J_{th} and η_d over the range 300-360 K. To estimate the leakage current, we calculate the electron sheet densities in states 5 and 6 using the following relations:

$$n_5 = n_4 \frac{\tau_{5,tot}}{\tau_{45}} + n_6 \frac{\tau_{5,tot}}{\tau_{65}} \quad (5.9)$$

$$n_6 = n_5 \frac{\tau_{6,tot}}{\tau_{56}} \quad (5.10)$$

where $\tau_{5,tot}$ and $\tau_{6,tot}$ are the net lifetimes corresponding to electron scattering from state 5 to states 1-4 and 6, and from state 6 to states 1-5 and to states in the upper Γ miniband, respectively. The lifetime corresponding to thermal excitation of electrons from a lower-energy state i to a higher-energy state j , τ_{ij} , which is predominantly due to LO-phonon absorption scattering for large energy separations is approximated from the following expression :

$$\frac{1}{\tau_{ij}} = \frac{1}{\tau_{ji}} \exp\left(-\frac{E_{ji} - \hbar\omega_{LO}}{kT_{ei}}\right) \left(\frac{1}{\exp(\hbar\omega_{LO}/kT) - 1}\right) \quad (5.11)$$

where E_{ji} is the energy difference between states j and i , $\hbar\omega_{LO}$ is the LO phonon energy ($E_{ji} > \hbar\omega_{LO}$), and the rightmost term corresponds to the occupation number of phonons (assumed to be in thermal equilibrium with the lattice). T_{ei} is the electronic temperature for state i , which under very low duty-cycle operation (i.e., negligible Joule heating) is obtained from: $T_{ei} - T = \alpha_{E-L} \cdot J$, where α_{E-L} is the electron-lattice coupling constant [16]. The structures used in the calculations are of the conventional (Fig. 4.1 in chapter 4) and deep-well (Fig. 5.3) types, considering 3 mm-long devices with uncoated facets. Since the lifetimes due to inelastic and elastic scattering tend to be similar in the $\lambda = 4.0$ - $5.0 \mu\text{m}$ range [8] we halved the lifetimes obtained from a $k \cdot p$ code considering only inelastic scattering, and, since the elastic-scattering lifetimes are basically temperature

independent, [8] we assumed that the lifetimes vary half as fast with temperature than when only inelastic scattering is considered (*i.e.*, LO-phonon assisted scattering). Furthermore, the presence of elastic scattering (due to interface roughness) causes the electroluminescence linewidth, $2\gamma_{43}$, to vary much more slowly than when only LO-phonon scattering is considered [17]. For example, over the 300-360 K temperature range, the calculated characteristic temperature coefficient for the $2\gamma_{43}$ parameter is ~ 410 K if only LO-phonon scattering is considered [5] by comparison to the observed value of ~ 700 K. [17] Since in the $J_{0,th}$ equation the main terms that vary with temperature are the upper-state lifetime (τ_4) and $2\gamma_{43}$ we find that its T_0 value increases from 250 K when only LO-phonon scattering is considered to 450 K when both inelastic and elastic scattering are included.

We use the backfilling current as a fitting parameter with Δ_{inj} values of 100 meV for conventional devices and 120 meV for deep-well devices. The former value is consistent with values smaller than the designed ones, which are obtained from the V - I characteristics of conventional devices [7, 18]. This discrepancy may be related to the fact that, while the commonly used backfilling-current expression [7] (Eq. 5.1b) assumes that electrons in the injector are in thermal equilibrium with the lattice, an experimental investigation [19] of $\lambda = 4.8$ μm QCLs showed that the electronic temperature in the injector is clearly higher than the lattice temperature (*i.e.*, the electrons in the injector are hot). For calculating T_{ei} values we use an α_{E-L} value of $35 \text{ K cm}^2/\text{kA}$ as measured [19] for the electronic temperature of the injector ground state, T_{eg} , of $4.8 \mu\text{m}$ -emitting, strain-compensated QCLs. Since state g is strongly coupled to the upper laser level, we assume that at threshold $T_{e4} \approx T_{eg}$. We also employ $T_{e5} \approx T_{e6} \approx T_{e4}$, although these assumptions

may be less reliable.

Item Laser type	Measured T_0 (300-360 K)	J_{leak} / J_{th}		Estimated Values	
		300 K	360 K	T_0	T_1
Conventional QC	143 K	0.144	0.210	150 K	228 K
Deep-Well QC	260-278 K	0.087	0.128	240 K	514 K

Table 5.1: Estimated parameters for conventional and deep-well QCLs of DPR design ($\lambda = 4.6\text{-}4.8 \mu\text{m}$).

Table 5.1 shows calculated values for the J_{leak}/J_{th} ratio at 300 K and 360 K heatsink temperatures, and for T_0 and T_1 in conventional QCLs [14] and DW-QCLs [1] of DPR design, 30 stages, and emitting in the $4.6\text{-}4.8 \mu\text{m}$ wavelength range. For conventional QCLs the value of J_{th} at 300 K is taken to be 1.9 kA/cm^2 , as deduced from experimental data by considering uncoated, 3 mm-long chips. For DW-QCLs, the J_{th} value at 300 K is taken from experimental data for uncoated, 3 mm-long chips: 1.87 kA/cm^2 (Fig. 4.2 in chapter 4). Starting with the expression for $J_{0,th} + J_{bf}$ (i.e., n_4/τ_4) we add to it the expression for J_{leak} (Eqns. 5.3, 5.9 and 5.10) and then factor out n_4 to find its value for a given J_{th} . Subsequently, J_{leak} at 300 K was calculated. Then, the ratio of values for the quantity $J_{0,th} + J_{bf}$ at 360 K and 300 K was used as a scaling factor for n_4 when calculating J_{leak} at 360 K.

The primary electron-leakage path is found to be relaxation from state 5 to the lower AR states 3, 2 and 1, of electrons thermally excited from the upper laser level (state 4) to state

5. A secondary leakage path, which is significant only for conventional QCLs, is thermal excitation from state 6 to the upper- Γ -miniband levels, and subsequently to the continuum, of electrons (thermally) excited to state 6 from states 4 and 5.

The relative carrier leakage ($J_{\text{leak}}/J_{\text{th}}$) is significantly smaller for DW as compared to conventional devices primarily because E_{54} is 60 meV in the former compared to 46 meV in the latter [11]. The higher E_{54} value, which is a consequence of the much taller barriers, impacts J_{leak} mostly through the scattering time τ_{45} . For example, the calculated values for τ_{45} at 360 K are 0.84 ps and 0.32 ps for DW and conventional devices, respectively. The difference is due to the E_{54} dependence in the thermal-activation term of Eq. 5.11, and also the larger τ_{54} value (0.21 vs. 0.12 ps) that relates to the magnitude of E_{54} compared to the phonon energy (*i.e.*, how non-resonant is the phonon-assisted scattering).

Leakage from state 6 to the continuum is basically inexistent in DW devices because of the large energy difference between state 6 and the bottom of the upper- Γ -miniband, $E_{\text{um},6}$ (*i.e.*, 150 meV, as seen from Fig. 5.3) which in turn gives $\tau_{6,\text{um}}$ values of the order of 500 ps at 300 K and 200 ps at 360 K. In sharp contrast, $E_{\text{um},6}$ in conventional devices is ≈ 70 meV (Fig. 4.1 in chapter 4), which coupled with the significant wavefunction overlap between state 6 and the lower states of the upper miniband gives much smaller $\tau_{6,\text{um}}$ values of 2.4 ps at 300 K and 1.3 ps at 360 K. Notwithstanding, leakage through the upper miniband at 360 K is estimated to account for only 10 % of the total J_{leak} , because of the relatively high value of E_{65} (*i.e.*, 80 meV). The electron leakage to the continuum may actually be greater if the electronic temperatures of states 5 and 6 are higher than that in the upper laser level, state 4. That would in turn lower the estimated values for T_0 and may require adjusting the value of Δ_{inj} to maintain a good fit with experiment. Hence,

more detailed numerical calculations are needed to estimate the carrier leakage with greater accuracy.

The calculated T_0 values for conventional and DW devices (150 K and 240 K) are in close agreement with the experimental values of 143 K and 260-278 K, respectively. To estimate T_1 , we assumed in the equation for η_d (Eq. 5.6b) that only the pumping efficiency term, η_p , depends on temperature for the reasons provided in section 5.2. Then T_1 is obtained from Eq. 5.6a by taking, as justified above, a characteristic temperature of 450 K for $J_{0,th}$ combined with the derived T_0 value for the total J_{th} . The T_1 value thus calculated for conventional devices (i.e., 228 K) cannot be directly compared to experiment, since in the literature we could not find pulsed L-I curves beyond $T = 298$ K for DPR-design, 4.6-4.8 μm QCLs. A T_1 value of ~ 153 K can be derived from pulsed $L-I$ curves [20] covering $T = 280$ -298 K, which does not necessarily mean that it is maintained in the 298-360 K range. While pulsed $L-I$ curves for 4.6-4.8 μm -emitting devices of other depopulation designs give $T_1 \sim 143$ K over the 273-323 K range for the bound-to-continuum design [21] and ~ 140 K over the 293-333 K range for the NRE design [14], direct comparisons are not possible. For DW-type devices the calculated T_1 value of 514 K is higher than the experimental value of 285 K, yet the difference in relative decrease of the slope efficiency over the 300-360 K range is rather small: 11% rather than 19%.

Finally we estimate values for the laser internal efficiency, η_i as defined in Eq. 5.6b. As the heatsink temperature increases from 300 K to 360 K, for conventional QCLs η_i decreases from 58 % to 45 % while for deep-well QCLs η_i decreases from 76% to 67.5 %.

5.4 Conclusion

The use of deep quantum wells in the active regions of mid-infrared QCLs has resulted in the strong suppression of electron leakage. This is evidenced by much lower temperature sensitivities for both the threshold current and the slope efficiency when compared to conventional QCLs. Basically, both the threshold current and the slope efficiency of DW-QCLs vary with temperature about *2.3 times slower* than those parameters for conventional, high-performance QCLs. This dramatic suppression of carrier leakage indicates that we are approaching temperature dependences determined mainly by inelastic and elastic scattering and backfilling. The virtual doubling of T_0 and T_I above room temperature should lead to significantly improved CW performance as well as greater long-term reliability at watt-range CW powers. Furthermore, the achieved carrier leakage suppression makes DW-QCL designs ideally suited for incorporation into intersubband quantum-box laser structures. The conventional equations for threshold current and external differential quantum efficiency, η_d , have been modified to reflect electron leakage and, in the case of η_d , backfilling as well. It is found that the commonly-observed decrease in η_d above room temperature results from both electron leakage and backfilling. The electron leakage currents are calculated for 300K and 360 K heatsink temperatures, and estimated T_0 and T_I values are found to be in good agreement with experimental values for both conventional and deep-well QCLs.

References:

- [1] Shin, J. C. , D'Souza, M., Liu, Z., Kirch, J., Mawst, L. J., Botez, D. , Vurgaftman, I., and Meyer, J.R., "Highly Temperature Insensitive, Deep-Well 4.8 μm Emitting Quantum Cascade Semiconductor Lasers", *Appl. Phys. Lett.*, 94, (20), (2009).
- [2] D. Hofstetter, M. Beck, S. Blaser, T. Aellen and J. Faist, "High temperature operation of distributed feedback quantum-cascade lasers at 5.3 μm ", *Appl. Phys. Lett.* **78**, pp. 396-398 (2001).
- [3] Christian Pflügl, Laurent Diehl, Arkadiy Lyakh, Qi Jie Wang, Richard Maulini, Alexei Tsekoun, C. Kumar N. Patel, Xiaojun Wang, and Federico Capasso, "Activation energy study of electron transport in high performance short wavelengths quantum cascade lasers", *Opt. Express*, **18**, pp. 746-753 (2010).
- [4] J. Faist, F. Capasso, C. Sirtori, D. Sivco, and A. Cho, "Intersubband Transitions in Quantum Wells: Physics and Device Applications II" in Chap.1 in *Semiconductors and Semimetals*, H. Liu and F. Capasso, Eds., **66**, pp. 1–83, Academic, New York, (2000).
- [5] Chia-Fu Hsu, Jeong-Seok O, Peter Zory and Dan Botez, "Intersubband quantum-box semiconductor lasers," *IEEE J. Sel. Top. Quantum Electron.* **6**, 491-503 (2000).
- [6] J. Faist, "Wallplug efficiency of quantum cascade lasers: Critical parameters and fundamental limits" *Appl. Phys. Lett.* **90**, 253512 (2007).
- [7] A. Wittmann, A. Hugi, E. Gini, N. Hoyler, and J. Faist., "Heterogeneous High-Performance Quantum-Cascade Laser Sources for Broad-Band Tuning", *IEEE J. Quantum. Electron.* **44**, 1083-1088 (2008).
- [8] J. Faist, private communication
- [9] Jae Su Yu, Steven Slivken, Allan J. Evans, and Manijeh Razeghi, "High-Performance

Continuous-Wave Operation of $\lambda \sim 4.6 \mu\text{m}$ Quantum-Cascade Lasers Above Room Temperature”, *IEEE J. Quantum. Electron.* **44**, 747-754 (2008).

[10] Richard Maulini, Arkadiy Lyakh, Alexei Tsekoun, Rowel Go, Christian Pflügl, Laurent Diehl, Federico Capasso, and C. Kumar N. Patel, “High power thermoelectrically cooled and uncooled quantum cascade lasers with optimized reflectivity facet coatings”, *Appl. Phys. Lett.* **95**, 151112 (2009).

[11] J. C. Shin, L. J. Mawst, D. Botez, I. Vurgaftman and J. R. Meyer, “Ultra-low temperature sensitive deep-well quantum cascade lasers ($\lambda = 4.8 \mu\text{m}$) via uptapering conduction band edge of injector regions” *Elect. Lett.* Vol. 45, No. 14 (2009)

[12] J. C. Shin, M. D’Souza, J. Kirch, J. H. Park, L. J. Mawst, D. Botez, “Characteristics of Mid-IR Emitting Deep-Well Quantum Cascade Lasers Grown by MOCVD” *J. of Crystal Growth*, Vol. 312, Issue 8, pp. 1379-1382, 2010

[13] Bai, Y., Darvish, S. R. , Slivken, S., Zhang, W., Evans, A., Nguyen, J., and Razeghi, M., “Room temperature continuous wave operation of quantum cascade lasers with watt-level optical power,” *Appl. Phys. Lett.*, **92**, p.101105, (2008).

[14] Lyakh, A., Pflugl, C., Diehl, L., Wang, Q. J., Capasso, F., Wang, X. J., Fan, J. Y., Tanbuk-Ek, T., Maulini, R., Tsekoun, A., Go, R., and Patel, C. K. N., “1.6W high wallplug efficiency, continuous-wave, room temperature quantum cascade laser emitting at $4.6 \mu\text{m}$ ”, *Appl. Phys. Lett.*, **92**, p.111110, (2008).

[15] Howard, S.S., Liu, Z. and Gmachl, C.F., “Thermal and Stark-Effect Roll-Over of Quantum-Cascade Lasers”, *IEEE J. Quantum. Electron.*, 44, (4), pp.319-323, (2008).

[16] Vincenzo Spagnolo, Gaetano Scamarcio, Hideaki Page and Carlo Sirtori, “Simultaneous measurement of the electronic and lattice temperatures in

GaAs/Al_{0.45}Ga_{0.55}As quantum-cascade lasers: Influence on the optical performance”, *Appl. Phys. Lett.* **84**, 3690 (2004).

[17] A. Wittmann, Y. Bonetti, J. Faist, E. Gini, and M. Giovannini, “Intersubband linewidths in quantum cascade laser designs”, *Appl. Phys. Lett.* **93**, 141103 (2008).

[18] I. Vurgaftman, unpublished work.

[19] Miriam S. Vitiello, Tobias Gresch, Antonia Lops, Vincenzo Spagnolo, Gaetano Scamarcio, Nicolas Hoyler, Marcella Giovannini, and Jérôme Faist, “Influence of InAs, AlAs δ layers on the optical, electronic, and thermal characteristics of strain-compensated GaInAs/AlInAs quantum-cascade lasers”, *Appl. Phys. Lett.* **91**, 161111 (2007).

[20] Manijeh Razeghi, “ High-power high-wallplug efficiency mid-infrared quantum cascade lasers based on the InP/GaInAs/AlInAs material system” *Proc. SPIE* **7230**, 723011 (2009).

[21] T. Gresch, J. Faist, and M. Giovannini, “Gain measurements in strain-compensated quantum cascade laser”, *Appl. Phys. Lett.* **94**, 161114 (2009).

Chapter 6

Tapered Active-Region Quantum Cascade Laser

6.1 Introduction

In chapters 4 and 5, we demonstrated the suppression of carrier leakage by using deep (in energy) quantum wells (QWs) and tall barriers (i.e., $\text{In}_{0.68}\text{Ga}_{0.32}\text{As}/\text{Al}_{0.75}\text{In}_{0.25}\text{As}$) throughout the active regions of $4.8\text{ }\mu\text{m}$ -emitting devices [1, 2]. In addition, the tapered extractor/injector region further increases the energy separation between the active-region (AR) upper energy state and the upper Γ miniband up to 150 meV. These designs substantially reduce the current leakage from upper energy states in the active region [1, 2].

In this chapter, we introduce a new concept: Tapered Active-region Quantum Cascade Laser (TA-QCL). The barriers' height in the active region increases from the injection barrier to the exit barrier. As a result, we further increase the energy separation between the upper laser level and the AR upper energy states. Thus, electrons in the upper laser level can hardly reach the highest energy state in the AR, state 6. This design reduces the electron-leakage current by a factor of ~ 3 compared to that in deep-well QCLs. Moreover, the lifetime in the upper laser level is kept similar to that in high-performance

conventional QCLs. Then, the threshold current of the TA-QCL device at room-temperature decreases by $\sim 20\%$ compared to that for conventional, high-performance QCLs. The combination of significantly reduced electron leakage and lower room-temperature threshold leads to much higher wallplug efficiencies for TA-QCL devices than for conventional QCL devices.

6.2 The design for the tapered active-region (TA) – QCL device

Part of the electrons that are injected into the upper laser level [in the active region (AR)] are thermally excited to the upper AR energy states. The electrons in those states (i.e., states 5 and 6) relax to the lower AR states or are thermally excited to the upper Γ miniband in the extractor region, and thus are lost to the continuum. The thermal excitation is an exponential function of the energy difference between energy states [3]. Therefore the energy separation between the upper laser level and the upper AR energy states is a key to controlling the amount of electron leakage.

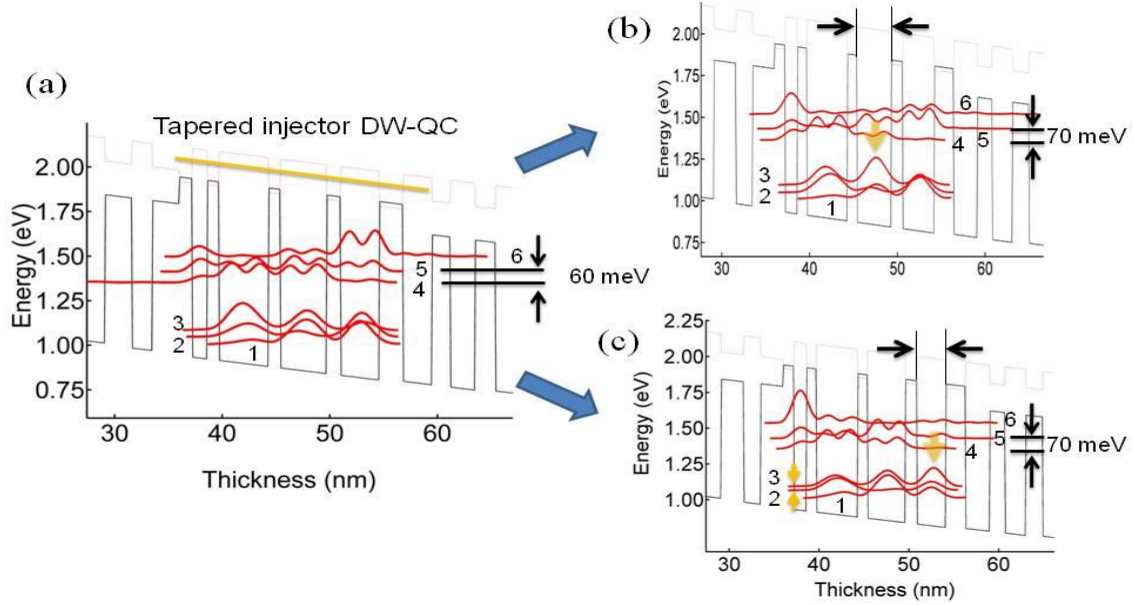


Figure 6.1: Conduction-band profile and key wavefunctions for: (a) Tapered injector (TI) Deep-well (DW) QCL emitting at $\lambda = 4.8 \mu\text{m}$, (b) TI DW-QCL structure with shortened width of the third well, and (c) shortened width of the fourth well. The upper laser level is labeled 4, while 5 and 6 are higher energy states in the active region. The lower laser level is labeled 3, while 2 and 1 are lower energy states in the active region.

Figure 6.1 (a) shows the active region of the DW-QCL structure discussed in chapter 5 [2]. To further increase the value of E_{54} the quantum wells or barriers thicknesses in active region (AR) need to be adjusted. For the design in Fig. 6.1 (a) we reduced the third-well width (Fig. 6.1(b)) or the fourth well width (Fig. 6.1 (c)) in the AR. As a result, for both cases the energy separation E_{54} increased to 70 meV from 60 meV. However, the tallest peak of the wavefunction corresponding to the lower laser level moves from the second well to the third well (Fig. 6.1(b)) and to the fourth well (Fig. 6.1 (c)),

respectively. Thus, the matrix element between laser levels is significantly reduced which in turn causes a significant increase in the threshold-current density value. Thus, these approaches to increasing E_{54} are unsatisfactory due to the unacceptable price paid in device performance.

Therefore we needed a different solution for increasing the energy separation between states 4 and 5 as well as between states 5 and 6, without decreasing the matrix element between laser levels. It is well known from quantum mechanics that for a given quantum well increasing the barriers height causes the excited-states energies to increase faster than the ground-state energy [4]. We applied this fact to coupled quantum wells.

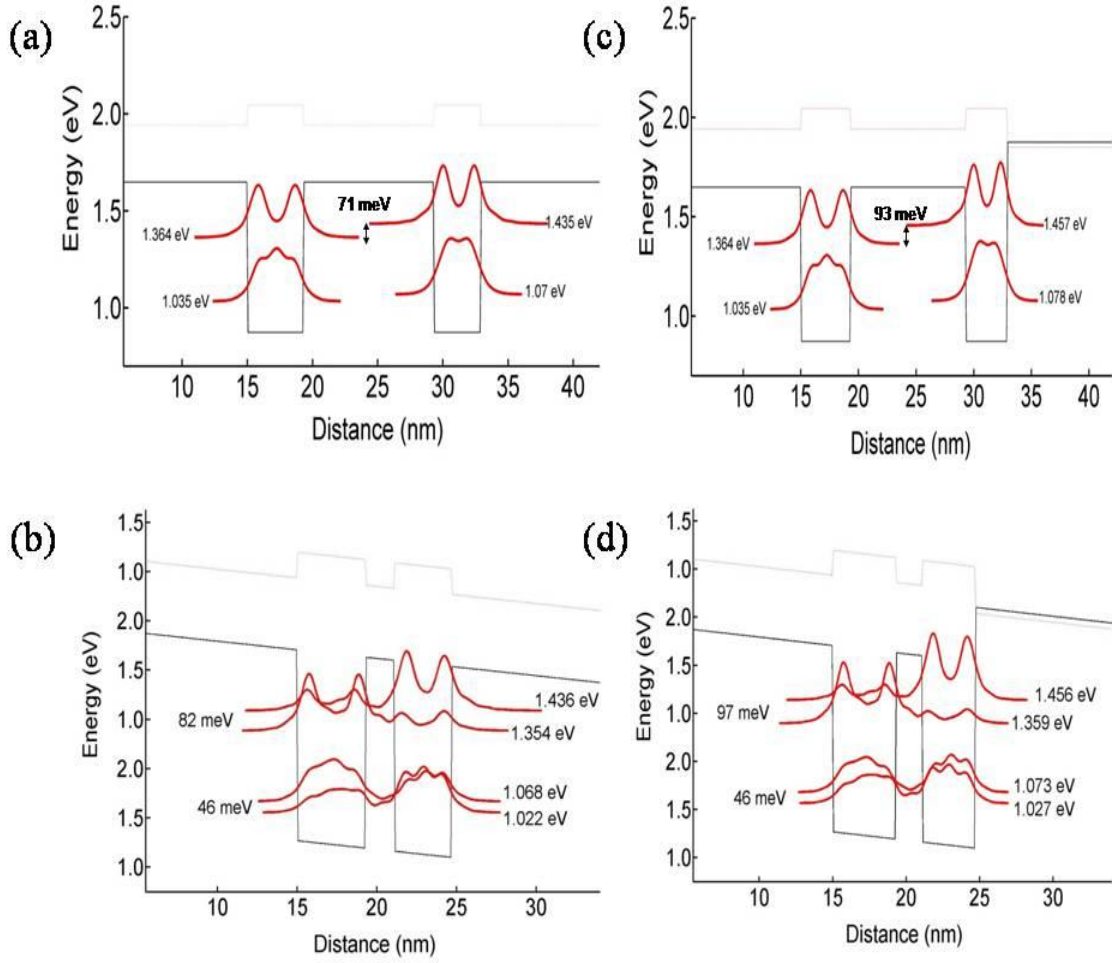


Figure 6.2: Conduction band diagram and energy levels under: (a) no bias and (b) an electric field of 70 kV/cm. The quantum wells are $\text{In}_{0.68}\text{Ga}_{0.32}\text{As}$ for all structures. The barriers in (a) and (b) are $\text{Al}_{0.60}\text{In}_{0.40}\text{As}$. In (c) and (d) we have both $\text{Al}_{0.60}\text{In}_{0.40}\text{As}$ and $\text{Al}_{0.75}\text{In}_{0.25}\text{As}$ barriers.

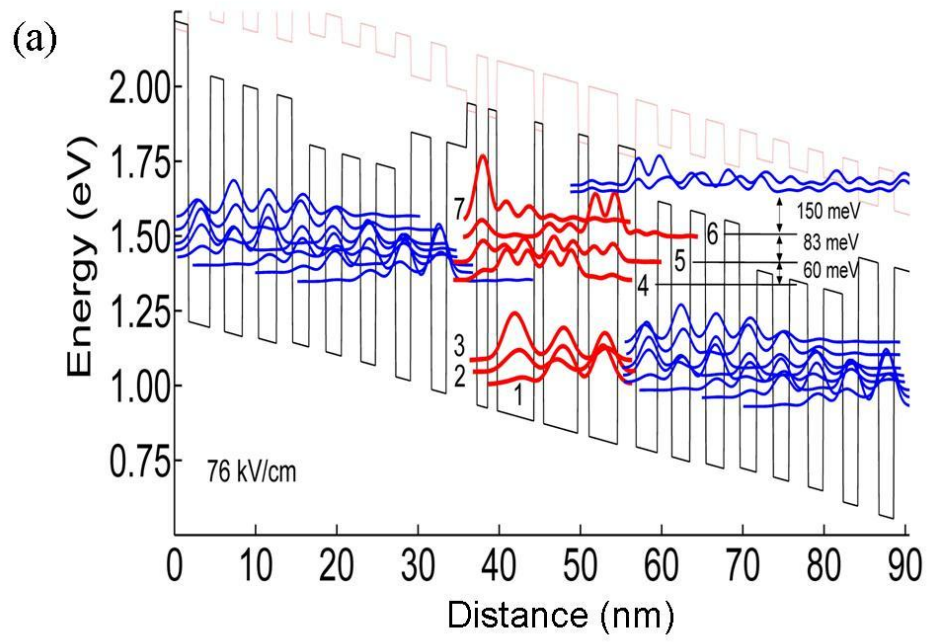
All the barriers in Fig. 6.2 (a) and (b) are made of $\text{Al}_{0.60}\text{In}_{0.40}\text{As}$, but in Figure 6.2 (c) and (d), the first two barriers from the left are $\text{Al}_{0.60}\text{In}_{0.40}\text{As}$ while the third barrier is a taller one: $\text{Al}_{0.75}\text{In}_{0.25}\text{As}$. All quantum wells (QWs) in Fig. 6.2 are $\text{In}_{0.68}\text{Ga}_{0.32}\text{As}$. The thicknesses of the first and second well are 4.3 nm and 3.6 nm for all structures chosen such that strong coupling of their ground states occurs when applying a field of 70 kV/cm.

The barrier thickness between QWs is chosen to be 10 nm when the QWs are uncoupled (Fig. 6.2 (a) and 6.2 (c)). Under no bias, the ground and excited states of the first QW from left has the same energy for both cases (i.e., 1.035 eV). However, the ground and excited state energy of the second quantum well are 8 meV and 22 meV higher, respectively for the asymmetric-QWs case (Fig. 6.2 (a)) compared to the symmetric-QWs case (Fig. 6.2 (c)). More specifically what happens is that increasing the height of the barrier on the right for the second QW “draws” upwards the QWs excited-state energy to much more than for the ground state.

For Figures 6.2 (b) and (d), we applied an electric field of 70 kV/cm and reduced the barrier thickness to 1.8 nm; thus the ground states of the two quantum wells are strongly coupled to each other, the coupling being evident from an energy separation of 46 meV for both structures. The excited states couple as well with the coupling-induced increase in energy separation being 11 meV and 4 meV larger than the energy separation in the no-bias case for the symmetric-QWs structure and the asymmetric-QWs structure, respectively (see Fig. 6.2). The weaker coupling in the asymmetric-QWs case can be understood in view of the fact that the electric field at resonance between the excited states is ~ 200 kV/cm in the asymmetric-QWs case compared to 150 kV/cm in the symmetric-QWs case. At resonance the splitting is similar : 70 and 72 meV for the symmetric-QWs and asymmetric-QWs, respectively.

The net effect is that the energy difference between the coupled excited states is 15 meV higher for the asymmetric-QWs structure than for the symmetric-QWs structure (i.e., 97 meV vs. 82 meV). We extend this property of asymmetric-QWs structures to the entire active region of deep-well QCLs.

Figure 6.3 shows a comparison between the conduction band diagram and relevant wavefunctions of a Deep-well (DW) QCL [2] and those of a TA-DW-QCL. Both designs use the double-phonon-resonance (DPR) design for depopulation of the lower laser level [5].



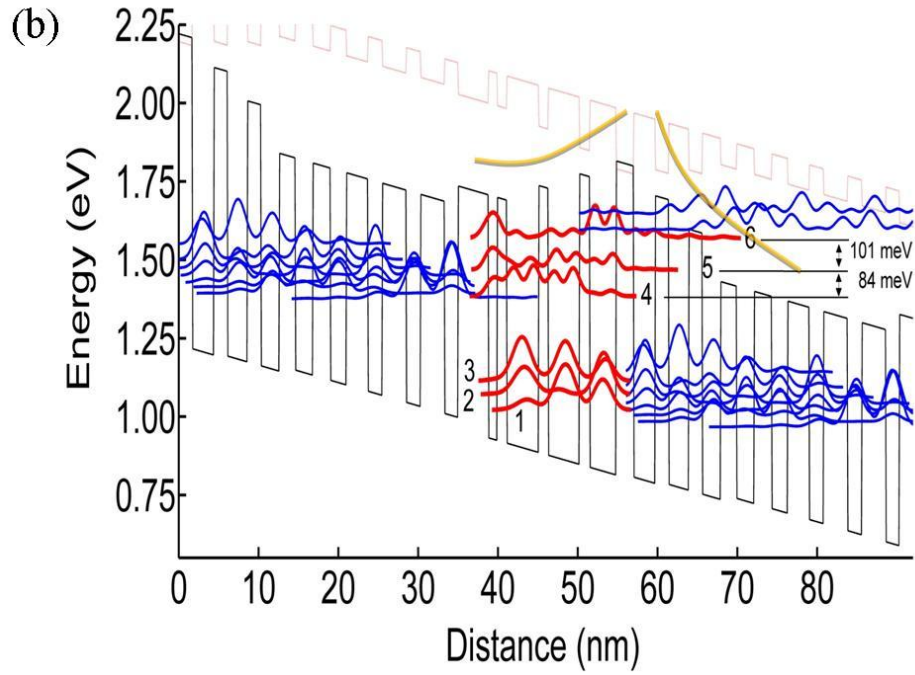


Figure 6.3: Conduction-band profile and key wavefunctions for: (a) Deep-well QCL (b) Tapered active-region, deep-well QCL emitting at $\lambda = 4.8 \mu\text{m}$. The upper laser level is labeled 4, while 5 and 6 are higher energy states in the active region. The band profile at the top of each figure corresponds to the X valley.

The tapered barrier heights in the active region of Fig. 6.3 (b) cause the energy difference between states 4 and 5, E_{54} to increase to 84 meV from 60 meV in the DW-QCL case [2]. In addition, the E_{65} value increases to 101 meV vs. 83 meV in the DW-QCL case. These large energy separations further suppress the electron leakage from the upper laser state to the upper energy states compared to the original deep-well QCL structure.

For high-performance QCLs with lower laser levels depopulated via the non-resonant-extraction (NRE) design, [6] E_{54} values as high as 63 meV have been reported [7].

However, the E_{65} value is only about 40 meV in such devices [8] as compared to 101 meV for the TA-QCL with DPR design in Fig. 6.3 (b). The low E_{65} value for the NRE-design QCL in turn leads to easy carrier escape to the continuum, as attested by the observation of relatively small values for both T_0 and T_1 (≈ 140 K) [6]. The E_{54} and E_{65} values (84 meV and 101 meV) achieved with the TA DW-QCL design are to the best of our knowledge the largest such values for any type of QCL design.

We have calculated the electron leakage using the equations in Chapter 5 [3] and find that for TA-QCLs the electron leakage is reduced by a factor of ~ 3 compared to that in deep-well QCLs [1, 2]. More specifically, the relative leakage current $J_{\text{leak}}/J_{\text{th}}$ decreases from 8.8% to $\sim 3\%$. The matrix element (i.e., z_{43}) of the lasing transition is 1.4 nm, and the lifetimes τ_4 and τ_3 have values of 1.59 ps and 0.36 ps, respectively. These values are similar to those in high-performance conventional QCLs. In turn, due to the significant decrease in leakage current, we calculate that the room-temperature threshold, I_{th} , of TA-QCL will decrease by $\sim 20\%$ by comparison to that of conventional QCLs.

The combination of lower room-temperature I_{th} and virtually suppressed electron-leakage current leads to significantly higher pulsed maximum wallplug efficiency, $\eta_{\text{wp, max}}$ values for TA-QCLs than for DW-QCLs [9]. We estimate for the front-facet emitted power of high-reflectivity-coated back facet devices (i.e., the usable power) pulsed room-temperature $\eta_{\text{wp, max}}$ values of 24 % for TA-QCL devices; that is ~ 1.7 times higher than the best pulsed $\eta_{\text{wp, max}}$ values published to date from single-facet power [10]. By considering similar series and thermal resistances, we further estimate a front-facet CW

$\eta_{\text{wp, max}}$ value of 23 %; that is basically twice the best CW $\eta_{\text{wp, max}}$ obtained to date at 300 K from any kind of QCLs.

6.3 Conclusion

By using tapered active-region barriers, we have increased the energy difference E_{54} between the upper laser level (state 4) and the next-high AR energy level (state 5) to 84 meV, and the energy difference E_{65} between the upper AR energy levels (state 5 and 6) to 101 meV. Both the electron-leakage current as well as the room-temperature threshold current are reduced. This dramatic suppression in electron-leakage current should lead to significantly improved QCL CW performance as well as greater long-term reliability at watt-range CW powers.

References:

- [1] J. C. Shin, M. D'Souza, Z. Liu, J. Kirch, L. J. Mawst, D. Botez, I. Vurgaftman and J. R. Meyer, "Highly Temperature Insensitive, Deep-Well 4.8 μm Emitting Quantum Cascade Semiconductor Lasers", *Appl. Phys. Lett.* **94**, 201103 (2009).
- [2] J. C. Shin, L. J. Mawst, D. Botez, I. Vurgaftman and J. R. Meyer, "Ultra-low temperature sensitive deep-well quantum cascade lasers ($\lambda = 4.8 \mu\text{m}$) via uptapering conduction band edge of injector regions" *Elect. Lett.* Vol. 45, No. 14 (2009).
- [3] D. Botez, J. C. Shin, S. Kumar, L. J. Mawst, I. Vurgaftman, and J. R. Meyer, "Electron leakage and its suppression via deep-well structures in 4.5-5.0 μm -emitting quantum cascade lasers", *Opt. Eng.*, to be published (2010).
- [4] John P. McKelvey, *Solid State and Semiconductor Physics*, Harper of Row, New York 1966.
- [5] D. Hofstetter, M. Beck, S. Blaser, T. Aellen and J. Faist, "High temperature operation of distributed feedback quantum-cascade lasers at 5.3 μm ", *Appl. Phys. Lett.* 78, pp. 396-398 (2001).
- [6] A. Lyakh, C. Pflugl, L. Diehl, Q. J. Wang, F. Capasso, X. J. Wang, J. Y. Fan, T. Tanbuk-Ek, R. Maulini, A. Tsekoun, R. Go, and C. K. N. Patel, "1.6W high wallplug efficiency, continuous-wave, room temperature quantum cascade laser emitting at 4.6 μm ," *Appl. Phys. Lett.* **92**, 111110 (2008).
- [7] A. Lyakh, R. Maulini, A. Tsekoun, R. Go, C. Pflügl, L. Diehl, Q. J. Wang, Federico Capasso, and C. Kumar N. Patel, "3 W continuous-wave room temperature single-facet emission from quantum cascade lasers based on nonresonant extraction design approach", *Appl. Phys. Lett.* **95**, 141113 (2009).

- [8] Christian Pflügl, Laurent Diehl, Arkadiy Lyakh, Qi Jie Wang, Richard Maulini, Alexei Tsekoun, C. Kumar N. Patel, Xiaojun Wang, and Federico Capasso, “Activation energy study of electron transport in high performance short wavelengths quantum cascade lasers”, *Opt. Express*, **18**, pp. 746-753 (2010).
- [9] D. Botez, S. Kumar, J. C. Shin, L. J. Mawst, I. Vurgaftman and J. R. Meyer, unpublished work.
- [10] Richard Maulini, Arkadiy Lyakh, Alexei Tsekoun, Rowel Go, Christian Pflügl, Laurent Diehl, Federico Capasso, and C. Kumar N. Patel, *Appl. Phys. Lett.* **95**, 151112 (2009).

Appendix

The growth spreadsheet for the 4.8 μm emitting tapered injector DW-QCLs

Layer	Thickness (\AA)	Growth rate ($\text{\AA}/\text{s}$)	Growth time (s)	Doping (cm^{-3})
InP	5000	3.150	1587.3	$1 \cdot 10^{17}$
Digital grading I				
Ga _{0.47} In _{0.53} As	25	1.633	15.3	$1 \cdot 10^{17}$
Al _{0.48} In _{0.52} As	25	3.500	7.1	$1 \cdot 10^{17}$
Ga _{0.47} In _{0.53} As	30	1.633	18.4	$1 \cdot 10^{17}$
Al _{0.48} In _{0.52} As	20	3.500	5.7	
Ga _{0.47} In _{0.53} As	35	1.633	21.4	
Al _{0.48} In _{0.52} As	15	3.500	4.3	
Ga _{0.47} In _{0.53} As	40	1.633	24.5	
Al _{0.48} In _{0.52} As	10	3.500	2.9	
Ga _{0.47} In _{0.53} As	45	1.633	27.6	
Al _{0.48} In _{0.52} As	5	3.500	1.4	
Ga _{0.47} In _{0.53} As	3300	1.633	2020.4	

Active region X 30

Ga _{0.34} In _{0.66} As	19	2.080	9.1	
Al _{0.65} In _{0.35} As	25	2.433	10.3	
Ga _{0.36} In _{0.64} As	19	1.971	9.6	
Al _{0.56} In _{0.44} As	24	2.850	8.4	$1.4 \cdot 10^{17}$
Ga _{0.40} In _{0.60} As	19	1.860	10.2	$1.4 \cdot 10^{17}$
Al _{0.56} In _{0.44} As	23	2.850	8.1	$1.4 \cdot 10^{17}$
Ga _{0.40} In _{0.60} As	20	1.860	10.8	$1.4 \cdot 10^{17}$
Al _{0.56} In _{0.44} As	20	2.850	7.0	
Ga _{0.40} In _{0.60} As	21	1.860	11.3	
Al _{0.65} In _{0.35} As	19	2.433	7.8	
Ga _{0.36} In _{0.64} As	23	1.971	11.7	
Al _{0.65} In _{0.35} As	19	2.433	7.8	

Ga_{0.34}In_{0.66}As	23	2.080	11.1
Al_{0.65}In_{0.35}As	17	2.433	7.0
Ga_{0.34}In_{0.66}As	27	2.080	13.0
Al_{0.75}In_{0.25}As	20	2.150	9.3
Ga_{0.32}In_{0.68}As	36	2.300	15.7
Al_{0.75}In_{0.25}As	13	2.150	6.0
Ga_{0.32}In_{0.68}As	43	2.300	18.7
Al_{0.75}In_{0.25}As	11	2.150	5.1
Ga_{0.32}In_{0.68}As	46	2.300	20.0
Al_{0.75}In_{0.25}As	11	2.150	5.1
Ga_{0.40}In_{0.60}As	14	2.300	6.1
Al_{0.75}In_{0.25}As	12	2.150	5.6
Al_{0.65}In_{0.35}As	27	2.433	11.1

Digital grading
VI

Al_{0.48}In_{0.52}As	14	3.500	4.0	1*10¹⁷
Ga_{0.47}In_{0.53}As	20	1.633	12.2	1*10¹⁷
Al_{0.48}In_{0.52}As	12	3.500	3.4	1*10¹⁷
Ga_{0.47}In_{0.53}As	24	1.633	14.7	1*10¹⁷
Al_{0.48}In_{0.52}As	10	3.500	2.9	1*10¹⁷
Ga_{0.47}In_{0.53}As	32	1.633	19.6	1*10¹⁷
Al_{0.48}In_{0.52}As	8	3.500	2.3	1*10¹⁷
Ga_{0.47}In_{0.53}As	37	1.633	22.7	1*10¹⁷
Al_{0.48}In_{0.52}As	5	3.186	1.6	1*10¹⁷
Ga_{0.47}In_{0.53}As	3400	1.633	2081.6	5*10¹⁶
Digital grading InP				
Al_{0.48}In_{0.52}As	5	3.500	1.4	1*10¹⁷
Ga_{0.47}In_{0.53}As	45	1.633	27.6	1*10¹⁷
Al_{0.48}In_{0.52}As	10	3.500	2.9	1*10¹⁷
Ga_{0.47}In_{0.53}As	40	1.633	24.5	1*10¹⁷
Al_{0.48}In_{0.52}As	15	3.500	4.3	1*10¹⁷
Ga_{0.47}In_{0.53}As	35	1.633	21.4	1*10¹⁷
Al_{0.48}In_{0.52}As	20	3.500	5.7	1*10¹⁷
Ga_{0.47}In_{0.53}As	30	1.633	18.4	1*10¹⁷
Al_{0.48}In_{0.52}As	25	3.500	7.1	1*10¹⁷

Ga_{0.47}In_{0.53}As	25	1.633	15.3	1*10¹⁷
InP	35000	3.150	11111.1	1*10¹⁷
InP	5000	3.150	1587.3	5*10¹⁸
InP	100	3.150	31.7	5*10¹⁹